Response Across Biological Scales: Topologically-Bound Sensitivity and Cooperative Antibiotic Resistance

by

Gabriela Fernandes Martins

A dissertation submitted in partial fulfillment
of the requirements for the degree of
Doctor of Philosophy
(Physics)
in The University of Michigan
2026

Doctoral Committee:

Associate Professor Jordan M. Horowitz, Chair
Professor David Lubensky
Assistant Professor Suraj Shankar
Associate Professor Qiong Yang
Assistant Professor Luis Zaman

Gabriela Fernandes Martins
gmartins@umich.edu
ORCID iD: 0009-0005-0598-64400

© Gabriela Fernandes Martins 2026

DEDICATION

To my family: Mom, Dad, Lucas, Lili and Alisher.

ACKNOWLEDGEMENTS

Doing impactful research is deeply rewarding, but it is also undoubtedly challenging. I was lucky to have the support of two incredible scientists and advisors throughout my PhD: Prof. Jordan Horowitz and Prof. Kevin Wood. I am forever grateful to Jordan for introducing me to the mesmerizing world of Biophysics. Under his guidance, I developed a great appreciation for the role of scientific intuition when solving complicated problems. He once said "Average is a choice", when discussing the many ways one could analyze their data. This phrase has stayed with me, reminding me to explore every idea and strive to be the best scientist I can be. He also taught me, after much trial and error, how to write and talk about science in a precise and engaging way. I am also deeply appreciative of his support in allowing me to pursue my scientific interests, including the risky decision to do experimental work toward the very end of my PhD. I have never met, and likely will never meet, a scientist as positive and enthusiastic about research as Kevin. I am so grateful that he agreed to the (somewhat) crazy idea of letting me do experiments in his lab. I will never forget showing him a set of culture plates that were clearly contaminated. He said something along the lines of, "Don't worry, there are millions of bacteria in a single droplet, some are bound to end up where they shouldn't." After our research meetings I would always feel so encouraged and motivated, even when things were not working. I wish I had had more time to discuss research with him, but I hope he is nevertheless proud that we were able to finally finish the biofilm paper.

I was also very fortunate to receive guidance from two other exceptional mentors, Prof. Luis Zaman and Prof. Kelsey Hallinen, who stepped in when I needed the most. With them I learned how to think as an experimentalist. They also never let me give up, even when the data suggested that we needed to completely rethink our approach.

I would also like to acknowledge my Master's advisor, Prof. Frederico Borges de Brito, for teaching me how to do research. When I was applying to graduate schools in the US, he suggested I consider working with Jordan, who had just been hired at a university I had never heard of: the University of Michigan. Looking back, I cannot imagine a better place to have lived and completed my studies, and I feel very lucky to call Ann Arbor home.

During my studies, I received extensive support from the Physics Department, the Biophysics Department, and the Center for the Study of Complex Systems at the University

of Michigan. I am grateful to the staff, students, and professors who supported me along the way and provided opportunities for my professional growth beyond research. In particular, I would like to acknowledge the Physics Department and its donors for awarding me the Norman E. and Mary E. Barnett Fellowship, which allowed me to focus fully on my experimental work.

I am grateful to all past and current members of the Horowitz group, it was an honor to share the graduate experience with you: Qi, Freddy, Seoyoung, Hyun-Myung and Sean. I especially thank Sean, who taught us many great coding techniques and with whom I greatly enjoyed collaborating. I am forever in debt to all members of the Wood group for taking a rookie scientist in and being so patient even after I broke so many things in the lab. I am particularly grateful to Keanu, who traveled just to teach me how to do experiments and whose cheerfulness is beyond contagious. And to Marlis, who taught me so many cool things about microscopy and biology.

During my graduate studies I decided I needed to learn how to become a better teacher. Joining Prof. Marisa Eisenberg's teaching team was one of the most enjoyable experiences I have had. When developing the Complex System's 100 course, I learned fascinating facts about how complexity shapes our everyday lives. I was also lucky to have the best co-GSI that I could have asked for, Conrad. Teaching young students that coding is cool was not easy, even with the help of coding ducks, but I need to admit that we had so much fun together teaching this class, and I am so proud that we also got a prize for it.

I am so thankful for all the friendships I built during my years studying Physics. All the CoPhIE cold baristas: Claire, Cynthia, Nora, Max, Ruiqi, and Saaj, you all showed me that there is space for everyone in the world of Physics. And the hot baristas: Andrea, Sarahi, Haley, Sara and Trisha, I know you will take great care of this amazing community we built. In particular, I thank Cynthia and Claire for inspiring me to fight for the things I believe in, and for our good times planning CUWiP. I had much joy sharing tea and academic dreams with Sabina during the last hard months of my PhD. My classmates of the IFSC class of 2016, we are now spread across the globe, pursuing all kinds of careers. I am so proud of all of us. Clara, the most patient and kind friend, we had so much fun in our Advanced Physics Laboratory. Although I am far away now, I cannot wait to visit her new house.

Thank you to my friends who took time to come to my weeding in a cold and snowy day: Bineet, Kolya, Zhanar, and Zhibek. Zhanar and Zhibek you both bring joy wherever you go, thank you for making Ann Arbor feel like home. Your attitude toward life and confidence remind me how to live fully, and, of course, to take plenty of photos along the way. I see many fun shopping trips in our future, including searches for almost sold-out Trader Joe's bags.

I would not be here if it weren't for my family. Thank you, Mom, for always keeping me going, even when I wanted to give up in my first year of undergrad. Mom dedicated her life to taking care of our family, and I say with no doubt in mind that I had the most wonderful childhood: surrounded by books, nature, and a love for knowledge. Thank you, Dad, for teaching me Math and Physics and for showing me, by example, the value of hard work. Thank you both for being so patient with me, making my education a priority, taking me over to compete in so many science olympiads, and getting me the best dog in the world, Lili. I am so lucky that growing up, I had the company of my favorite (and only) brother, Lucas. His clever humor and sometimes unhinged comments light up any room he enters. His curiosity and intelligence continue to amaze me every day. I am so proud of the career he is building for himself, even though it means we are far away from each other. Although we are all grown up now, I miss our carefree afternoons playing in the garden and enjoying the delicious snacks Mom prepared. Thank you, Mom, Dad, Lucas, and Lili, for loving me unconditionally even when I was so stressed about grades.

At last, but most definitely not at least, I would like to thank my husband, Alisher. Alisher has been my porto seguro since the early steps of my PhD. It was wonderful sharing all the ups and downs with him along the way, and I will always treasure the late nights we spent working together. Thank you for getting me my computer monitor, which made working at home much more enjoyable. Thank you for keeping me going when I felt I could go no further. Thank you for all our long walks spotting cats, the coffee shop visits that warmed my soul in the cold Michigan winters, for introducing me to the joy of attending live concerts and to many cool bands, for teaching me how wonderful it is to make scientific figures using Adobe Illustrator, and for always checking my citation count. Witnessing your productivity in graduate school was incredibly inspiring, and your dedication and work ethic motivate me every day. I feel so fortunate that I also get to share the love and kindness from your Mom and Granny. I love sharing my life with you.

TABLE OF CONTENTS

DEDICATION ii

ACKNOWLEDGEMENTS iii

LIST OF FIGURES viii

LIST OF TABLES xv

LIST OF ACRONYMS xvi

ABSTRACT xvii

CHAPTER

1 Overview **1**

2 Bounds on Nonequilibrium Response **4**

2.1 Introduction 4
2.2 Graphical representations of Markov-jump processes 6
2.2.1 Graphical solution for the steady-state distribution 8
2.3 Nonequilibrium response 10
2.4 Bounds on the nonequilibrium response of state observables 13
2.4.1 Single-edge symmetric perturbation 15
2.4.2 Multiple-edge symmetric perturbation 21
2.4.3 Asymmetric and arbitrary perturbations 24
2.5 Topologies with optimal response 26
2.6 Relaxing the bounds 27
2.7 Bounds on the nonequilibrium response of currents 28
2.8 Applying the bounds to receptor binding models 29
2.9 Derivations 34
2.9.1 Graphical solution for inhomogeneous linear equations 34
2.9.2 Constrains on the structural coefficients for the single-edge perturbation 38
2.9.3 Vertices of the convex polytope 43
2.9.4 Constrains on the structural coefficients for the multiple-edge perturbation 45
2.9.5 Bounds on covariance 47

2.10 Summary . . . 50

3 Cooperativity in Nonequilibrium Receptor Binding Models . . . 51

3.1 Introduction . . . 51
3.2 The role of cooperativity in equilibrium receptor binding models . . . 53
3.3 Definitions of cooperativity in nonequilibrium receptor binding models . . . 56
3.3.1 Energetics-inspired definition . . . 58
3.3.2 Dynamics-inspired definition . . . 59
3.3.3 What is the role of higher order cooperativity in nonequilibrium receptor binding models? . . . 60
3.4 Summary . . . 62

4 Cooperative Antibiotic Response in Bacterial Communities . . . 64

4.1 Introduction . . . 64
4.2 Experimental setup . . . 66
4.2.1 Bacterial strains . . . 66
4.2.2 Biofilm growth . . . 67
4.2.3 Data collection and image analysis . . . 67
4.3 Resistance spreads through a population inversion effect in biofilm and planktonic populations equally . . . 67
4.4 β-lactamase inhibition enhances resistance spread . . . 69
4.5 Biofilms are structurally amorphous as revealed by correlation analysis . . . 73
4.6 Modeling . . . 74
4.6.1 The minimal model . . . 74
4.6.2 The model with drug dynamics . . . 76
4.7 Summary . . . 80

5 Outlook . . . 85

5.1 Topology and thermodynamics bound nonequilibrium response . . . 85
5.2 Maximum nonequilibrium sensitivity does not require higher-order cooperativity . . . 85
5.3 Resistance subpopulations protect biofilm and planktonic populations equally 86

BIBLIOGRAPHY . . . 88

LIST OF FIGURES

FIGURE

1.1 Illustrative examples highlighting the study of response in biological systems across multiple scales. At the molecular scale, changes in ligand (yellow) concentration alter the number of ligands bound to a protein (green). At the cellular scale, mechanical perturbations of the cell (purple) wall trigger signaling pathways that regulate important cellular processes. At the community scale, changes in bacterial populations (green and purple) that modify ecological interactions can influence the behavior and composition of the entire community. 3

2.1 Representative example of a Markov-jump process. (a) Five-state house graph with perturbed edge e_{12} highlighted in pink. The transition rates are functions of a parameter λ that can be externally perturbed. (b) Cycles associated to the thermodynamic forces F_C. 7

2.2 Graphical representation of the Matrix-Tree Theorem Eq. (2.12) for the house graph Fig. 2.1. (a) All the spanning trees for the house graph. (b) The steady-state probability of any state i, in this case $i = 1$, is given by a normalized sum of all the weights of spanning trees rooted at vertex i (highlighted in pink). . . . 9

2.3 (a) For any tree T^{12} that contains e_{12}, adding directed edge $1 \to 2$ to the rooted tree T_1^{12} produces a subgraph with the same weight as that obtained by adding $2 \to 1$ to T_2^{12}. (b) For any rooted tree S_1^{12} that does not contain e_{12}, adding directed edge $1 \to 2$ creates a subgraph with a cycle in the clockwise direction. Adding $2 \to 1$ to S_2^{12} yields a subgraph that is identical except that the cycle is oriented in the counterclockwise direction. 10

2.4 An arbitrary nonequilibrium response can be expressed as a linear combination of three distinct components. (a) E-perturbations (also called equilibrium-like perturbations), (b) symmetric B-perturbations (also called kinetic perturbations), and (c) asymmetric F-perturbations. (a) An E-perturbation of state n corresponds to a uniform decrease in all exit rates from that state. (b) A symmetric perturbation between states m and n corresponds to a uniform increase in both the forward and backward transition rates between the two states. (c) An asymmetric perturbation between states m and n corresponds to an increase in the forward rate and an equal decrease of the backward transition rate between the two states. (d) Assuming the system admits a well-defined energy landscape, it is possible to develop an intuitive understanding for each type of perturbation. E-perturbations are equivalent to changes in the energy of a state. Symmetric perturbations correspond to changes in the energetic barrier between states. Asymmetric perturbations correspond to shifts in the driving forces. 14
2.5 Graphical representation of the solution to Eq. 2.37. (a) All 2-forests for the house graph (Fig. 2.1). (b) For a symmetric edge perturbation on edge e_{12}, the response of π_3, is composed of two terms, a positive one, which is a sum of weights of all rooted 2-forests $f_l^1 \sqcup f_3^2$ (both roots are highlighted in pink), and a negative one, which is a sum of weights on all rooted 2-forests $f_3^1 \sqcup f_l^2$. 16
2.6 (a) Triangle graph with perturbed edge $\bar{e}_{12}$ (highlighted in pink). (b) 2-forests $\mathcal{F}^{12}$. (c) Feasible polytope: The only structural coefficients that are not trivially zero are P_{12}, P_{13} and P_{32}. As there is only one linearly independent equality constraint, $P_{12} = P_{13} + P_{32}$, the feasible polytope has dimension $d = 2$. Its vertices are the trivial case $(0, 0, 0)$, as well as $(1, 1, 0)$ and $(1, 0, 1)$ that are each associated to a 2-forest. 20
2.7 Representation of the topologically-consistent splitting of the vertices, $\mathcal{V}^{12}$, for the house graph (Fig. 2.1). The set V^1, highlighted in pink, contains vertex 1, and V^2, highlighted in blue, contains vertex 2. 21
2.8 Response ratio $\mathcal{R}_B$ as a function of the maximum cycle force $\mathcal{F}_{\max}$ around cycles containing edge e_{12} of the house graph (Fig. 2.1) for 15000 rate matrices with the logarithmic asymmetric $\ln(W_{ij}/W_{ji})$ and symmetric $\ln(W_{ij}W_{ji})$ parts sampled uniformly on $[-7, 7]$ and the observable Q_i sampled uniformly on $[-4, 4]$. All samples (gray) fall below the predicted bound $\tanh(\mathcal{F}_{\max}/4)$ (red). 22
2.9 (a) Multi-edge perturbation in a generic graph: all edges (pink) in the subgraph H^{mn} (gray) are perturbed uniformly. Removing all edges of the cut-set K^{mn} (green) splits the graph into two separate subgraphs. The probability current $\bar{J}^H$ (blue arrows) flowing in and out of H^{mn} is due to cycles $\mathcal{C}^H$ that straddle the perturbed and unperturbed regions. (b) Representation of a multi-edge perturbation for the illustrative graph. All edges in the subgraph H^{12}, highlighted in gray, are uniformly perturbed. (c) Cycles that count towards determining $\mathcal{F}_{\max}$ in the case of multi-edge perturbation of H^{12}. Note that the cycle $\{1 \to 2 \to 5 \to 1\}$ is not relevant in this case, as it is internal to H^{12}. 24

2.10 Example of an optimal network topology inherited from the topologically-consistent splitting $V^1 = \{1,3,4\}$, $V^2 = \{2,5\}$. The rates on edge e_{15} are set to zero cutting that edge from the graph, leaving the system with a unique cycle. States internal to the islands defined by the topological splitting are contracted into a pair of single nodes by taking the rates along edges internal to the islands (orange) to be fast compared to the rates connecting the islands (dashed). 27
2.11 Response $\partial_{B_{12}} \ln \bar{J}_{12}$ as a function of the maximum cycle force $\mathcal{F}_{\max}$ around cycles containing edge e_{12} of the house graph (Fig. 2.1) for 1500 rate matrices with the logarithmic asymmetric $\ln(W_{ij}/W_{ji})$ and symmetric $\ln(W_{ij}W_{ji})$ parts sampled uniformly on $[-7,7]$. All samples (gray) fall between the predicted upper (blue) and lower (red) bounds. 30
2.12 Representation of a ligand receptor model with two binding sites. Ligands (yellow) bind to a receptor (green) with $N_B = 2$ binding sites. Only the binding rates (pink) are proportional to the ligand concentration c. 31
2.13 Decomposition of a c-perturbation into E-perturbations and a multi-edge B-perturbation for ligand receptor model with two binding sites following the graphical notation for the different types of perturbation illustrated in Fig. 2.4. 31
2.14 Saturating the inequalities in receptor binding: (a) Representation of the optimal network corresponding to the topological consistent splitting is $V^2 = \{1,4\}$, $V^2 = \{2,3\}$. The rates internal to the islands (pink and blue ovals) are fast compared to the rates connecting the islands (dashed). (b) For the optimal network in (a), the deviation of the response from the equilibrium prediction (gray) is compared to the bounds imposed by Eq. 2.92 (dashed dark red), Eq. 2.93 (orange) and Eq. 2.94 (red) as a function of concentration c for two observables $f = n/2$ (top) and $f = \delta(V^2)$ (bottom) at two values of thermodynamic driving, $\Delta\mu/kT = 1$ (left) and $\Delta\mu/kT = 5$ (right). (c) $\langle f \rangle_c$ as a function of c for both observables at the two values of thermodynamic driving. Parameter values are listed in Table 2.1. 33
2.15 Nonequilibrium response in the receptor binding model: (a) Normalized response for 15000 random rate matrices with $c = 1$, logarithmic asymmetric $\ln(k_\alpha/\tilde{k}_\alpha)$ and symmetric $\ln(k_\alpha \tilde{k}_\alpha)$ parts sampled uniformly on $[-7,7]$, and $f_1 = 0$, $f_3 = 1$, with $f_2 = f_4$ uniform in $[0.4, 0.6]$. All samples fall below the predicted bound Eq. 2.97, red. Green line is the maximum equilibrium response 2. (b) $\langle f \rangle_c$ as a function of c/K for three distinct rate matrices [purple points (a)] with $\Delta\mu/kT = 2$, which need not be Hill functions. Orange curve corresponds to the optimal Hill function Eq. 2.98. Inset: for any $\langle f \rangle_c$ sensitivity is bounded by the steepness of the Hill function, with a maximum of $H/4$. Parameters are listed in Table 2.2. 35
2.16 Example application of the *Root-Swap* map taking the pair $(T_3, f_1^1 \sqcup f_5^2)$ as input and outputting the pair $(T_5', f_1'^1 \sqcup f_3'^2)$. Each panel contains one step of the *Edge-Swap* operation. 41

3.1 Hill curves (Eq. 3.1) for different values of the Hill coefficient: 1 (blue), 2 (pink) and 4 (red), and dissociation constant $K = 1$. When the fractional occupation $\langle \Theta \rangle$ is zero the macromolecule is empty, when its one all the sites of the macromolecule are occupied. Higher Hill coefficients correspond to increased steepness of the curve. 52

3.2 Diagrammatic representation of states and energies for a receptor binding model with three-binding sites. The receptor is shown in green, and the bound ligands in yellow. The chemical potential, μ, represents the effective energy cost of removing a ligand from the reservoir and binding it to the receptor. J_{12}, J_{13}, and J_{23} are measures of pairwise cooperativity, and J_{123} is a measure of higher-order cooperativity capturing the interaction between all three sites. Without loss of generality the energy of the empty receptor is set to zero. Note that although the binding sites are represented identically, sites can assume different energies. . 54
3.3 Graph representing a nonequilibrium receptor binding model with three binding sites. The binding rates (pink) correspond to transitions that lead to the binding of a ligand. The state notation follows the definition used in Fig.3.2. 58
3.4 (a) For the three-binding site case, the maximum value of $\partial_{\ln\Theta}\langle n\Theta\rangle/\langle\Theta\rangle(1-\langle\Theta\rangle)$ is 7, and the numerical sampling strategy only recovers values slightly above 5. To generate the plot, 5×10^7 sets of rates were sampled with $\ln(W_{S,S'})$ drawn uniformly from the $[-17,17]$ interval. For visualization purposes, only 15,000 samples were plotted. Of these, 10,000 points were randomly selected from the interval $[0,3]$, and another 4,995 points were randomly selected from the interval $[3,7]$. All the five values above 5 were plotted. It should be noted that uniform sampling in log-rate space does not translate into uniform sampling in the space of responses, which is reflected in structured distributions of sampled values in the plots.(b) A greedy search algorithm reaches the maximum sensitivity for a three-binding site receptor model. Initial rate values are chosen at random, orange dots, and only moves that increase the ratio $\partial_{\ln c}\langle\Theta\rangle/\langle\Theta\rangle(1-\langle\Theta\rangle)$ are accepted. Each optimization run is terminated after 10^6 steps, with final values indicated by orange stars. Individual optimization trajectories through the rates state space are shown as gray lines. To generate the figure, 200 independent runs were initiated, of which 20 are shown for visualization purposes. 61
3.5 Identified counterexamples of three-binding site models that reach the maximum expected sensitivity with no higher-order cooperativity, for the energetics-inspired (a) and dynamics-inspired definition (b). The legend indicates the color coded values for the rates. 62

4.1 *E. faecalis* exhibits cooperative resistance to β-lactam antibiotics. (a) Ampicillin-resistant bacteria, shown in green, produce β-lactamase, an enzyme that inactivates ampicillin through hydrolysis. Although β-lactamases remain cell-associated, resistant bacteria effectively act as antibiotic sinks by degrading the drug. If the antibiotic concentration in the vicinity of a resistant cell falls below the MIC, sensitive cells, in magenta, can grow within this zone of protection. Sulbactam is a β-lactam drug commonly used in combination with ampicillin in clinical settings. Sulbactam has no toxic effects, however it binds irreversibly to β-lactamases, acting as a competitive inhibitor to ampicillin and decreasing the ability of resistant bacteria to degrade the drug. (b) The drug concentration profile is calculated by solving the 1D diffusion equation for a single resistant bacteria acting as a sink, with a fixed drug concentration at infinity. The zone of protection is defined as the distance from a resistant cell for which the drug concentration is below the MIC. The addition of sulbactam effectively decreases the zone of protection. 66

4.2 *E. faecalis* populations growing in the presence of ampicillin and sulbactam undergo significant compositional changes that depend on drug concentration and initial population composition. Diagram illustrating the experiment. A mixture of florescent ampicillin-sensitive and ampicillin-resistant *E. faecalis* bacteria, prepared at a defined density and ratio, is added to a glass-bottom well containing liquid growth media supplemented with drugs. After a 24 hour incubation period at 37 the biofilm is imaged directly in the glass-bottom well using confocal fluorescence microscopy. During incubation the well is kept undisturbed with no liquid media or antibiotics replenishing. The biofilm is imaged though its full thickness along the vertical axis by capturing 25 optical slices of dimensions 80 m x 80 m separated by 2.5 m. A 20 sample of the planktonic population is extracted and mounted on a glass slide for imaging using confocal fluorescent microscopy. . 69

4.3 Representative images (densest slice) of mixed ampicillin-resistant (green) and ampicillin-sensitive (magenta) biofilms after the incubation period. Initial bacterial density, initial resistant:sensitive ratio, as well as ampicillin and sulbactam concentrations were varied to examine effects on final population composition. All panels are shown at the same scale. 70

4.4 Spread of resistance by a population inversion effect as demonstrated by measurements of the final resistant fraction of bacteria as a function of the initial resistant fraction in the biofilm (panels a and d) and in the planktonic (panels b and e) populations. The non-monotonic dependence between final and initial resistant fractions is modulated by the initial number of bacteria in the system (for biofilm data compare panels a and d, for planktonic data compare panels b and e) with higher resistant fractions observed at the lower OD value of 0.001. Both biofilm and planktonic populations have the same final composition as seen by visualizing the final resistant fraction in the biofilm in terms of the final resistant fraction in the planktonic (panels c and f). 71

4.5 The combined use of ampicillin and sulbactam exacerbates the spread of resistance in the biofilm and planktonic populations. Sulbactam has no intrinsic toxic effects to the cells, when used by itself final resistant fractions are the same as for the no drugs case scenario for both OD 0.01 and 0.001 (panels a and d). Ampicillin was used in combination with sulbactam at two distinct concentration values, Amp.1 m-Sulb.1 m (cyan) and Amp.1 m-Sulb.2 m (purple). For both OD 0.01 (panel b) and OD 0.001 (e) the resulting final fraction is higher than the final resistant fraction with only Ampicillin at 1 m. Similarly to the only Ampicillin cases, both biofilm and planktonic populations have the same final composition (panels c and f). 72
4.6 Correlation analysis reveals that the biofilm does not exhibit spatial structure. (a) The metric used to quantify structure is analogous to a cumulative radial distribution function, quantifying differences between the relative positions of resistant bacteria in respect to sensitive bacteria in the data and in its randomized version. Values equal to one indicate that the biofilm lacks spatial structure, as the relative positions are the same as in a completely random scenario. Values above one indicate an increase in the number of resistant cells close to sensitive cells in relation to the random scenario, and values below one indicate a decrease. (b) For all initial resistant fractions and values of drug concentrations, the correlation metric has the same qualitative behavior with small quantitative shifts. 75
4.7 Phase plane of the dynamical system defined by Eqs. 4.2 and 4.3. The intersection between the nullcline of Eq. 4.2, in magenta, and Eq. 4.3, in green, defines the single fixed point of the system, in red. The values of the parameters used to generate this plot are $b_S = b_R = 1 = d_S$, $d_R = 0.5$, $C = 3$, $K = 1$ and $n = 2$. 76
4.8 Diagrammatic representation of the well-mixed model used to reproduce the observed spread of resistance within the biofilm. Sensitive and resistant cells consume glucose and grow at a rate that scales hyperbolically with its concentration. Ampicillin causes cell death, with resistant cells requiring substantially higher drug concentrations to reach half-maximal death rates compared with sensitive cells. Resistant cells produce intracellular β-lactamase, which degrades ampicillin. Sulbactam, while not toxic to cells, binds β-lactamase and competitively inhibits ampicillin degradation, thereby reducing its efficacy. 77
4.9 Time dynamics of the model variables for two different initial resistant fractions, 0.2 and 0.05. Ampicillin and sulbactam are continuously degraded as the population of resistant bacteria increases. Once both drug concentrations reach zero, bacterial death stops and the population only grows. As bacteria grow, the glucose concentration also decreases and once it reaches zero, growth ceases. When both glucose and drug concentrations reach zero, the system reaches steady-state. The dynamics are generated using parameters obtained from the fitting procedure, with values specified in Fig. 4.10. 81

4.10 Comparison between data and model predictions for initial OD 0.01, panels a and b, and initial OD 0.001, panels c and d. Data is shown in full lines and model predictions in dashed lines. The model is able to accurately predict final resistant fractions for ampicillin only data, panels b and d. With the addition of sulbactam, the model is not able to predict exact final resistant fractions, but it captures the increase in final resistant fractions. The values used to generate the plots are list in Table 4.1. 82
4.11 Number of sensitive and resistant bacteria in the biofilm as a function of the initial resistant fraction for different values of antibiotic concentrations. The experimental data, in full lines, quantifies the total population in a 80 m x 80 m x 60 m volume averaged over 5 distinct regions and 3 experimental replicas. The fitted data, in dashed lines, reproduce the observed data well, showcasing only an overestimation of resistant bacteria for higher drug concentrations. The total number of sensitive bacteria with no drugs and initial optical density of 0.001, green line in panel c, is used to fit the model parameters $\tilde{b}$ and $\tilde{Y}$, as well as the initial values $\tilde{S}_0 + \tilde{R}_0$, and $\tilde{g}_0$. 83

LIST OF TABLES

TABLE

2.1 Rate constants for the optimal network topology in Fig. 2.14. The values of the rates are chosen to fix the thermodynamic driving $\Delta\mu/kT = \{1, 5\}$. A multiplicative factor is included in the rates internal to the islands, $\varepsilon = 10^4$, in order to impose a timescale separation between transitions internal to the islands relative to between islands. 34

2.2 Rate constants and the observable values for the purple points 1, 2 and 3 in Fig. 2.15(a). The values are chosen so that the cycle force is equal to 2 in all cases. Note that in Fig. 2.15(b) the value of c for which $\langle f \rangle_c$ is equal to 0.5 depends on the rate constants. In the interest of creating a clear visualization, we numerically find these values, which we denote as K and plot each curve as a function of the normalized concentration c/K. 36

4.1 Fitted values of the nondimensionalized parameters and initial conditions of the model. 81

LIST OF ACRONYMS

FDT Fluctuation-Dissipation Theorem

MTT Matrix-Tree Theorem

MIC Minimum Inhibitory Concentration

ABSTRACT

In biological systems, response to changes in the environment are manifested across different scales, from the molecular reaction level to multicellular communities. In this Dissertation, we explore systems on opposite extremes of this spectrum. At the molecular level, we show how an arbitrary response in nonequilibrium mesoscopic stochastic systems is constrained by fluctuations of a topological variable and enhanced by nonequilibrium driving. When applied to receptor binding models, this result reveals that, as in equilibrium, sensitivity is constrained by a Hill function, while the Hill coefficient can be enhanced by the nonequilibrium driving beyond its equilibrium limit. In equilibrium, reaching maximum Hill coefficients requires strong pairwise cooperative interactions. Motivated by this, we introduce two nonequilibrium cooperativity definitions and show that pairwise interactions are also sufficient to reach maximum nonequilibrium Hill coefficients. At the other end of the scale, we study how strongly coupled planktonic and biofilm *E. faecalis* populations respond to antibiotic stress. Resistant strains respond to drug exposure with enzymatic degradation of the antibiotic molecule, notably leading to cooperative interactions within the population. Resistance is experimentally observed to spread through the community by a population inversion effect, characterized by a non-monotonic relation between initial and final fractions of resistant strains. The observations are captured by a simple well-mixed consumer-resource model with competition mediated by resource sharing and cooperation arising from global toxin degradation.

CHAPTER 1

Overview

This Dissertation covers two conceptually distinct topics and includes theoretical and experimental work. Although both topics differ in nature, they are unified by a common thematic: response in biological systems. Here, response is understood broadly as the change a system undergoes when subjected to an external perturbation. Studying response is valuable for two main reasons. First, living organisms are constantly sensing and responding to changes in their environment. Second, a system's response encodes information about its underlying structure and dynamics.

Thus, analyzing a system's response, both in and out of equilibrium, provides a powerful method for understanding its properties. Examples can be found in physics, where material properties, such as diffusivity and viscoelasticity, serve as fundamental parameters for describing the behavior of materials, including complex soft matter systems [1, 2]. In biology, a complementary example is the use of sensitivity to chemical inputs as a key performance measure for a variety of biophysical processes, from biochemical sensing [3, 4] to gene transcription [5, 6]. Response can be investigated across multiple levels of biological organization, which may be broadly categorized as molecular, cellular, and community scales, see Fig. 1.1. In this Dissertation, we study response at the molecular and community scales.

We start by investigating response at the molecular scale in Chapter 2. For systems in equilibrium, response is directly linked to fluctuations through the Fluctuation-Dissipation Theorem (FDT) [1]. The FDT states that the strength of a system's response to an external perturbation is constrained by the thermal fluctuations of the unperturbed system: strong response requires large fluctuations. Biological systems operate far from thermodynamic equilibrium, driven by continuous energy fluxes. Although the FDT no longer holds in this case, the notion that fluctuations constrain response still extends to nonequilibrium systems. Guided by this principle, we prove a Fluctuation-Response Inequality that bounds arbitrary responses in terms of topology and strength of nonequilibrium driving. The topology we refer to is that of the system's state space and determines which transitions between states

are allowed. Our results hold for any mesoscopic stochastic system with discrete states.

This result proves itself valuable for rationalizing the physical limits on the steepness of binding curves. The binding of a ligand to a receptor is a ubiquitous biological process, playing a central role in regulating cellular function. Its characteristic binding curve describes how the average occupancy of the receptor varies with ligand concentration. The steepness of the curve determines the system's sensitivity to changes in concentration, a property traditionally quantified through the Hill coefficient. At equilibrium, the Hill coefficient is constrained by the number of binding sites in the macromolecule. In the case of a receptor with two binding sites, our bounds show that driving the system out of equilibrium enhances the Hill coefficient beyond its equilibrium value, allowing it to reach values of up to three.

Before turning to the study of response beyond the molecular scale, in Chapter 3 we discuss cooperativity in the context of receptor binding models. Cooperativity quantifies the interaction between different binding sites, where the binding of a ligand at one site can influence the binding of ligands at other sites. This includes pairwise cooperativity, which describes interactions between two sites, as well as higher-order cooperativities, involving interactions among three or more sites. Cooperativity is important because it sharpens binding curves, thus enhancing the system's sensitivity to changes in ligand concentration. At equilibrium, only pairwise cooperativity is required for the system to reach its maximum sensitivity. In nonequilibrium systems, however, the notion of cooperativity remains elusive because interactions between sites can depend on details of the system's dynamics. We introduce two definitions of nonequilibrium cooperativity, one inspired by energetics and the other by dynamics. According to these definitions, akin to what holds in equilibrium systems, higher-order cooperativities are not required for a nonequilibrium receptor binding system to reach maximum sensitivity.

In Chapter 4, we shift focus to study responses at the community scale. The system under investigation is a bacterial community and the external perturbation is exposure to antibiotics. The response then manifests as a shift in the population composition. *Enterococcus faecalis*, the model organism employed in this study, is a non-motile, Gram-positive opportunistic pathogen that plays a significant role in hospital-acquired infections and often exhibits resistance to multiple antibiotic classes.

A common resistance mechanism in *E. faecalis* is enzymatic degradation, where bacterial enzymes inactivate the antibiotic [7]. This mechanism not only protects the bacteria that produce the enzymes, but also provides collateral resistance to antibiotic sensitive neighbors. By degrading the drug, resistant bacteria act as sinks that lower local antibiotic concentrations, allowing sensitive cells to survive. This interaction between resistant and sensitive bacteria, which we refer to as a drug-induced cooperative interaction, has been

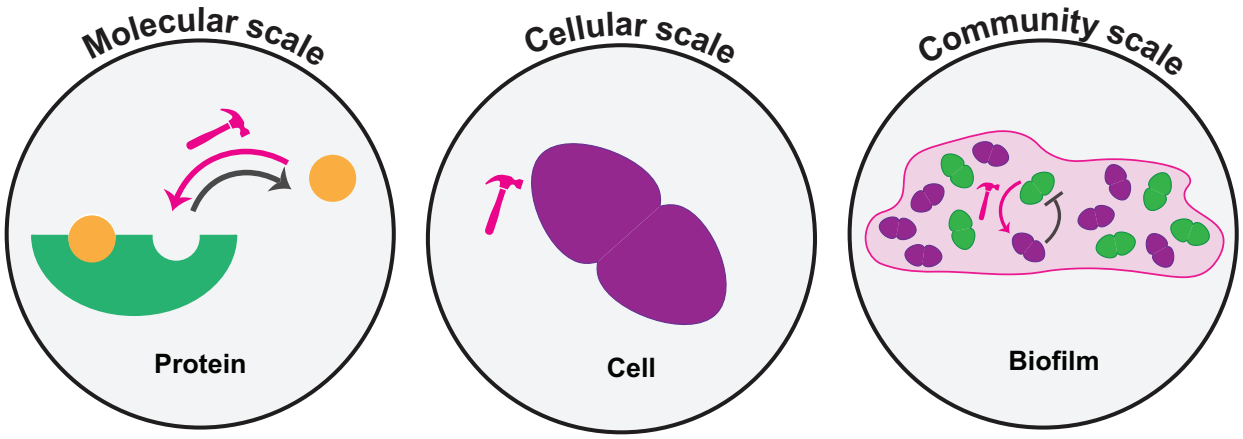


Figure 1.1: Illustrative examples highlighting the study of response in biological systems across multiple scales. At the molecular scale, changes in ligand (yellow) concentration alter the number of ligands bound to a protein (green). At the cellular scale, mechanical perturbations of the cell (purple) wall trigger signaling pathways that regulate important cellular processes. At the community scale, changes in bacterial populations (green and purple) that modify ecological interactions can influence the behavior and composition of the entire community.

reported to restore sensitive subpopulations in mixed cultures across different species and antibiotics [8, 9, 10, 11]. These experiments were conducted with planktonic cells, which are bacteria that exist as individual, free-floating cells in a liquid environment. Bacteria, however, also commonly form structured, surface-attached communities known as biofilms [12]. The physiological and structural complexity of biofilms raises the question of whether drug-induced cooperative interactions differ between planktonic and biofilm populations. Here, we show that the population shifts induced by antibiotic stress are equivalent in both planktonic and biofilm populations.

CHAPTER 2

Bounds on Nonequilibrium Response

This Chapter is based on published work by G. Fernandes Martins and J. M. Horowitz [13].

2.1 Introduction

Linear response theory provides a framework to predict how a system's observables respond to small, externally applied perturbations, and to connect these responses to the intrinsic properties of the unperturbed system. Consider an equilibrium system that is subject to a small time dependent perturbation $\lambda(t)$ starting at time 0. We assume the system has a number of mesoscopic states i, then the perturbation alters the energy of each state from E_i^{eq} to $E_i = E_i^{\text{eq}} - \lambda(t)V_i$. $V_i = -\partial_\lambda E_i$ is the conjugate variable to the perturbation with respect to the energy. The resulting change in the average value of an observable Q at time t, $\langle Q(t)\rangle$, due to this small perturbation is written as

$$\delta\langle Q(t)\rangle = \int_0^t R_{Q,V}(t-s)\lambda(s)ds, \tag{2.1}$$

where $R_{Q,V}(t-s)$ is the linear response function. If the system is initially in equilibrium at inverse temperature β, statistical physics predicts the response function to take the format

$$R_{Q,V}(t-s) = \beta\frac{d}{ds}\langle Q(t)V(s)\rangle^{\text{eq}}, \tag{2.2}$$

where $\langle Q(t)V(s)\rangle^{\text{eq}}$ denotes the equilibrium average between the values of the observable at time t and the conjugate variable at time s. Equation (2.4) is the celebrated Fluctuation Dissipation Theorem (FDT). The FDT operates as a powerful organizing principle: the spontaneous fluctuations of a system in equilibrium and its response to small external perturbations encode the same information.

The FDT does not hold for arbitrary small perturbations around a nonequilibrium steady state. Because many systems of interest operate far from equilibrium, research over the

past decades has been prolific in developing extensions of the FDT aimed specifically at describing fluctuations and responses in nonequilibrium systems. In particular, a sought-after formulation is one that mirrors the structure of the FDT,

$$R_{Q,V}(t-s) = \frac{d}{ds}\langle Q(t)B(s)\rangle, \tag{2.3}$$

where the average is now taken over the nonequilibrium steady state, and B is an observable related to the system's dynamics. Early work by Agarwal [14], followed by Seifert and Speck [15], identified B as a variable conjugate to the entropy production – a measure of irreversibility of the system's dynamics. Since nonequilibrium steady-state distributions are generally unknown for arbitrary systems, applying this modified version of the FDT becomes challenging for cases more complex than a single particle system.

An alternative approach is to determine the extent to which the FDT is violated when a system is driven out of equilibrium. Baiesi, Maes and Wynants show in [16] that the response function takes a similar form to the FDT

$$R_{Q,V}(t-s) = \frac{\beta}{2}\frac{d}{ds}\langle Q(t)V(s)\rangle - \frac{1}{2}\frac{d}{ds}\langle Q(t)A(s)\rangle, \tag{2.4}$$

with the addition of a term that depends on the system's kinetic activity, A – which quantifies how dynamically active the system is. Following an alternative approach, Harada and Sasa [17] showed that, in what is now known as the Harada–Sasa equality, the extent to which the FDT is violated directly quantifies the average rate of energy dissipation into the environment.

Another prominent class of results are Fluctuation Theorems, which characterize nonequilibrium averages of fluctuating quantities in terms of physical variables containing clear thermodynamic interpretation. A well known example is the Jarzynski equality, a nonequilibrium work theorem that relates the free energy difference between two states to the average work performed along all possible trajectories connecting both states [18]. Beyond the Fluctuation Theorems, a set of inequalities has recently been discovered that constrain the fluctuations of currents – directional flows of physical quantities. This inequalities are coined the Thermodynamic Uncertainty Relations, and establish a universal trade-off between the precision of nonequilibrium currents and the thermodynamic cost required to sustain them [19, 20]. Written explicitly, the relation states that the fluctuations of a current measured as its variance, $\mathrm{Var}(J)$, is constrained by the entropy production rate, denoted Σ, as

$$\frac{\mathrm{Var}(J)}{\langle J\rangle^2} \leq \frac{2}{\Sigma}, \tag{2.5}$$

with $\langle J \rangle$ the average current value.

Inspired by this approach of identifying inequalities that delineate the limits of possible behavior, we build on a recently established class of thermodynamic bounds on nonequilibrium response [21, 22, 23, 24]. In particular, we derive a Fluctuation-Response Inequality and demonstrate that the response of a physical observable is bounded not just by thermodynamic driving, but also by a measure of fluctuations sensitive to the topology of its state space.

Our main theoretical tool is a graphical representation of mesoscopic nonequilibrium systems. Such graphical representations have been known for some time [25, 26], and in the last ten years have re-emerged as powerful tools for studying the links between kinetics and thermodynamics in nonequilibrium systems [27, 28, 29, 30]. Although in this Dissertation we make exclusive use of graph-theoretical methods, it is worth noting that the dynamics can also be solved using tools from linear algebra. As shown by Aslyamov et al. [31], these approaches provide alternative representations of the dynamics and yield interesting insights into the response properties of nonequilibrium systems [32, 33, 34, 35].

2.2 Graphical representations of Markov-jump processes

There are many ways to describe the dynamics of a nonequilibrium system. Throughout this Dissertation, we adopt the framework of continuous-time Markov chains, which have appeared in the literature under a variety of names, including Markov-jump processes, linear framework graphs [36], and kinetic schemes [37].

In this framework, a system is characterized by a collection of discrete states, or configurations, $i = 1, \ldots, N$. The dynamics are dictated by random transitions between the states, with rates W_{ij} to jump from $j \to i$. The system is memoryless, meaning that transition rates depend only on the current state and not on the past history of visited states or on how long the system has occupied that state. For thermodynamic consistency [38], every transition must be accompanied by its reverse. This implies $W_{ji} \neq 0$ whenever $W_{ij} \neq 0$.

The system's dynamics can then be visualized as occurring on a state-space graph, G, where the vertices $\{i\}$ represent the states and the undirected edges $\{e_{mn}\}$ represent allowed transitions in both directions. An example which will serve to illustrate our results is introduced in Fig. 2.1 – throughout this Chapter we refer to this graph as the house graph because of its characteristic shape.

For such models, the probability $p_i(t)$ for the system to be at state i at time t evolves

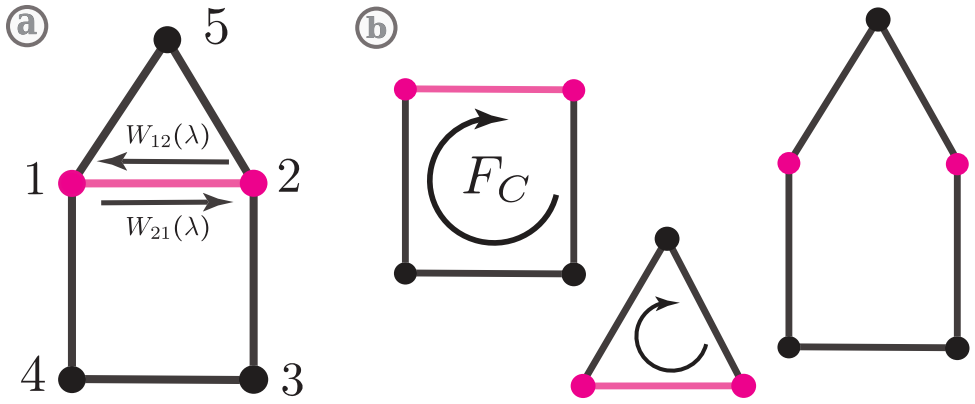


Figure 2.1: Representative example of a Markov-jump process. (a) Five-state house graph with perturbed edge e_{12} highlighted in pink. The transition rates are functions of a parameter λ that can be externally perturbed. (b) Cycles associated to the thermodynamic forces F_C.

according to the master equation [39]

$$\dot{p}_i(t) = \sum_{j=1}^{N} W_{ij} p_j(t), \tag{2.6}$$

where the diagonal elements $W_{ii} = -\sum_{j\neq i} W_{ji}$ enforce probability conservation. We assume that the graph G is strongly connected, which coupled with our assumption that every transition has a reverse, guarantees that $p_i(t)$ relaxes to a unique stationary distribution π_i given as the solution of

$$\sum_{j=1}^{N} W_{ij}\pi_j = 0. \tag{2.7}$$

Driven, or nonequilibrium dynamics are characterized by the emergence of nonzero steady-state probability currents between pairs of states,

$$\bar{J}_{ij} = W_{ij}\pi_j - W_{ji}\pi_i. \tag{2.8}$$

These flows are driven by thermodynamic forces, like temperature or chemical potential differences, and are linked to the dynamics by assuming local detailed balance [40, 41]. This allows us to identify these forces through the imbalances of the rates around cycles: sequences of edges that connect the initial vertex to itself without self-intersection (Fig. 2.1(b)). Then to each cycle $C = \{i_0 \to i_1 \to i_2 \to \cdots i_m \to i_0\}$ we identify a thermodynamic force, or affinity,

as the log-ratio of rates forwards and backwards around the cycle [25, 42, 38]:

$$F_C = \ln\left(\frac{W_{i_0 i_m}\dots W_{i_2 i_1} W_{i_1 i_0}}{W_{i_0 i_1} W_{i_1 i_2}\dots W_{i_m i_0}}\right). \tag{2.9}$$

When all cycle forces vanish, then necessarily all steady-state currents are zero ($\bar{J}_{ij} = 0$), and the system satisfies detailed balance,

$$W_{ij}\pi_j = W_{ji}\pi_i \tag{2.10}$$

which is a statistical symmetry characteristic of equilibrium. The cycle forces are therefore a natural measure of how far the steady state is from equilibrium.

2.2.1 Graphical solution for the steady-state distribution

The Matrix-Tree Theorem (MTT) [26, 43, 44] offers a powerful graphical method for solving the steady-state distribution of Markov-jump processes. The solution is built out of spanning trees, which are connected subgraphs of G that include all its vertices and contain no cycles. We illustrate all trees for the house graph in Fig. 2.2(a). For each tree we can choose a vertex, r, called the root, and orient all edges in the tree along the unique path towards that root. The resultant subgraph, we call a rooted spanning tree and denote it as T_r. To each rooted tree we assign a weight as the product of the weights of all its edges, $\{i \to j, \dots, k \to r\}$,

$$w(T_r) = W_{ji}\cdots W_{rk}. \tag{2.11}$$

The set of all spanning trees of a graph we denote as $\mathcal{T}$, and the sum over the weights of all trees as $w(\mathcal{T})$. Then the solution of the master equation Eq. (2.7) can be written as a sum over the weight of all spanning trees $\mathcal{T}$,

$$\pi_i = \frac{1}{\mathcal{N}}\sum_{\mathcal{T}} w\left(T_i\right), \tag{2.12}$$

with normalization constant $\mathcal{N} = \sum_{\mathcal{T},k} w\left(T_k\right) = w(\mathcal{T})$. This solution is illustrated in Fig. 2.2(b).

Equation (2.12) also leads to a graphical representation of the steady-state currents. This representation is obtained by substituting Eq. (2.12) into the definition of $\bar{J}_{mn}$ (Eq. (2.8)),

$$\bar{J}_{mn} = \frac{1}{\mathcal{N}}\sum_{\mathcal{T}}\left[W_{mn} w(T_n) - W_{nm} w(T_m)\right]. \tag{2.13}$$

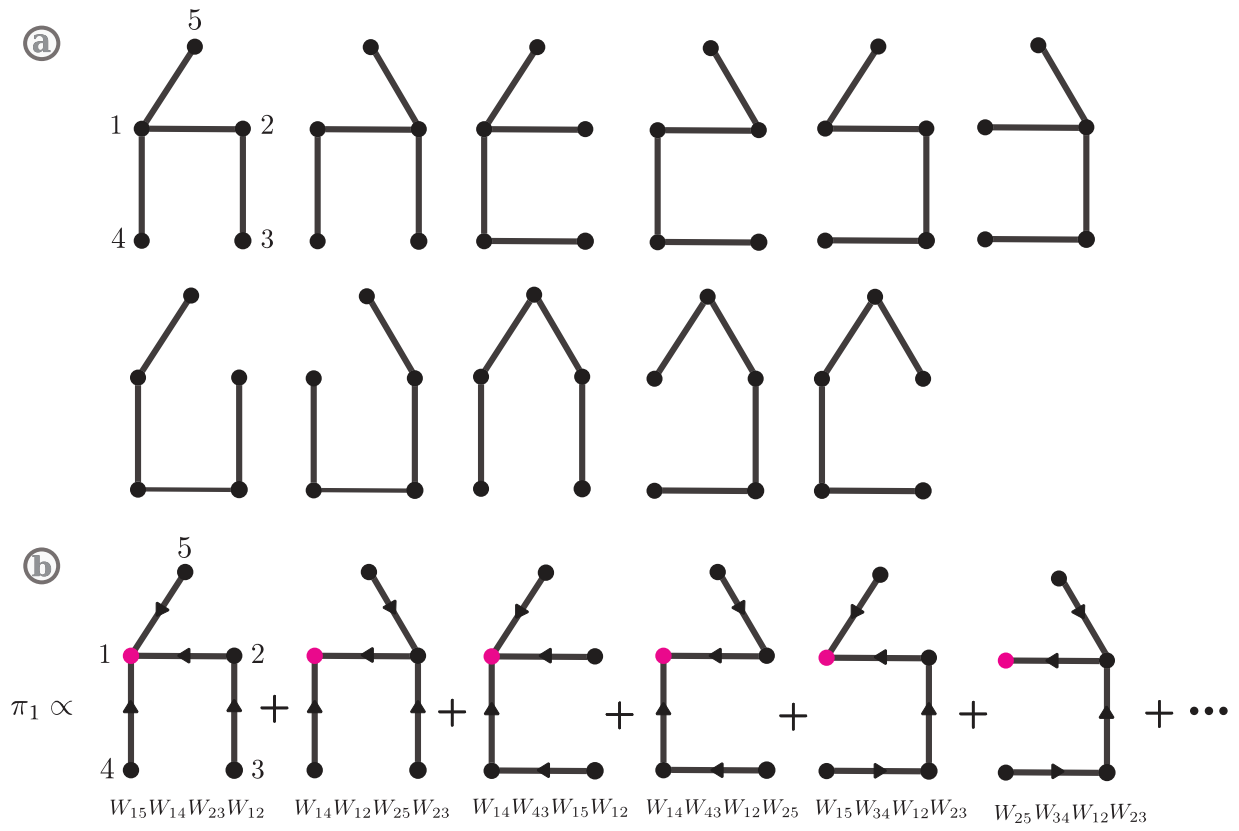


Figure 2.2: Graphical representation of the Matrix-Tree Theorem Eq. (2.12) for the house graph Fig. 2.1. (a) All the spanning trees for the house graph. (b) The steady-state probability of any state i, in this case $i = 1$, is given by a normalized sum of all the weights of spanning trees rooted at vertex i (highlighted in pink).

Most terms in the sum will cancel. To rationalize this statement we observe that every tree is one of two types: T^{mn}, which contain edge e_{mn}, or S^{mn}, which does not. For all trees T^{mn} the only difference between rooted trees T_m and T_n is the directionality of the edge: T_m contains directed edge $n \to m$, and T_n contains directed edge $m \to n$. Then adding directed edge $m \to n$ to T_m and $n \to m$ to T_n results in the same graph, which will cancel in the summation, see Fig. 2.3(a). Adding edge e_{mn} to any tree S^{mn} will create a cycle going through states m and n. In specific, when adding $m \to n$ ($n \to m$) to S_n^{mn} (S_m^{mn}) the cycle will be oriented from m to n (from n to m), see Fig. 2.3(b). We then define a spanning cycle graph, C^{mn}, as a graph formed by a single cycle, oriented along the edge $n \to m$, with every other vertex linked by a unique path oriented towards the cycle. When the cycle is oriented in the opposite direction we write $\tilde{C}^{mn} = C^{nm}$. The set of all cycle graphs is denoted $\mathcal{C}^{mn}$ and the sum of the weights of all elements in this set is $w(\mathcal{C})$. Then the steady-state current

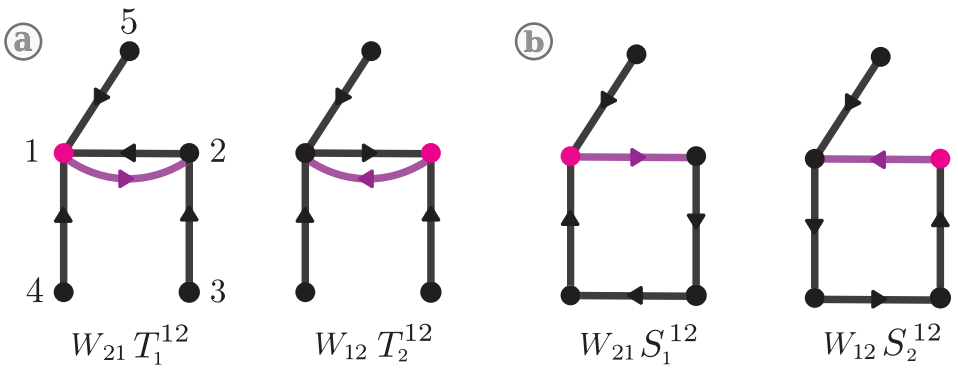


Figure 2.3: (a) For any tree T^{12} that contains e_{12}, adding directed edge $1 \to 2$ to the rooted tree T_1^{12} produces a subgraph with the same weight as that obtained by adding $2 \to 1$ to T_2^{12}. (b) For any rooted tree S_1^{12} that does not contain e_{12}, adding directed edge $1 \to 2$ creates a subgraph with a cycle in the clockwise direction. Adding $2 \to 1$ to S_2^{12} yields a subgraph that is identical except that the cycle is oriented in the counterclockwise direction.

is the difference of oriented cycle graphs

$$\bar{J}_{mn} = \frac{1}{\mathcal{N}} \sum_{C^{mn}} w(C^{mn}) - w(\tilde{C}^{mn}) = \frac{1}{\mathcal{N}} \Big[w(\mathcal{C}^{mn}) - w(\mathcal{C}^{nm}) \Big]. \tag{2.14}$$

This formulation also offers a deep connection with the cycle forces. Noting that the only difference between a cycle graph C^{mn} and its reverse $\tilde{C}^{mn}$ are the weights along the cycle, allows us to identify the cycle forces as

$$F(C^{mn}) = \ln \frac{w(C^{mn})}{w(\tilde{C}^{mn})}, \tag{2.15}$$

because all the edge weights not in the cycle cancel. Substituting into the steady-state current,

$$\bar{J}_{mn} = \frac{1}{\mathcal{N}} \sum_{C^{mn}} w(C^{mn}) \left(1 - e^{-F(C^{mn})}\right), \tag{2.16}$$

leads to the conclusion that nonzero currents require nonzero cycle forces, confirming our expectation that nonequilibrium flows require driving.

2.3 Nonequilibrium response

Typically, the experimentally accessible quantity is not the steady-state distribution, but steady-state averages of a state observable Q. At each state i the observable takes a value

Q_i, so that its average is

$$\langle Q \rangle = \sum_{i=1}^{N} Q_i \pi_i. \tag{2.17}$$

Our goal is to predict how perturbations of the transitions rates affect these averages. We model perturbations by allowing the rates to depend on an externally-controlled parameter λ. In particular, we study static responses, which measure how the steady-state value of an observable changes when a control parameter is perturbed infinitesimally and held fixed while the system relaxes to its new steady-state. A common, physically-motivated choice for this dependence is to exponentially re-weight the rates

$$W_{ij}(\lambda) = W_{ij} e^{\lambda d_{ij}} \tag{2.18}$$

through a coupling d_{ij} for $i \neq j$, which may have nonzero symmetric $d^s_{ij} = d_{ij} + d_{ji}$ and asymmetric $d^a_{ij} = d_{ij} - d_{ji}$ parts [45]. In which case, the static response to an external perturbation is defined by the linear combination of logarithmic derivatives

$$\frac{\partial \langle Q \rangle}{\partial \lambda} = \sum_{m \neq n} d_{mn} W_{mn} \frac{\partial \langle Q \rangle}{\partial W_{mn}} = \sum_{i, m \neq n} Q_i d_{mn} W_{mn} \frac{\partial \pi_i}{\partial W_{mn}}. \tag{2.19}$$

For perturbations around equilibrium steady-states π^{eq} where currents $\bar{J}^{\mathrm{eq}}_{mn}$ (Eq. (2.8)) are equal to zero, the FDT states [40]:

$$\frac{\partial \langle Q \rangle^{\mathrm{eq}}}{\partial \lambda} = \int_0^\infty \langle Q(t) J_{d^a}(0) \rangle^{\mathrm{eq}} dt, \tag{2.20}$$

where the equilibrium two-time correlation function between the observable and the d-weighted current is defined as

$$\langle Q(t) J_{d^a}(0) \rangle^{\mathrm{eq}} = \sum_{lij} Q_l (e^{tW})_{li} d^a_{ij} W_{ij} \pi_j \tag{2.21}$$

in terms of the transition probability $p(l, t|i, 0) = (e^{tW})_{li}$ for the system to be at l at time t given it was initially at i. Notably, only the asymmetric part of the coupling d^a_{ij} contributes. The symmetric part d^s_{ij} amounts to a coordinated and equal change in the forward and reverse rates between a pair of states. It is akin to varying a kinetic barrier, which cannot alter a system at equilibrium – the equilibrium Gibbs distribution only depends on the energies and not on the kinetics.

It is worth noting that generically adding an asymmetric coupling induces a nonconservative force, driving the system slightly away from equilibrium. The exception is when the

asymmetric coupling is derivable from a potential, $d^a_{ij} = -(U_i - U_j)$: in this case $J_d = -\dot{U}$, and the FDT (Eq. (2.20)) simplifies to a static equilibrium correlation,

$$\frac{\partial \langle Q \rangle^{\mathrm{eq}}}{\partial \lambda} = -\int_0^\infty \langle Q(t)\dot{U}(0)\rangle^{\mathrm{eq}} dt = \langle\!\langle Q, U \rangle\!\rangle^{\mathrm{eq}}, \tag{2.22}$$

where the covariance is $\langle\!\langle Q, U \rangle\!\rangle = \langle QU \rangle - \langle Q \rangle \langle U \rangle$. This perturbation is tantamount to varying the system's energy landscape by including a new potential U_i.

In light of this discussion, it is natural when studying nonequilibrium response to individually address changes in symmetric, asymmetric, or other particular combinations of rates. Previous works identified the following combinations of logarithmic derivatives as useful [21, 23]

$$\frac{\partial}{\partial E_i} = -\sum_{j \neq i} W_{ji} \frac{\partial}{\partial W_{ji}} \tag{2.23}$$

$$\frac{\partial}{\partial B_{mn}} = -W_{mn} \frac{\partial}{\partial W_{mn}} - W_{nm} \frac{\partial}{\partial W_{nm}} \tag{2.24}$$

$$\frac{\partial}{\partial F_{mn}} = \frac{1}{2}\left(W_{mn} \frac{\partial}{\partial W_{mn}} - W_{nm} \frac{\partial}{\partial W_{nm}} \right). \tag{2.25}$$

The E-perturbations, Eq. (2.23), which are uniform changes in the total exit rate from a state, are energy-like or equilibrium-like in that they satisfy a fluctuation-response equality akin to the equilibrium FDT Eq. (2.22), but valid arbitrarily far from equilibrium [21]

$$\sum_{i=1}^{N} U_i \frac{\partial \langle Q \rangle}{\partial E_i} = \langle\!\langle Q, U \rangle\!\rangle, \tag{2.26}$$

for arbitrary state function U_i. The symmetric B-perturbations Eq. (2.24) are like changes in kinetic barriers, and the asymmetric F-perturbations Eq. (2.25) are like shifts in the driving forces. Figure 2.4 illustrates these perturbations to help build intuition about their significance. Any arbitrary perturbation can be then be decomposed, albeit non-uniquely, into a linear combination of these three types of perturbations.

This decomposition of perturbations is analogous to parameterizing the transition rates as

$$W_{ij} = e^{-E_j - B_{ij} + F_{ij}/2}, \tag{2.27}$$

with $B_{ij} = B_{ji}$ and $F_{ij} = -F_{ji}$. This parametrization is reminiscent of the Arrhenius expression for transition rates for a system evolving in an energy landscape with wells of depth E_i and barriers of height B_{ij} driven by forces F_{ij}. The correspondence becomes clear by considering an arbitrary function of all transition rates, $\Phi(W_{ji}, \dots)$, with $j \neq i$, since the diagonal

elements are set by probability conservation. Applying the chain rule, the response of Φ to changes in E_i is

$$\frac{\partial \Phi}{\partial E_i} = \sum_k \sum_{j \neq k} \frac{\partial W_{jk}}{\partial E_i} \frac{\partial \Phi}{\partial W_{jk}} = -\sum_{j \neq i} W_{ji} \frac{\partial \Phi}{\partial W_{ji}}, \tag{2.28}$$

because the parametrization in Eq. (2.27) ensures that only the rates W_{ji} depend on E_i. A similar argument shows that responses to changes in B_{ij} and F_{ji} take the same form as the symmetric (Eq. (2.24)) and asymmetric (Eq. (2.25)) decompositions.

For the symmetric and asymmetric perturbations, Owen et al. previously demonstrated constraints on ratios of nonnegative observables, $Q^{(1)}, Q^{(2)} \geq 0$ [21]:

$$\left| \frac{\partial \ln(\langle Q^{(1)} \rangle / \langle Q^{(2)} \rangle)}{\partial B_{mn}} \right| \leq \tanh(\mathcal{F}_{\max}/4) \tag{2.29}$$

$$\left| \frac{\partial \ln(\langle Q^{(1)} \rangle / \langle Q^{(2)} \rangle)}{\partial F_{mn}} \right| \leq 1, \tag{2.30}$$

where $\mathcal{F}_{\max} = \max_{C \ni e_{mn}} F_C$ is the maximum cycle force through the perturbed edge.

Our focus here is the response of a single observable $\langle Q \rangle$ (Eq. (2.19)), not a ratio. To transform the predictions in Eq. (2.29) and Eq. (2.30) into bounds on a single observable, let us introduce notation for the observable's maximum Q_M and minimum Q_m. Then, by setting the two positive observables in Eq. (2.29) and Eq. (2.30) to be $Q^{(1)} = Q - Q_m \geq 0$ and $Q^{(2)} = Q_M - Q \geq 0$, we arrive at the relevant predictions

$$\left| \frac{\partial \langle Q \rangle}{\partial B_{mn}} \right| \leq \frac{(Q_M - \langle Q \rangle)(\langle Q \rangle - Q_m)}{Q_M - Q_m} \tanh(\mathcal{F}_{\max}/4) \tag{2.31}$$

$$\left| \frac{\partial \langle Q \rangle}{\partial F_{mn}} \right| \leq \frac{(Q_M - \langle Q \rangle)(\langle Q \rangle - Q_m)}{Q_M - Q_m}. \tag{2.32}$$

These predictions do not account for any specific properties of the graph's topology. The goal of this work is then to derive tighter inequalities that reveal how the topology of the state-space graph G limits nonequilibrium response.

2.4 Bounds on the nonequilibrium response of state observables

In the following, we derive Fluctuation-Response Inequalities for single- and multiple-edge symmetric perturbations, as well as for single-edge asymmetric and arbitrary perturbations. A first step shared by all derivations is recognizing that the steady-state response admits a

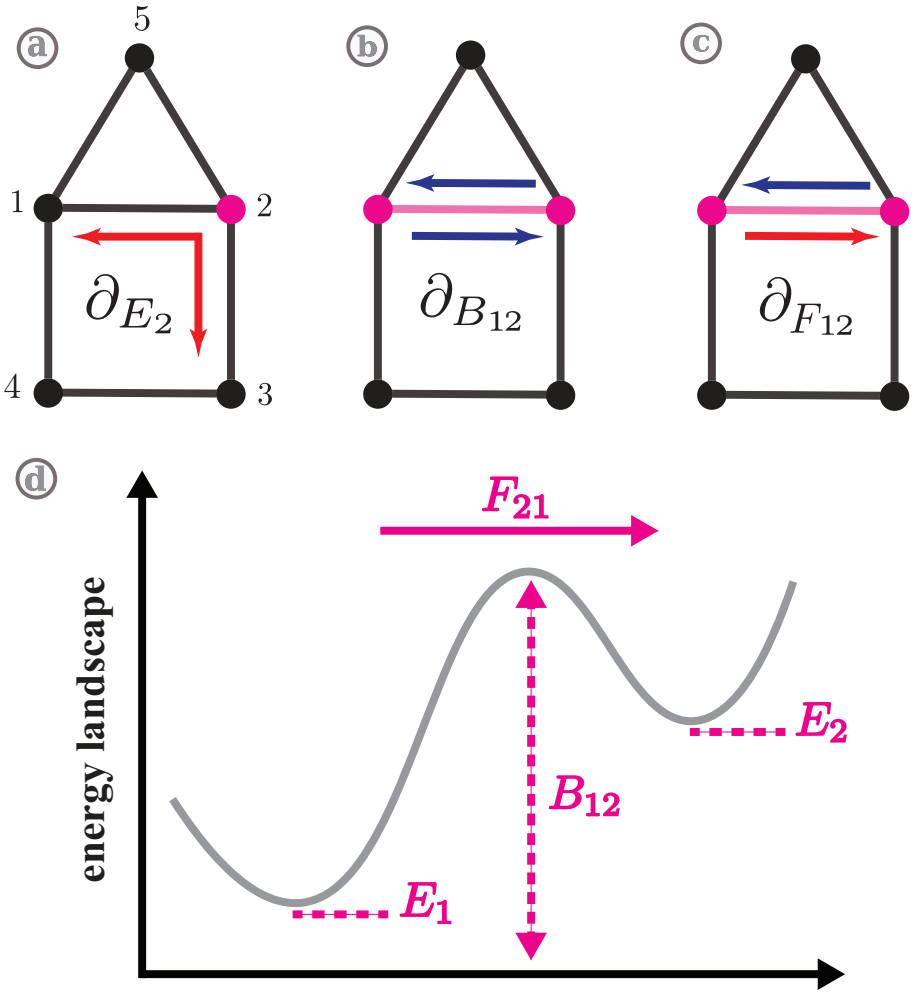


Figure 2.4: An arbitrary nonequilibrium response can be expressed as a linear combination of three distinct components. (a) E-perturbations (also called equilibrium-like perturbations), (b) symmetric B-perturbations (also called kinetic perturbations), and (c) asymmetric F-perturbations. (a) An E-perturbation of state n corresponds to a uniform decrease in all exit rates from that state. (b) A symmetric perturbation between states m and n corresponds to a uniform increase in both the forward and backward transition rates between the two states. (c) An asymmetric perturbation between states m and n corresponds to an increase in the forward rate and an equal decrease of the backward transition rate between the two states. (d) Assuming the system admits a well-defined energy landscape, it is possible to develop an intuitive understanding for each type of perturbation. E-perturbations are equivalent to changes in the energy of a state. Symmetric perturbations correspond to changes in the energetic barrier between states. Asymmetric perturbations correspond to shifts in the driving forces.

graphical solution. The task of finding the maximum response can then be formulated as a linear optimization problem. Some details of the derivations are occasionally omitted and discussed further in Section 2.9 to maintain the flow of the main text.

2.4.1 Single-edge symmetric perturbation

We begin our analysis by determining the maximum response of the steady-state average of an observable Q to a symmetric perturbation (Eq. (2.24)) along a single edge e_{mn},

$$\frac{\partial \langle Q \rangle}{\partial B_{mn}} = \sum_{i=1}^{N} Q_i \frac{\partial \pi_i}{\partial B_{mn}}. \tag{2.33}$$

By directly differentiating the master equation Eq. (2.7) we obtain

$$\sum_{j=1}^{N} W_{ij} \frac{\partial \pi_j}{\partial B_{mn}} = -\sum_{j=1}^{N} \frac{\partial W_{ij}}{\partial B_{mn}} \pi_j. \tag{2.34}$$

Recalling the rates must satisfy probability conservation, we recognize that

$$\frac{\partial W_{ij}}{\partial B_{mn}} = -W_{mn}\delta_{im}\delta_{jn} - W_{nm}\delta_{in}\delta_{jm} \qquad i \neq j \tag{2.35}$$

$$\frac{\partial W_{ii}}{\partial B_{mn}} = -\sum_{j \neq i} \frac{\partial W_{ji}}{\partial B_{mn}} = W_{mn}\delta_{jm}\delta_{in} + W_{nm}\delta_{jn}\delta_{im} \qquad i = j. \tag{2.36}$$

So that the symmetric response of the steady-state probabilities is the solution to the set of inhomogeneous linear equations

$$\sum_{j=1}^{N} W_{ij} \frac{\partial \pi_j}{\partial B_{mn}} = \bar{J}_{mn} \left(\delta_{im} - \delta_{in} \right), \tag{2.37}$$

with $\bar{J}_{mn}$ the current through the perturbed edge (Eq. (2.8)).

Analogous to its homogeneous counterpart, whose solution is given by the MTT, Eq. (2.37) can also be solved using graph-theoretical methods. The solutions are now built out of spanning 2-forests: subgraphs of the state-space G composed of 2 disjoint individually-connected components with no cycles such that each vertex is in exactly one component. In each component, we can choose a vertex, r_1 and r_2, called the roots, and orient all edges in each component along the unique path towards that root. The resultant subgraph, we call a rooted spanning 2-forest and will denote it as $f_{r_1} \sqcup f_{r_2}$. To each rooted 2-forest we assign a weight as the product of the weights of all its edges, $w(f_{r_1} \sqcup f_{r_2})$. We depict the spanning 2-forests for the house graph in Fig. 2.5(a).

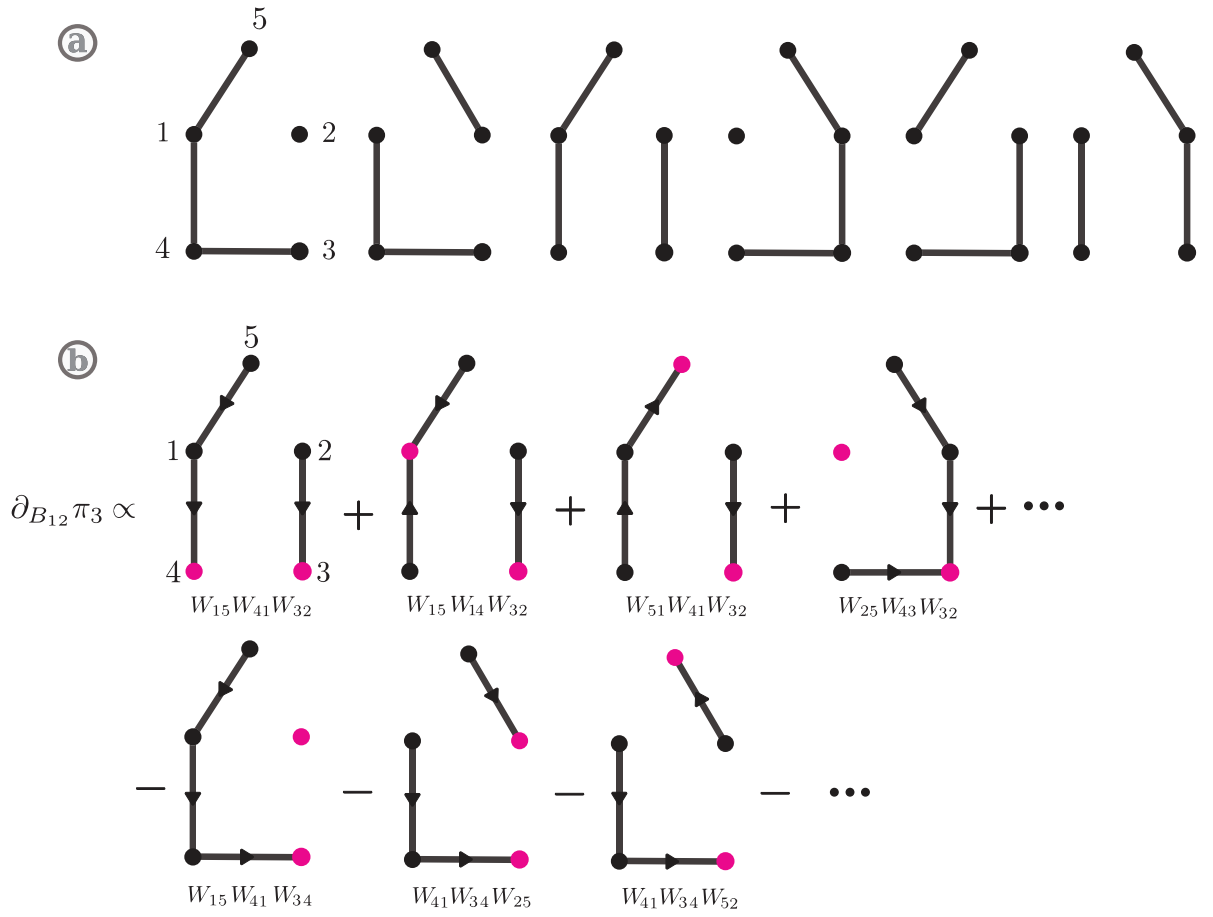


Figure 2.5: Graphical representation of the solution to Eq. 2.37. (a) All 2-forests for the house graph (Fig. 2.1). (b) For a symmetric edge perturbation on edge e_{12}, the response of π_3, is composed of two terms, a positive one, which is a sum of weights of all rooted 2-forests $f_l^1 \sqcup f_3^2$ (both roots are highlighted in pink), and a negative one, which is a sum of weights on all rooted 2-forests $f_3^1 \sqcup f_l^2$.

Specifically, the solution depends on 2-forests $f^m \sqcup f^n$, where component f^m has vertex m and component f^n has vertex n,

$$\frac{\partial \pi_i}{\partial B_{mn}} = \frac{\bar{J}_{mn}}{\mathcal{N}} \sum_{\mathcal{F}^{mn},j} w\left(f_j^m \sqcup f_i^n\right) - w\left(f_i^m \sqcup f_j^n\right), \tag{2.38}$$

with $\mathcal{F}^{mn}$ the set of all 2-forests $f^m \sqcup f^n$. This graphical solution is illustrated in Fig. 2.5(b) and its detailed derivation is discussed in Section 2.9.1. Inserting this solution Eq. (2.38) in

Eq. (2.33) we find

$$\frac{\partial\langle Q\rangle}{\partial B_{mn}} = \frac{\bar{J}_{mn}}{\mathcal{N}} \sum_{\mathcal{F}^{mn},i,j} Q_i \left[w\left(f_j^m \sqcup f_i^n\right) - w\left(f_i^m \sqcup f_j^n\right)\right]. \tag{2.39}$$

To simplify this expression we start by multiplying and dividing by $\pi_i\pi_j$. Making use of the MTT solution for the steady-states (Eq. (2.12)) we have

$$\frac{\partial\langle Q\rangle}{\partial B_{mn}} = \bar{J}_{mn}\mathcal{N} \sum_{\mathcal{F}^{mn},i,j} Q_i\pi_i\pi_j \frac{w\left(f_j^m \sqcup f_i^n\right) - w\left(f_i^m \sqcup f_j^n\right)}{\sum_{\mathcal{T}} w(T_i) \sum_{\mathcal{T}} w(T_j)} \tag{2.40}$$

$$= \bar{J}_{mn}\mathcal{N} \sum_{i,j} (Q_j - Q_i)\pi_i\pi_j \frac{\sum_{\mathcal{F}^{mn}} w\left(f_i^m \sqcup f_j^n\right)}{\sum_{\mathcal{T}} w(T_i) \sum_{\mathcal{T}} w(T_j)}. \tag{2.41}$$

Now recalling the graph theoretical representation of currents (Eq. (2.14)) and multiplying and dividing by $\left(\sqrt{w(\mathcal{C}^{mn})} + \sqrt{w(\mathcal{C}^{nm})}\right)^2$ we find:

$$\left|\frac{\partial\langle Q\rangle}{\partial B_{mn}}\right| = \mathcal{M}\left|\sum_{i,j} (Q_j - Q_i)\, \pi_i\pi_j\mathcal{P}_{ij}\right|, \tag{2.42}$$

where we have separated out an overall magnitude

$$\mathcal{M} = \frac{|w(\mathcal{C}^{mn}) - w(\mathcal{C}^{nm})|}{\left(\sqrt{w(\mathcal{C}^{mn})} + \sqrt{w(\mathcal{C}^{nm})}\right)^2}, \tag{2.43}$$

and a collection of structural coefficients

$$\mathcal{P}_{ij} = \left(\sqrt{w(\mathcal{C}^{mn})} + \sqrt{w(\mathcal{C}^{nm})}\right)^2 P_{ij}, \qquad \text{where} \qquad P_{ij} = \frac{\sum_{\mathcal{F}^{mn}} w(f_i^m \sqcup f_j^n)}{\sum_{\mathcal{T}} w(T_i) \sum_{\mathcal{T}} w(T_j)} \tag{2.44}$$

are forest-tree ratios. Equation (2.42) allows us to split the problem in two parts. First we tackle the response magnitude $\mathcal{M}$. Factoring the numerator of the response magnitude Eq. (2.43), we find

$$\mathcal{M} = \left|\frac{\sqrt{w(\mathcal{C}^{mn})} - \sqrt{w(\mathcal{C}^{nm})}}{\sqrt{w(\mathcal{C}^{mn})} + \sqrt{w(\mathcal{C}^{nm})}}\right| = \tanh\left(\frac{1}{4}\left|\ln\frac{w(\mathcal{C}^{mn})}{w(\mathcal{C}^{nm})}\right|\right). \tag{2.45}$$

Then an application of the log-sum inequality [46] to the sums over cycle graphs and the

definition of cycle force Eq. (2.15), leads to the sequence of bounds

$$\mathcal{M} \leq \tanh\left(\frac{1}{4\,w(\mathcal{C}^{mn})}\sum_{C^{mn}} w(C^{mn})\,|F(C^{mn})|\right) \tag{2.46}$$

$$\leq \tanh(\mathcal{F}_{\max}/4), \tag{2.47}$$

where $\mathcal{F}_{\max} = \max_{C^{mn}} |F(C^{mn})|$ is the maximum over all cycle forces through the perturbed edge.

Second, we address the structural coefficients Eq. (2.44), which are formed from spanning forests and therefore are not independent. First, we note that due to their definition, the forest-tree ratios are nonnegative, $P_{ij} \geq 0$. A number of them are also trivially zero,

$$P_{im} = 0 \quad i \neq m, \tag{2.48}$$

$$P_{ni} = 0 \quad i \neq n, \tag{2.49}$$

$$P_{ii} = 0, \tag{2.50}$$

since a vertex can only be in one component, and the 2-forests $f_j^m \sqcup f_m^n$ and $f_n^m \sqcup f_i^n$ with m or n in the opposite component are not possible. In Section 2.9.2 we derive in detail that the forest-tree ratios are further related by

$$P_{ij} \leq P_{mj}, P_{in} \tag{2.51}$$

$$P_{mi} + P_{ij} = P_{mj} + P_{ji} \tag{2.52}$$

$$P_{in} + P_{ji} = P_{jn} + P_{ij} \tag{2.53}$$

which naturally extend to the structural coefficients $\mathcal{P}_{ij}$. Furthermore, the structural coefficient

$$\mathcal{P}_{mn} \leq 1 \tag{2.54}$$

is bounded, which also constrains all other structural coefficients $\mathcal{P}_{ij} \leq 1$ Eq. (2.51). The linear relationships between the structural coefficients implied by Eqs. (2.51) to (2.54) confine the $\mathcal{P}_{ij}$ to a convex polytope, called the feasible polytope. For the three-state triangle graph we can visualize this polytope, see Fig. 2.6.

Limits to the response can then be deduced by identifying the values of the $\mathcal{P}_{ij}$ inside this polytope that maximize the response. Namely, we can collect the constraints in Eqs. (2.51)

to (2.54) to frame our question as the linear optimization problem:

$$\max_{\mathcal{P}_{ij}} \left| \sum_{i,j} (Q_j - Q_i)\, \pi_i \pi_j \mathcal{P}_{ij} \right| \quad \text{such that for all } i \neq j \neq m, n \tag{2.55}$$

$$0 \leq \mathcal{P}_{ij} \leq \mathcal{P}_{mj} \leq \mathcal{P}_{mn} \leq 1 \tag{2.56}$$

$$0 \leq \mathcal{P}_{ij} \leq \mathcal{P}_{in} \leq \mathcal{P}_{mn} \leq 1 \tag{2.57}$$

$$\mathcal{P}_{mn} = \mathcal{P}_{mi} + \mathcal{P}_{in} \tag{2.58}$$

$$\mathcal{P}_{mi} + \mathcal{P}_{ij} = \mathcal{P}_{mj} + \mathcal{P}_{ji} \tag{2.59}$$

$$\mathcal{P}_{in} + \mathcal{P}_{ji} = \mathcal{P}_{jn} + \mathcal{P}_{ij}. \tag{2.60}$$

The fundamental theorem of linear programming then states that the solution to this optimization problem will be one of the vertices of the feasible polytope [47].

In Section 2.9.3 we argue that the vertices of the feasible polytope are inherited from the 2-forests. The potential optima are the topologically-consistent splitting of the vertices of the graph, $V^{mn} \in \mathcal{V}^{mn}$: each V^{mn} is formed by cutting the graph into two connected disjoint components, one V^m which contains the vertex m and the other V^n which contains vertex n. This splitting is illustrated in Fig. 2.7 for the house graph.

We can now calculate the value of our objective function at these potential optima. Recognizing that $\sum_{j \in V^m} \pi_j + \sum_{j \in V^n} \pi_j = 1$, as any 2-forest contains all vertices of the state-space G, we have

$$\begin{aligned}
\sum_{i,j} (Q_j - Q_i)\, \pi_i \pi_j \mathcal{P}_{ij} \Big|_{\text{vertex}} &= \sum_{i \in V^m} \sum_{j \in V^n} (Q_j - Q_i)\, \pi_i \pi_j \\
&= \sum_{j \in V^n} Q_j \pi_j \sum_{i \in V^m} \pi_i - \left(\langle Q \rangle - \sum_{j \in V^n} Q_j \pi_j \right) \sum_{j \in V^n} \pi_j \\
&= \sum_{j \in V^n} Q_j \pi_j - \langle Q \rangle \sum_{j \in V^n} \pi_j \\
&= \langle\!\langle Q, \delta(V^n) \rangle\!\rangle = -\langle\!\langle Q, \delta(V^m) \rangle\!\rangle,
\end{aligned} \tag{2.61}$$

with $\delta_i(V)$ the characteristic function of a vertex set V, taking value one when $i \in V$ and zero otherwise. Any one of the vertices could be the maximum, the particular one depends on the observable and the steady-state distribution:

$$\max_{\mathcal{P}_{ij}} \left| \sum_{i,j} (Q_j - Q_i)\, \pi_i \pi_j \mathcal{P}_{ij} \right| \leq \max_{\mathcal{V}^{mn}} \left| \langle\!\langle Q, \delta(V^m) \rangle\!\rangle \right|. \tag{2.62}$$

At last we combine the bounds defined by Eq. (2.47) and Eq. (2.62), to obtain the result

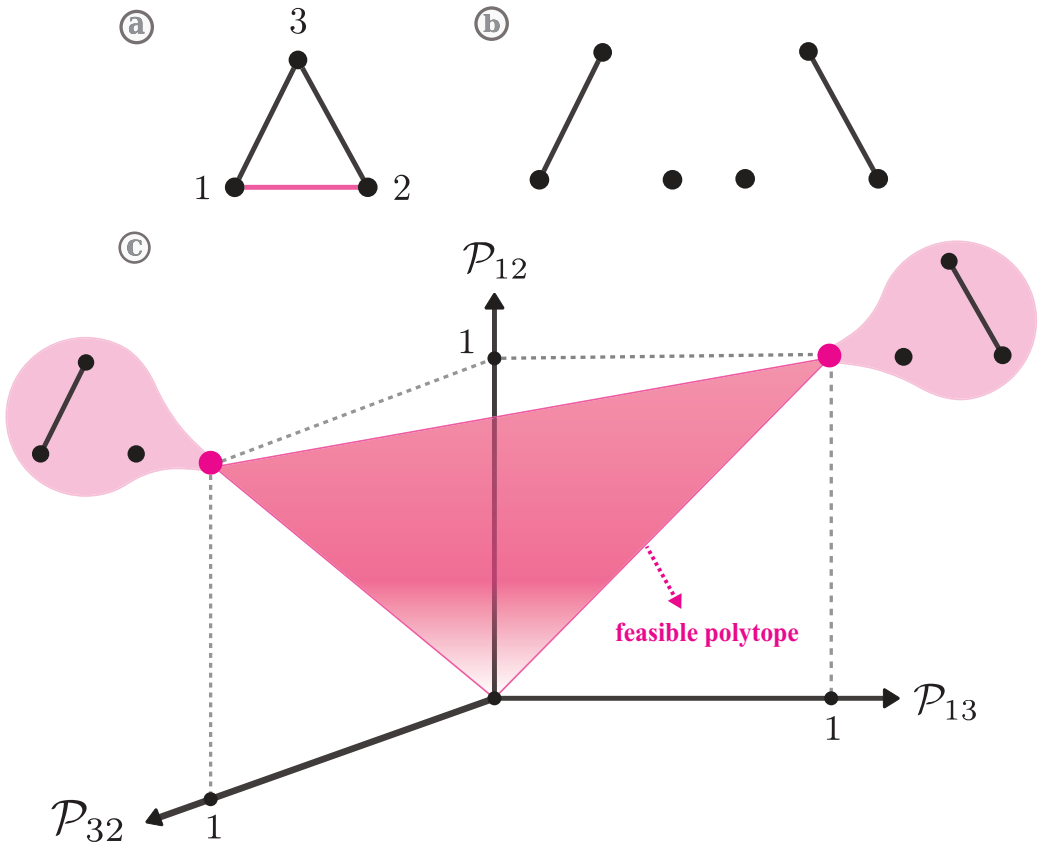


Figure 2.6: (a) Triangle graph with perturbed edge $\bar{e}_{12}$ (highlighted in pink). (b) 2-forests $\mathcal{F}^{12}$. (c) Feasible polytope: The only structural coefficients that are not trivially zero are P_{12}, P_{13} and P_{32}. As there is only one linearly independent equality constraint, $P_{12} = P_{13} + P_{32}$, the feasible polytope has dimension $d = 2$. Its vertices are the trivial case $(0, 0, 0)$, as well as $(1, 1, 0)$ and $(1, 0, 1)$ that are each associated to a 2-forest.

that topology and thermodynamics constrain the response of $\langle Q \rangle$ via a Fluctuation-Response Inequality

$$\left| \frac{\partial \langle Q \rangle}{\partial B_{mn}} \right| \leq \max_{\mathcal{V}^{mn}} \left| \langle\!\langle Q, \delta(V^m) \rangle\!\rangle \right| \tanh\left(\mathcal{F}_{\max}/4\right), \tag{2.63}$$

where we recall that $\mathcal{F}_{\max}$ is the maximum cycle force going through the perturbed edge e_{mn}, and $V^{mn} \in \mathcal{V}^{mn}$ is the topologically-consistent splitting of the vertices of the graph.

Equation (2.63) has the character of the FDT, linking response to fluctuations. Here, however, the covariance measures the fluctuations of the observable across the two components of V^{mn}, a topologically-dependent noise characteristic. The response is zero whenever all the cycle forces through the perturbed edge are zero, $\mathcal{F}_{\max} = 0$. This is possible away from equilibrium, but is always true at equilibrium. It also can occur if there are no cycles through the perturbed edge because it is a bridge, its removal disconnects G into

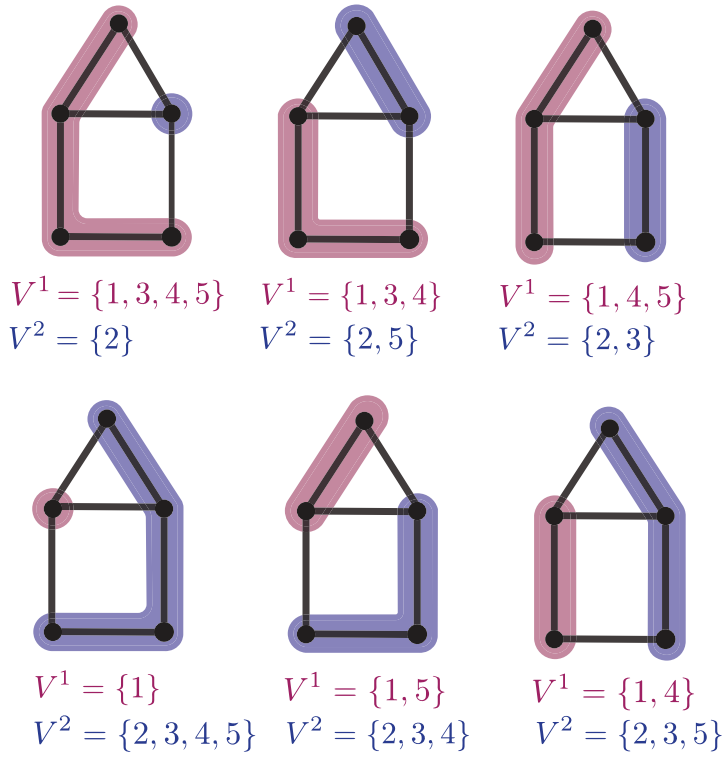


Figure 2.7: Representation of the topologically-consistent splitting of the vertices, $\mathcal{V}^{12}$, for the house graph (Fig. 2.1). The set V^1, highlighted in pink, contains vertex 1, and V^2, highlighted in blue, contains vertex 2.

two disjoint components. In Fig. 2.8, we verify Eq. (2.63) by plotting the response ratio $\mathcal{R}_B = |\partial_{B_{mn}}\langle Q\rangle| / \max_{\mathcal{V}^{mn}} |\langle\!\langle Q, \delta(V^m)\rangle\!\rangle|$ for perturbations along e_{12} of the house graph (Fig. 2.1) for random observables and rates.

2.4.2 Multiple-edge symmetric perturbation

When multiple edges are perturbed in the graph, we expect the response to have a more complicated dependence on the topology. However, there is one situation where our analysis directly generalizes to multi-edge perturbations. That is when their combined impact is effectively like a single edge perturbation. Our assumption is that these edges with their incident nodes form a subgraph H^{mn} of G that only connects to the rest of the graph at two vertices, which we call m and n, as illustrated in Fig. 2.9. Note that m and n may not be directly linked by any single edge, but there is at least one path between m and n through H^{mn}. All the edges not in H^{mn} and incident to either m or n form a cut-set of G, which we label as K^{mn}, such that removing all of them splits G into two separate connected components.

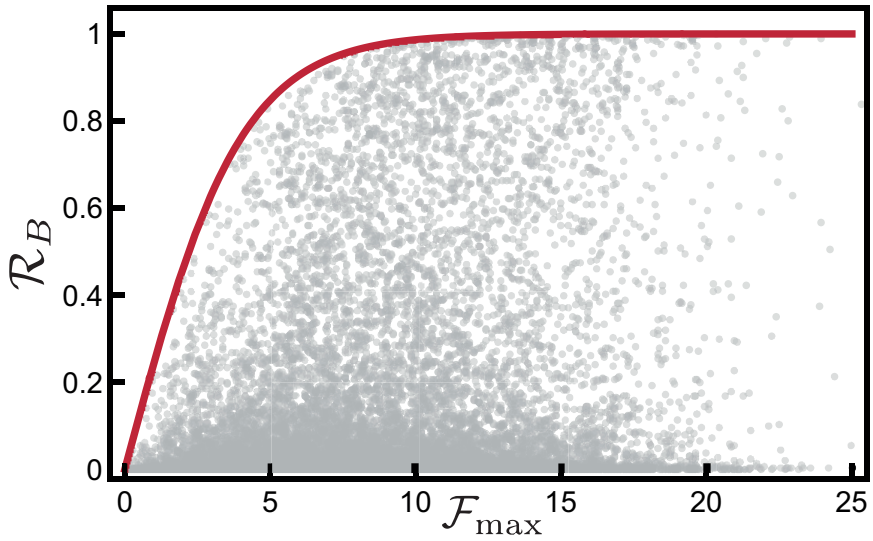


Figure 2.8: Response ratio $\mathcal{R}_B$ as a function of the maximum cycle force $\mathcal{F}_{\max}$ around cycles containing edge e_{12} of the house graph (Fig. 2.1) for 15000 rate matrices with the logarithmic asymmetric $\ln(W_{ij}/W_{ji})$ and symmetric $\ln(W_{ij}W_{ji})$ parts sampled uniformly on $[-7, 7]$ and the observable Q_i sampled uniformly on $[-4, 4]$. All samples (gray) fall below the predicted bound $\tanh(\mathcal{F}_{\max}/4)$ (red).

To bound the response of an observable to a coordinated and uniform symmetric perturbation of all edges in H^{mn}, we follow closely our derivation for a single edge and consider the derivative

$$\sum_{\bar{e}_{lk}\in H^{mn}} \frac{\partial\langle Q\rangle}{\partial B_{lk}} = \sum_{j=1}^{N} Q_j \sum_{\bar{e}_{lk}\in H^{mn}} \frac{\partial\pi_j}{\partial B_{lk}}, \tag{2.64}$$

with the steady-state responses solving the set of inhomogenous linear equations

$$\sum_{j=1}^{N} W_{ij}\left(\sum_{\bar{e}_{lk}\in H^{mn}} \frac{\partial\pi_j}{\partial B_{lk}}\right) = \sum_{\bar{e}_{lk}\in H^{mn}} \bar{J}_{lk}\left(\delta_{il}-\delta_{ik}\right). \tag{2.65}$$

At this point, we recall that conservation of probability requires that the total probability current flowing into or out of any vertex is zero, $\sum_i \bar{J}_{ij} = \sum_j \bar{J}_{ij} = 0$. Therefore the sums in Eq. (2.65) at vertices internal to H^{mn} cancel. Only at m and n does the sum on probability currents leave an imbalance equal to the total probability flowing in or out of the subgraph H^{mn},

$$\sum_{j=1}^{N} W_{ij}\left(\sum_{e_{lk}\in H^{mn}} \frac{\partial\pi_j}{\partial B_{lk}}\right) = \bar{J}^H(\delta_{im}-\delta_{in}), \tag{2.66}$$

with total probability flow out of H^{mn}, which is the same as into due to probability conservation, given by the sum of the currents on all edges in the cut-set oriented away from

m

$$\bar{J}^H = \sum_{e_{im} \in K^{mn}} \bar{J}_{im} = \frac{1}{\mathcal{N}} \left[w\left(\mathcal{C}^H\right) - w\left(\tilde{\mathcal{C}}^H\right) \right]. \tag{2.67}$$

Here, we have further observed that this probability current is only due to cycle-graphs in $\mathcal{C}^H$ whose cycles straddle H^{mn} and its complement, oriented such that they exit at m and enter at n, as illustrated in Fig. 2.9. The solution of Eq. (2.66) can be organized using 2-forests,

$$\sum_{\bar{e}_{lk} \in H^{mn}} \frac{\partial \pi_j}{\partial B_{lk}} = \frac{\bar{J}^H}{\mathcal{N}} \sum_{\mathcal{F}^{mn},j} w\left(f_j^m \sqcup f_i^n\right) - w\left(f_i^m \sqcup f_j^n\right). \tag{2.68}$$

Substitution into Eq. (2.64) and rearranging as before, leads to

$$\left| \sum_{\bar{e}_{lk} \in H^{mn}} \frac{\partial \langle Q \rangle}{\partial B_{lk}} \right| = \mathcal{M}^H \left| \sum_{i,j} \left(Q_j - Q_i\right) \pi_i \pi_j \mathcal{P}_{ij}^H \right|, \tag{2.69}$$

with overall magnitude

$$\mathcal{M}^H = \frac{\left| w(\mathcal{C}^H) - w(\tilde{\mathcal{C}}^H) \right|}{\left(\sqrt{w(\mathcal{C}^H)} + \sqrt{w(\tilde{\mathcal{C}}^H)} \right)^2}, \tag{2.70}$$

and structural coefficients

$$\mathcal{P}_{ij}^H = \left(\sqrt{w(\mathcal{C}^H)} + \sqrt{w(\tilde{\mathcal{C}}^H)} \right)^2 P_{ij}, \quad \text{where} \quad P_{ij} = \frac{\sum_{\mathcal{F}^{mn}} w(f_i^m \sqcup f_j^n)}{\sum_{\mathcal{T}} w(T_i) \sum_{\mathcal{T}} w(T_j)}. \tag{2.71}$$

The bound on $\mathcal{M}^H$ follows the exact same line of reasoning we used to bound $\mathcal{M}$ for a single edge response. The result is then

$$\mathcal{M}^H \leq \tanh(\mathcal{F}_{\max}/4), \tag{2.72}$$

except here $\mathcal{F}_{\max} = \max_{C \in \mathcal{C}^H} |F(C)|$ as it emerges from ratios of elements of $\mathcal{C}^H$ and $\tilde{\mathcal{C}}^H$.

Next, we observe that the structural coefficients $\mathcal{P}_{ij}^H$ are defined in terms of the same type of forest-tree ratios that appeared in our analysis of a single edge perturbation. Furthermore, the linear relationships between the forest-tree ratios in Eqs. (2.51) to (2.53) did not depend on the vertices being linked by an edge, and thus hold here as well. The only potential difference from our single-edge analysis is the bound $\mathcal{P}_{mn}^H \leq 1$ (Eq. (2.54)), but this holds as well as derived in Section 2.9.4. This then implies that the response can be bounded as

$$\left| \sum_{e_{kl} \in H^{mn}} \frac{\partial \langle Q \rangle}{\partial B_{kl}} \right| \leq \max_{\mathcal{V}^{mn}} \left| \langle\!\langle Q, \delta(V^m) \rangle\!\rangle \right| \tanh\left(\mathcal{F}_{\max}/4\right), \tag{2.73}$$

where $\mathcal{F}_{\max}$ is the maximum cycle force over all cycles that straddle the perturbed and

unperturbed regions passing through the two vertices m and n.

2.4.3 Asymmetric and arbitrary perturbations

In this section, we extend the methods used to bound symmetric edge responses to also obtain bounds for asymmetric and more general perturbations. Nonsymmetric edge perturbations can generate a response even in equilibrium Eq. (2.20). Thus, we expect thermodynamics to

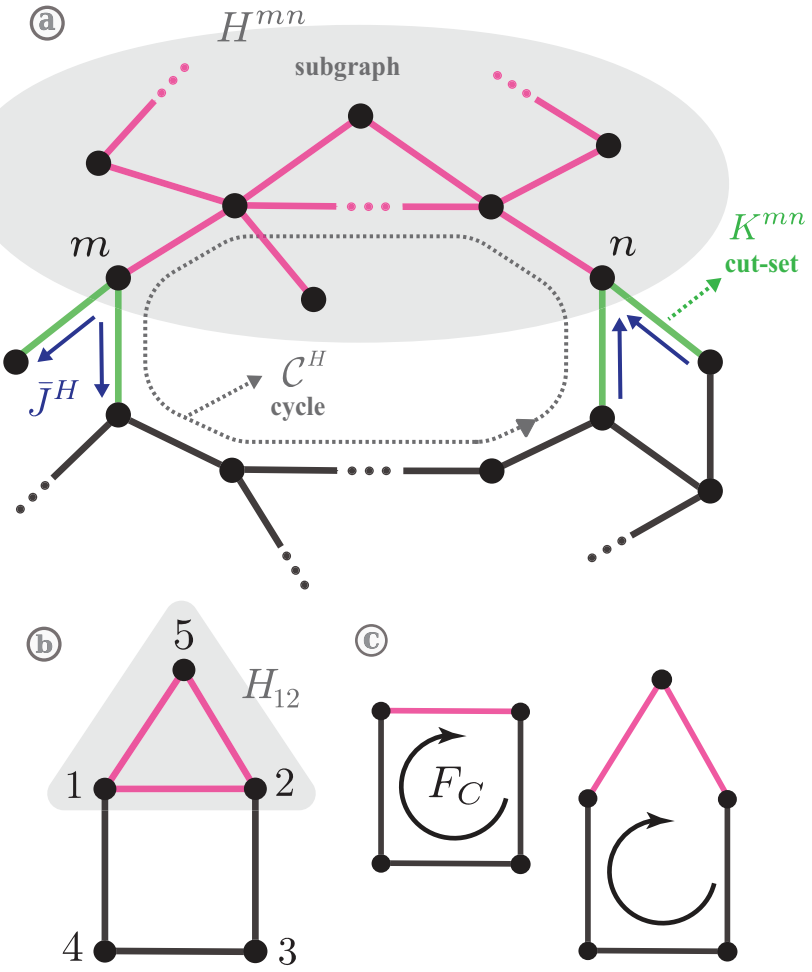


Figure 2.9: (a) Multi-edge perturbation in a generic graph: all edges (pink) in the subgraph H^{mn} (gray) are perturbed uniformly. Removing all edges of the cut-set K^{mn} (green) splits the graph into two separate subgraphs. The probability current $\bar{J}^H$ (blue arrows) flowing in and out of H^{mn} is due to cycles $\mathcal{C}^H$ that straddle the perturbed and unperturbed regions. (b) Representation of a multi-edge perturbation for the illustrative graph. All edges in the subgraph H^{12}, highlighted in gray, are uniformly perturbed. (c) Cycles that count towards determining $\mathcal{F}_{\max}$ in the case of multi-edge perturbation of H^{12}. Note that the cycle $\{1 \to 2 \to 5 \to 1\}$ is not relevant in this case, as it is internal to H^{12}.

not be a limiting constraint, and focus solely on the influence of network topology. We first will analyze a general rate perturbation, and then specialize to asymmetric perturbations Eq. (2.25).

The response of an observable to the logarithmic perturbation of a single kinetic rate W_{mn} is

$$\frac{\partial \langle Q \rangle}{\partial \ln W_{mn}} = \sum_{j=1}^{N} Q_j \frac{\partial \pi_j}{\partial \ln W_{mn}}. \tag{2.74}$$

Here, the master equation implies the responses of the steady-state distribution satisfy

$$\sum_{j=1}^{N} W_{ij} \frac{\partial \pi_j}{\partial \ln W_{mn}} = W_{mn} \pi_n (\delta_{in} - \delta_{im}). \tag{2.75}$$

Analogously to the single edge perturbation, the solution is given in terms of 2-forests as

$$\frac{\partial \pi_i}{\partial \ln W_{mn}} = \frac{W_{mn} \pi_n}{\mathcal{N}} \sum_{\mathcal{F}^{mn},j} w\left(f_i^m \sqcup f_j^n\right) - w\left(f_j^m \sqcup f_i^n\right), \tag{2.76}$$

Substituting into Eq. (2.74) and reorganizing, we recover the structure,

$$\left| \frac{\partial \langle Q \rangle}{\partial \ln W_{mn}} \right| = \left| \sum_{i,j} (Q_j - Q_i)\, \pi_i \pi_j \mathcal{P}_{ij}^W \right|, \tag{2.77}$$

where in this case the structural coefficients are

$$\mathcal{P}_{ij}^W = W_{mn} \sum_{\mathcal{T}} w(T_n) P_{ij}, \qquad \text{with} \qquad P_{ij} = \frac{\sum_{\mathcal{F}^{mn}} w(f_i^m \sqcup f_j^n)}{\sum_{\mathcal{T}} w(T_i) \sum_{\mathcal{T}} w(T_j)}. \tag{2.78}$$

We again conclude that the structural coefficients retain the linear relationships presented in Eqs. (2.51) to (2.54) necessary to bound this sum. The only potential change is the overall magnitude, requiring us to demonstrate that $\mathcal{P}_{mn}^W \leq 1$ as in Eq. (2.54). From the definition of the structural coefficients, we have

$$\mathcal{P}_{mn}^W = W_{mn} \sum_{\mathcal{T}} w(T_n) \frac{\sum_{\mathcal{F}^{mn}} w(f_m^m \sqcup f_n^n)}{\sum_{\mathcal{T}} w(T_m) \sum_{\mathcal{T}} w(T_n)} = \frac{\sum_{\mathcal{F}^{mn}} W_{mn} w(f_m^m \sqcup f_n^n)}{\sum_{\mathcal{T}} w(T_m)}. \tag{2.79}$$

Recognizing that addition of the edge e_{mn} to a 2-forest $f_m^m \sqcup f_n^n$ results in a tree $T_m^{n \to m}$ rooted at m with the edge directed from $n \to m$, so that $W_{mn} w(f_m^m \sqcup f_n^n) = w(T_m^{n \to m})$, we have,

$$\mathcal{P}_{mn}^W = \frac{\sum_{\mathcal{T}} w(T_m^{n \to m})}{\sum_{\mathcal{T}} w(T_m)} \leq 1, \tag{2.80}$$

where the inequality follows because the set of all trees includes more trees then just those

that contain the edge e_{mn}. Therefore we recover the same topological bound

$$\left|\frac{\partial\langle Q\rangle}{\partial \ln W_{mn}}\right| \leq \max_{\mathcal{V}^{mn}} \left|\langle\!\langle Q, \delta(V^m)\rangle\!\rangle\right|. \tag{2.81}$$

We see the correlation between the observable and the topologically-consistent splittings provide the ultimate limit, no matter how strongly driven the system. Equation (2.81) readily leads to a constraint on asymmetric perturbations as well,

$$\begin{aligned}\left|\frac{\partial\langle Q\rangle}{\partial F_{mn}}\right| &= \frac{1}{2}\left|\frac{\partial\langle Q\rangle}{\partial \ln W_{mn}} - \frac{\partial\langle Q\rangle}{\partial \ln W_{nm}}\right| \\ &\leq \max_{\mathcal{V}^{mn}} \left|\langle\!\langle Q, \delta(V^m)\rangle\!\rangle\right|,\end{aligned} \tag{2.82}$$

after noting that the covariance bound is symmetric with respect to W_{mn} and W_{nm}.

2.5 Topologies with optimal response

Analysis of the derivation of our bound Eq. (2.63) allows us to identify design principles for achieving the maximum response by determining how we should tune the rates W_{ij} to saturate the inequality. By changing the rates, we can effectively change the topology of the state-space graph, thus identifying what effective network structures are optimal.

There are two limits of the rates that we will encounter that lead to effective changes in the network structure: sending the rates to zero or to infinity. If we drive a pair of rates along a single edge e_{ij} to zero, $W_{ij} = W_{ji} = 0$, the resulting dynamics take place on a state-space graph with that edge deleted, as transitions along that edge are no longer possible. On the other hand, if we take a pair of rates on an edge e_{ij} to be large, the system will relax to a local steady state on the pair of nodes i and j very quickly: the remaining slow dynamics evolve on a state-space graph where the nodes i and j have been contracted into a single node.

We have found that to saturate Eq. (2.63) two conditions are required. The first is that there is a single cycle passing through our states m and n. Thus, we have to interrupt all cycles but one through m and n by deleting at least one of their edges, without disconnecting the graph, by sending the rates along that edge to zero. The second condition is that the graph has a single dominant topologically-consistent splitting V^{mn}. This is accomplished by taking all the rates on each vertex set V^m and V^n to be large such that they each form isolated dynamical islands. These islands are then linked together by a pair of slow rates that complete the unique cycle in the system. For the house graph, this is illustrated in Fig. 2.10 for a particular topologically-consistent splitting. The emergent optimal network

acts as a two state system, linked up by a single cycle.

2.6 Relaxing the bounds

Each of our bounds depends on a covariance with the indicator function $\delta(V^m)$. Measuring such correlations requires access to the occupation statistics of the states. This may be challenging even for moderately sized systems, where only coarser observations are possible. Thus, we now turn to deriving weakened, operational bounds on the covariance that depend only on observable properties of Q: its average $\langle Q \rangle$, variance $\langle\langle Q^2 \rangle\rangle$, maximum Q_M, and minimum Q_m.

To bound the covariance, we note that each $\delta(V^m)$ is nonnegative and bounded by one ($0 \leq \delta(V^m) \leq 1$). Let us consider the set of all such bounded observables, $\mathcal{B}O = \{A | 0 \leq A_i \leq 1\}$, of which $\delta(V^m)$ is a member. Then, the correlation we wish to constrain can trivially be bounded by the maximum over all steady-states π_i and all bounded observables, keeping the average $\langle Q \rangle$ and variance $\langle\langle Q^2 \rangle\rangle$ fixed:

$$\max_{\mathcal{V}^{mn}} \Big| \langle\langle Q, \delta(V^m) \rangle\rangle \Big| \leq \max_{\{\pi, A \in \mathcal{B}O | \langle Q \rangle, \langle\langle Q^2 \rangle\rangle\}} \Big| \langle\langle Q, A \rangle\rangle \Big|. \tag{2.83}$$

This weaker optimization is carried out in Section 2.9.5, with a result that depends on

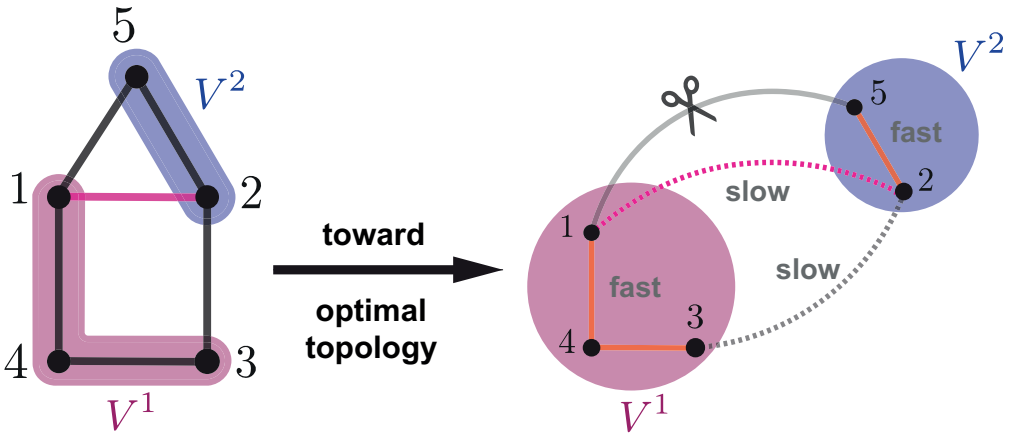


Figure 2.10: Example of an optimal network topology inherited from the topologically-consistent splitting $V^1 = \{1, 3, 4\}$, $V^2 = \{2, 5\}$. The rates on edge e_{15} are set to zero cutting that edge from the graph, leaving the system with a unique cycle. States internal to the islands defined by the topological splitting are contracted into a pair of single nodes by taking the rates along edges internal to the islands (orange) to be fast compared to the rates connecting the islands (dashed).

$\Gamma_Q = \min\{Q_M - \langle Q\rangle, \langle Q\rangle - Q_m, \sqrt{\langle\!\langle Q^2\rangle\!\rangle}\}$ via

$$\max_{\mathcal{V}^{mn}} \left| \langle\!\langle Q, \delta(V^m)\rangle\!\rangle \right| \leq \frac{\Gamma_Q \langle\!\langle Q^2\rangle\!\rangle}{\Gamma_Q^2 + \langle\!\langle Q^2\rangle\!\rangle}, \tag{2.84}$$

where the variance is required to fall below $\langle\!\langle Q^2\rangle\!\rangle \leq (Q_M - \langle Q\rangle)(\langle Q\rangle - Q_m)$. Saturation occurs when π_i is nonzero on only two states whose precise values depend on the value of Γ_Q.

To make contact with the bounds Eq. (2.31) and Eq. (2.32) derived in [21], we relax the constraint on the variance. Observing that Eq. (2.84) is monotonically increasing function of the variance, we can bound it by setting the variance to its maximum value $\langle\!\langle Q^2\rangle\!\rangle = (Q_M - \langle Q\rangle)(\langle Q\rangle - Q_m)$:

$$\max_{\mathcal{V}^{mn}} \left| \langle\!\langle Q, \delta(V^m)\rangle\!\rangle \right| \leq \frac{(Q_M - \langle Q\rangle)(\langle Q\rangle - Q_m)}{Q_M - Q_m} \tag{2.85}$$

$$\leq \frac{1}{4}(Q_M - Q_m), \tag{2.86}$$

where in the second line we have further maximized over all $Q_m \leq \langle Q\rangle \leq Q_M$. The first bound Eq. (2.85) is saturated when π_i is nonzero on only two states: one of the states, call it $i = M$, where Q_i reaches its maximum value Q_M and another state $i = m$ where the observable reaches its minimum value Q_m. The weaker bound Eq. (2.86) saturates when the probability is evenly split between those two states, $\pi_M = \pi_m = 1/2$.

By arriving at the previously derived bounds Eq. (2.31) and Eq. (2.32) through our more refined inequalities, we uncover how they emerge as the maximum response over all steady-state distributions with the mean observable held fixed. Under these conditions, the steady-state distribution is peaked at only two states. Thus, our more refined bounds provide the limits to steady-state response for an arbitrary steady-state distribution that can be spread among multiple states, accounting for how the response at different states must be related through topology as manifested through fluctuations across the topologically-consistent splittings. One could further imagine tighter operational bounds that constrain additional cumulants of the observables Q and $\delta(V^m)$.

2.7 Bounds on the nonequilibrium response of currents

So far we have focused on bounding the response of state observables. Bounding currents is a much more complicated process. One result we have obtained is an explicit expression for the symmetric response of a single current flowing between states m and n to perturbations

applied to that same edge. In Section 2.2.1, we derived the following expression for currents,

$$\bar{J}_{mn} = \frac{\alpha}{\mathcal{N}} \quad \text{with} \quad \alpha = \left[w(\mathcal{C}^{mn}) - w(\mathcal{C}^{nm}) \right] \quad \text{and} \quad \mathcal{N} = w(\mathcal{T}). \tag{2.87}$$

The spanning cycle graphs C^{mn} are formed by a single cycle oriented along the edge $n \to m$, with every other vertex linked by a unique path oriented towards the cycle. We note that the symmetric response (Eq. (2.24)) of α with respect to W_{mn} is equal to $-\alpha$ as each $w(C^{mn})$ contains a single weight of value equal to W_{mn}. The symmetric response of $\mathcal{N}$ is $w(\mathcal{T}^{mn})$, the sum of the weight of all trees containing edge e_{mn}. Combining these observations

$$\partial_{B_{mn}} \bar{J}_{mn} = -\frac{\alpha}{\mathcal{N}} \left[1 - \frac{w(\mathcal{T}^{mn})}{\mathcal{N}} \right]. \tag{2.88}$$

Upon normalizing the response by the current value itself, we obtain

$$\frac{\partial_{B_{mn}} \bar{J}_{mn}}{\bar{J}_{mn}} = -\left[1 - \frac{w(\mathcal{T}^{mn})}{\mathcal{N}} \right]. \tag{2.89}$$

As $w(\mathcal{T}^{mn})$ is a subset of $\mathcal{N}$ and both quantities are nonnegative, their ratio is necessarily bounded between 0 and 1. This leads to the bound

$$-1 \leq \partial_{B_{mn}} \ln \bar{J}_{mn} \leq 0, \tag{2.90}$$

In Fig. 2.11 we verify Eq. (2.90) by plotting the response $\partial_{B_{12}} \bar{J}_{12}$ to perturbations along e_{12} of the house graph (Fig. 2.1). Physically, this result expresses the intuitive fact that increasing an energetic barrier between two states can only suppress transitions between the states. After our initial derivation, the same bound was independently reported in [31].

2.8 Applying the bounds to receptor binding models

A central biochemical motif is the binding of ligands to a larger macromolecule [48, 49]. A relevant theoretical and experimental question is how sensitively this system responds to changes in the ligand concentration c, and how that depends on the number of binding sites N_B as well as other structural and thermodynamic characteristics [50]. In a kinetic model, like the one in Fig. 2.12, each state i is identified by the collection of binding sites in the macromolecule occupied by a ligand, with the number of bound sites denoted by the ligand-occupation number n_i. Binding rates $k_\alpha c$ are taken to be proportional to c, whereas unbinding rates $\tilde{k}_\alpha$ are concentration independent; beyond that the rates are fixed in accordance with local detailed balance Eq. (2.9). It is then common to study normalized

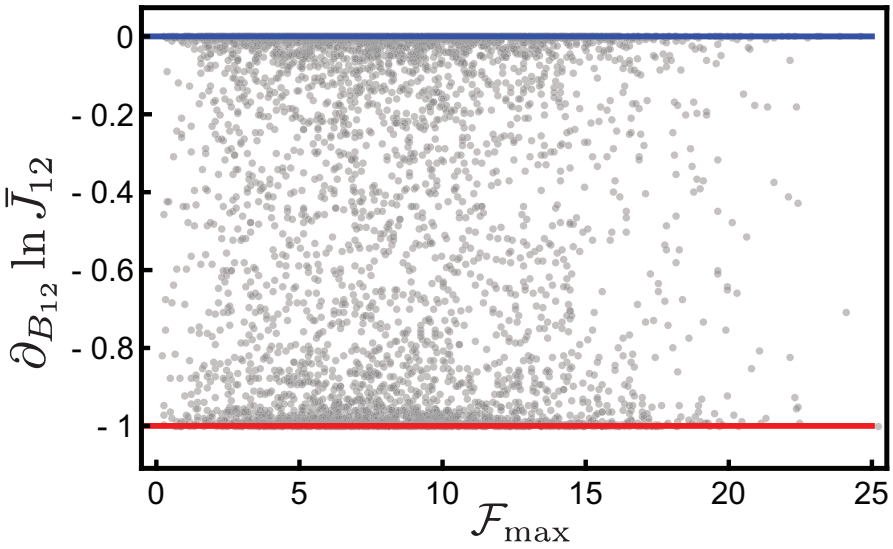


Figure 2.11: Response $\partial_{B_{12}} \ln \bar{J}_{12}$ as a function of the maximum cycle force $\mathcal{F}_{\max}$ around cycles containing edge e_{12} of the house graph (Fig. 2.1) for 1500 rate matrices with the logarithmic asymmetric $\ln(W_{ij}/W_{ji})$ and symmetric $\ln(W_{ij}W_{ji})$ parts sampled uniformly on $[-7, 7]$. All samples (gray) fall between the predicted upper (blue) and lower (red) bounds.

observables, $0 \leq f_i \leq 1$: the fraction of bound sites $f_i = n_i/N_B$ is one example [26], or in the context of gene regulation f_i could represent a normalized transcription rate [51, 52, 53] .

Before addressing nonequilibrium situations, we recall the equilibrium limits to cooperative binding. Statistical physics via the FDT Eq. (2.22) predicts that the sensitivity of an arbitrary normalized observable f_i is given by the correlation with the ligand-occupation number n_i,

$$\begin{aligned} \frac{\partial \langle f \rangle_c^{\text{eq}}}{\partial \ln c} &= \langle\!\langle f, n \rangle\!\rangle^{\text{eq}} \\ &\leq N_B \langle f \rangle_c^{\text{eq}} (1 - \langle f \rangle_c^{\text{eq}}) \leq N_B/4. \end{aligned} \tag{2.91}$$

Here, we have bounded the covariance using Eq. (2.85) after recognizing $n_i/N_B \leq 1$. This allows us to recover the classic prediction that the slope of the binding curve is limited by the number of binding sites N_B [26].

When driven away from equilibrium, binding can be more sensitive, as first demonstrated numerically in [54] in binding models with $N_B \geq 3$ binding sites. With the predictions presented above, we are limited to the model depicted in Fig. 2.12 with $N_B = 2$. To incorporate nonequilbrium driving, we imagine that the binding is coupled to ATP hydrolysis so that the sole thermodynamic driving force can be related to the chemical potential difference between ATP and its products: $F_C = \Delta\mu/kT$.

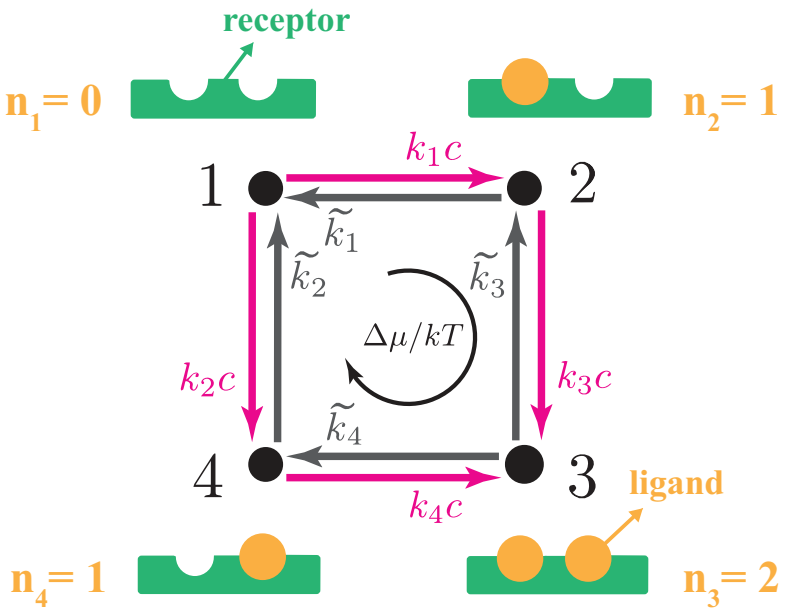


Figure 2.12: Representation of a ligand receptor model with two binding sites. Ligands (yellow) bind to a receptor (green) with $N_B = 2$ binding sites. Only the binding rates (pink) are proportional to the ligand concentration c.

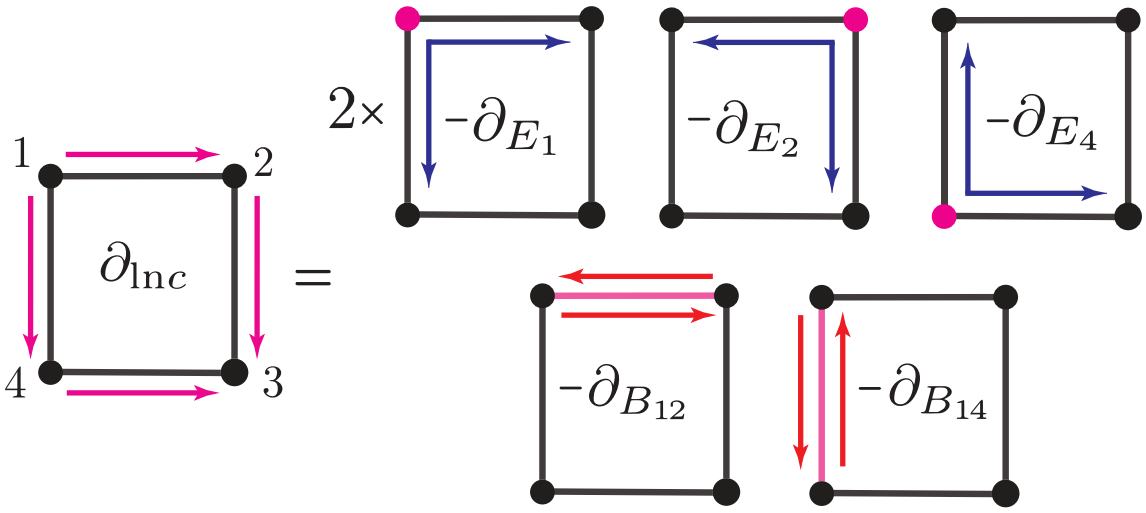


Figure 2.13: Decomposition of a c-perturbation into E-perturbations and a multi-edge B-perturbation for ligand receptor model with two binding sites following the graphical notation for the different types of perturbation illustrated in Fig. 2.4.

A logarithmic perturbation of c can be divided into E-perturbations Eq. (2.23) and a multi-edge symmetric perturbation, as in Fig. 2.13. Thus, by combining Eq. (2.26) and Eq. (2.73) we can bound the deviation of the sensitivity from the equilibrium-like prediction $\langle\!\langle f, n \rangle\!\rangle$ (Eq. (2.91))

$$\left| \frac{\partial \langle f \rangle_c}{\partial \ln c} - \langle\!\langle f, n \rangle\!\rangle \right| \leq \max_{\mathcal{V}^{24}} \left| \langle\!\langle f, \delta(V^2) \rangle\!\rangle \right| \tanh(\Delta\mu/4kT). \tag{2.92}$$

This can be simplified using the operational bounds Eq. (2.152) and Eq. (2.85),

$$\left| \frac{\partial \langle f \rangle_c}{\partial \ln c} - \langle\!\langle f, n \rangle\!\rangle \right| \leq \frac{\Gamma_f \langle\!\langle f^2 \rangle\!\rangle}{\Gamma_f^2 + \langle\!\langle f^2 \rangle\!\rangle} \tanh(\Delta\mu/4kT) \tag{2.93}$$

$$\leq \langle f \rangle_c (1 - \langle f \rangle_c) \tanh(\Delta\mu/4kT), \tag{2.94}$$

with $\Gamma_f = \min\{\langle f \rangle, 1 - \langle f \rangle, \sqrt{\langle\!\langle f^2 \rangle\!\rangle}\}$. We illustrate these inequalities in Fig. 2.14 for the representative optimal topology in Fig. 2.14(a) where $V^2 = \{2, 3\}$ and $V^4 = \{1, 4\}$. Our bound singles out two normalized observables of potential interest: when the observable is proportional to the ligand-occupation number, $f_i = n_i/2$, or when it is equal to the indicator function, $f_i = \delta_i(V^2)$. For both observables, we plot in Fig. 2.14(b) the deviation of the response from the equilibirum-like expectation with the limits imposed by Eq. (2.92) - Eq. (2.94) as a function of the concentration c for a lower-level of thermodynamic driving $\Delta\mu/kT = 1$ and a higher-level of driving $\Delta\mu/kT = 5$. We observe that the covariance bound Eq. (2.92) is only saturated at one point. Though, over the entire binding curve the bounds tend to be tighter with increasing thermodynamic driving, leading to an overall steeper binding curve as illustrated in Fig. 2.14(c). Of the two observables, the bounds are tighter when the observable is equal to the indicator function $f_i = \delta_i(V^2)$, when further the observable's variance equals the operational limit, $\langle\!\langle \delta^2 \rangle\!\rangle = \langle \delta \rangle (1 - \langle \delta \rangle)$.

For observables that monotonically increase with concentration, Eq. (2.92) bounds the sensitivity

$$\frac{\partial \langle f \rangle_c}{\partial \ln c} \leq \langle\!\langle f, n \rangle\!\rangle + \max_{\mathcal{V}^{24}} \left| \langle\!\langle f, \delta(V^2) \rangle\!\rangle \right| \tanh(\Delta\mu/4kT) \tag{2.95}$$

$$\leq \frac{\Gamma_f \langle\!\langle f^2 \rangle\!\rangle}{\Gamma_f^2 + \langle\!\langle f^2 \rangle\!\rangle} \left(2 + \tanh(\Delta\mu/4kT)\right) \tag{2.96}$$

$$\leq \langle f \rangle_c (1 - \langle f \rangle_c) \left(2 + \tanh(\Delta\mu/4kT)\right). \tag{2.97}$$

While these bounds saturate only at a single point along the binding curve, it is still worthwhile to investigate what concentration dependence would $\langle f \rangle_c$ require in order to have the

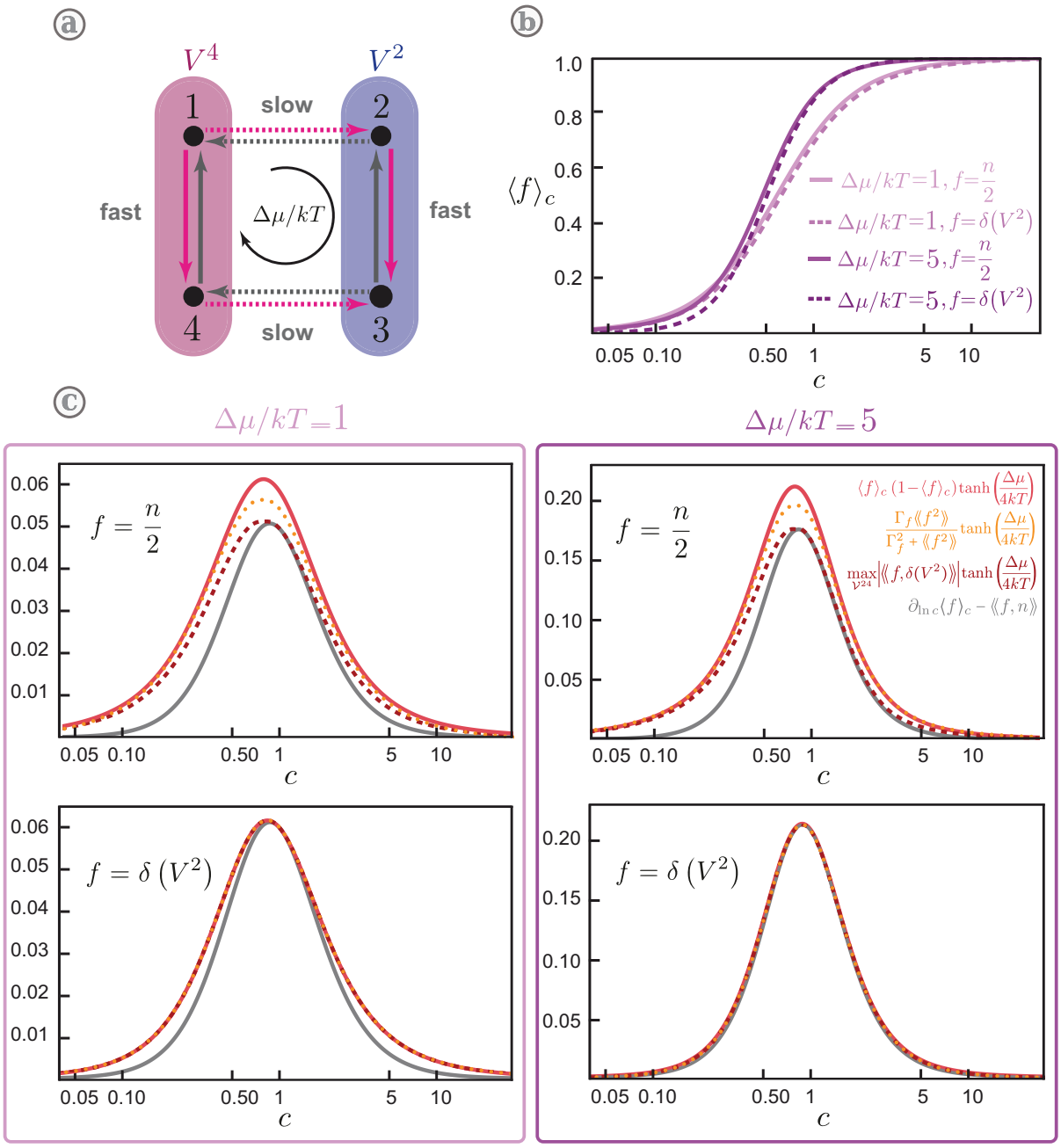


Figure 2.14: Saturating the inequalities in receptor binding: (a) Representation of the optimal network corresponding to the topological consistent splitting is $V^2 = \{1, 4\}$, $V^2 = \{2, 3\}$. The rates internal to the islands (pink and blue ovals) are fast compared to the rates connecting the islands (dashed). (b) For the optimal network in (a), the deviation of the response from the equilibrium prediction (gray) is compared to the bounds imposed by Eq. 2.92 (dashed dark red), Eq. 2.93 (orange) and Eq. 2.94 (red) as a function of concentration c for two observables $f = n/2$ (top) and $f = \delta(V^2)$ (bottom) at two values of thermodynamic driving, $\Delta\mu/kT = 1$ (left) and $\Delta\mu/kT = 5$ (right). (c) $\langle f\rangle_c$ as a function of c for both observables at the two values of thermodynamic driving. Parameter values are listed in Table 2.1.

	$\Delta\mu/kT = 1$	$\Delta\mu/kT = 5$
k_1	0.457986	0.457986
$\tilde{k}_1$	5.09981	37.6828
k_2	$0.457986\,\varepsilon$	$0.457986\,\varepsilon$
$\tilde{k}_2$	$1.20478\,\varepsilon$	$1.20478\,\varepsilon$
k_3	$3.09319\,\varepsilon$	$3.09319\,\varepsilon$
$\tilde{k}_3$	$0.251558\,\varepsilon$	$0.251558\,\varepsilon$
k_4	1.98634	14.6772
$\tilde{k}_4$	14.6772	14.6772

Table 2.1: Rate constants for the optimal network topology in Fig. 2.14. The values of the rates are chosen to fix the thermodynamic driving $\Delta\mu/kT = \{1, 5\}$. A multiplicative factor is included in the rates internal to the islands, $\varepsilon = 10^4$, in order to impose a timescale separation between transitions internal to the islands relative to between islands.

maximum steepness, saturating Eq. (2.97), along the entire binding curve. Assuming equality in Eq. (2.97) leads to a differential equation for the optimal binding curve whose solution is the Hill function [26]

$$\langle f \rangle_c^{\text{opt}} = \frac{c^H}{K^H + c^H}, \quad H = 2 + \tanh(\Delta\mu/4kT), \tag{2.98}$$

where the arbitrary constant K fixes the location of the curve via $\langle f \rangle_K^{\text{opt}} = 1/2$. The Hill coefficient H is enhanced beyond the structural equilibrium limit equal to 2 by the chemical driving. In Fig. 2.15(a), we verify the prediction in Eq. (2.97). The optimality of the Hill function Eq. (2.98) is illustrated in Fig. 2.15(b). Notably this curve does not bound any other binding curve, but for any given value of $\langle f \rangle$, it is the steepest.

2.9 Derivations

This section includes detailed derivations not presented in the previous Sections.

2.9.1 Graphical solution for inhomogeneous linear equations

Here, we show that

$$r_j = \frac{1}{\mathcal{N}} \sum_{\mathcal{F}^{mn},l} w\left(f_l^m \sqcup f_j^n\right) - w\left(f_j^m \sqcup f_l^n\right) \tag{2.99}$$

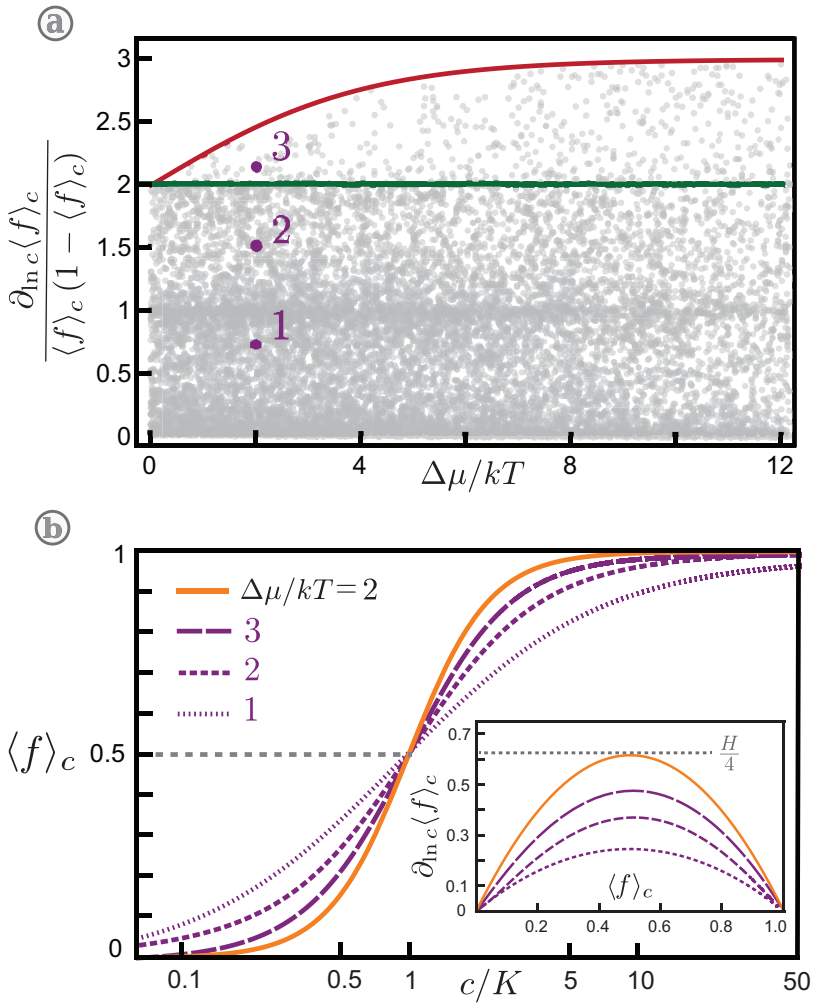


Figure 2.15: Nonequilibrium response in the receptor binding model: (a) Normalized response for 15000 random rate matrices with $c = 1$, logarithmic asymmetric $\ln(k_\alpha/\tilde{k}_\alpha)$ and symmetric $\ln(k_\alpha\tilde{k}_\alpha)$ parts sampled uniformly on $[-7, 7]$, and $f_1 = 0$, $f_3 = 1$, with $f_2 = f_4$ uniform in $[0.4, 0.6]$. All samples fall below the predicted bound Eq. 2.97, red. Green line is the maximum equilibrium response 2. (b) $\langle f\rangle_c$ as a function of c/K for three distinct rate matrices [purple points (a)] with $\Delta\mu/kT = 2$, which need not be Hill functions. Orange curve corresponds to the optimal Hill function Eq. 2.98. Inset: for any $\langle f\rangle_c$ sensitivity is bounded by the steepness of the Hill function, with a maximum of $H/4$. Parameters are listed in Table 2.2.

is the solution for the set of inhomogeneous linear equations

$$\sum_{j=1}^{N} W_{ij} r_j = \delta_{im} - \delta_{in} \quad \text{with} \quad \sum_j r_j = 0. \tag{2.100}$$

	Point 1	**Point 2**	**Point 3**
k_1	27.7025	12.530555	0.001309
$\tilde{k}_1$	0.467072	10.464932	1.789962
k_2	0.664276	29.406176	0.236687
$\tilde{k}_2$	8.4392	57.100834	272.941976
k_3	1.97131	320.175943	76.741704
$\tilde{k}_3$	0.142501	12.530555	0.023359
k_4	4.07565	516.106104	6.817252
$\tilde{k}_4$	0.00288908	516.106104	0.018179
$f_2 = f_4$	0.571365	0.559462	0.416399

Table 2.2: Rate constants and the observable values for the purple points 1, 2 and 3 in Fig. 2.15(a). The values are chosen so that the cycle force is equal to 2 in all cases. Note that in Fig. 2.15(b) the value of c for which $\langle f \rangle_c$ is equal to 0.5 depends on the rate constants. In the interest of creating a clear visualization, we numerically find these values, which we denote as K and plot each curve as a function of the normalized concentration c/K.

The requirement that the r_j sum to zero carries over naturally to the steady-state symmetric response, as probability conservation enforces $\sum_i \pi_i = 1$. We start by noting that Eq. (2.100) can be divided into three different types of equations depending on the value of i:

$$\sum_{j\neq m} W_{mj} r_j - \sum_{j\neq m} W_{jm} r_m = 1, \tag{2.101}$$

$$\sum_{j\neq n} W_{nj} r_j - \sum_{j\neq n} W_{jn} r_n = -1, \tag{2.102}$$

$$\sum_{j\neq h} W_{hj} r_j - \sum_{j\neq h} W_{jh} r_h = 0, \qquad h \neq m, n. \tag{2.103}$$

where conservation of probability is used to expand the diagonal elements of the rate matrix, $W_{ii} = -\sum_{j\neq i} W_{ji}$. We now check that Eq. (2.99) is the solution by direct calculation. First, substituting into Eq. (2.101), we arrive at the pair of sums

$$\sum_{j\neq m} W_{mj} r_j = \frac{1}{\mathcal{N}} \sum_{\substack{\mathcal{F}^{mn},l \\ j\neq m}} W_{mj} \left[w(f_l^m \sqcup f_j^n) - w(f_j^m \sqcup f_l^n) \right] \tag{2.104}$$

$$-\sum_{j\neq m} W_{jm} r_m = \frac{1}{\mathcal{N}} \sum_{\substack{\mathcal{F}^{mn},l \\ j\neq m}} W_{jm} w(f_m^m \sqcup f_l^n). \tag{2.105}$$

Now, each term in Eq. (2.104) and Eq. (2.105) corresponds to the weight of a subgraph formed from the addition of a single edge to a 2-forest. We address each sum in turn. The terms of the form $W_{mj}w(f_l^m \sqcup f_j^n)$ correspond to the weight of a subgraph constructed by adding e_{mj} to the 2-forest $f_l^m \sqcup f_j^n$, which forms a rooted spanning tree such that along the unique sequence of undirected edges linking n and m, the edge incident to m is oriented into m. We call the set of trees with this property $\mathcal{T}^{m\curvearrowleft n}$. All trees in the set are formed in this manner: the removal of the unique edge into m leads to the 2-forest $f_l^m \sqcup f_j^n$. Next, the terms in the second sum of Eq. (2.104) have the form $W_{mj}w(f_j^m \sqcup f_l^n)$. Here, the addition of the edge e_{mj} to the 2-forest $f_j^m \sqcup f_l^n$ closes a cycle in the f^m component, leaving the f^n component unaltered. This set of subgraphs we denote $\mathcal{C}^m\mathcal{F}^n$, where again the entire set is formed via this construction. The last type of term $W_{jm}w(f_m^m \sqcup f_l^n)$ appearing in Eq. (2.105), corresponds to the addition of e_{jm} to $f_m^m \sqcup f_l^n$, leading to one of two possibilities. The first possibility is that $j \in V(f^m)$ is in the same component as m. In this case, the resulting subgraph is an element of $\mathcal{C}^m\mathcal{F}^n$, the sum in Eq. (2.105) spanning over the entire set. The other possibility is that $j \notin V(f^m)$ is not in the same component as m, and e_{jm} links the two components of the forest forming a rooted spanning tree with the property that in the unique sequence of undirected edges linking n and m the edge incident to m is oriented out of m. This set we call $\mathcal{T}^{m\curvearrowright n}$. Putting everything together, we can write Eq. (2.101) as

$$\sum_{j\neq m} W_{mj}r_j - \sum_{j\neq m} W_{jm}r_m = \frac{1}{\mathcal{N}}\left[w\left(\mathcal{T}^{m\curvearrowleft n}\right) - w\left(\mathcal{C}^m\mathcal{F}^n\right) + w\left(\mathcal{T}^{m\curvearrowright n}\right) + w\left(\mathcal{C}^m\mathcal{F}^n\right)\right] \tag{2.106}$$

$$= \frac{w(\mathcal{T})}{\mathcal{N}} = 1, \tag{2.107}$$

where we recognized that $\mathcal{T} = \mathcal{T}^{m\curvearrowleft n} \cup \mathcal{T}^{m\curvearrowright n}$, since in any tree, along the path linking n and m the edge incident to m can only be oriented either into or out of m. Verification that Eq. (2.99) solves Eq. (2.102) follows along similar lines, so we omit the argument.

Lastly, we have to check Eq. (2.103). We proceed by analyzing the pair of sums

$$\sum_{j\neq h} W_{hj}r_j = \frac{1}{\mathcal{N}} \sum_{\substack{\mathcal{F}^{mn},l \\ j\neq h}} W_{hj}\left[w(f_l^m \sqcup f_j^n) - w(f_j^m \sqcup f_l^n)\right] \tag{2.108}$$

$$-\sum_{j\neq h} W_{jh}r_h = -\frac{1}{\mathcal{N}} \sum_{\substack{\mathcal{F}^{mn},l \\ j\neq h}} W_{jh}\left[w(f_l^m \sqcup f_h^n) - w(f_h^m \sqcup f_l^n)\right] \tag{2.109}$$

Again, sums on the right hand sides correspond to the weights of a set of subgraphs. The three sets that emerge are

1. $\mathcal{T}^{n\overset{h}{\curvearrowleft}m}$: spanning trees such that the sequence of undirected edges connecting n and m

pass through h, obtained by adding an edge incident to h that joins the two components of a 2-forest.

2. $\mathcal{C}^{m,h}\mathcal{F}^n$: spanning subgraphs composed of a cycle graph component containing the vertex m and a cycle through h, plus a tree component containing the vertex n. They are formed by adding an edge incident to h to a 2-forest $f^m \sqcup f^n$, where the edge links two vertices in the f^m component.

3. $\mathcal{F}^m\mathcal{C}^{n,h}$: spanning subgraphs composed of a cycle graph component containing the vertex n and a cycle through h, plus a tree component containing the vertex m. They are formed by adding an edge incident to h to a 2-forest $f^m \sqcup f^n$, where the edge links two vertices in the f^n component.

With this notation we separately combine the positive and negative terms in the sums in Eq. (2.108) and Eq. (2.109), so that they can be equated to the weights of these sets as

$$\sum_{\substack{\mathcal{F}^{mn},l \\ j\neq h}} W_{hj} w(f_l^m \sqcup f_j^n) + W_{jh} w(f_h^m \sqcup f_l^n) = w\left(\mathcal{F}^m\mathcal{C}^{n,h}\right) + w\left(\mathcal{C}^{m,h}\mathcal{F}^n\right) + w\left(\mathcal{T}^{n\overset{h}{\leftrightarrow}m}\right), \quad (2.110)$$

$$-\sum_{\substack{\mathcal{F}^{mn},l \\ j\neq h}} W_{hj} w(f_j^m \sqcup f_l^n) + W_{jh} w(f_l^m \sqcup f_h^n) = -w\left(\mathcal{C}^{m,h}\mathcal{F}^n\right) - w\left(\mathcal{F}^m\mathcal{C}^{n,h}\right) - w\left(\mathcal{T}^{n\overset{h}{\leftrightarrow}m}\right). \quad (2.111)$$

It is easy to see that both sums generate the entire sets $\mathcal{F}^m\mathcal{C}^{n,h}$ and $\mathcal{C}^{m,h}\mathcal{F}^n$. Furthermore, every element of $\mathcal{T}^{n\overset{h}{\leftrightarrow}m}$ is indeed contained in the sums on the left hand sides. To see this, let us follow the sequence of undirected edges from m to n in order. If we remove the unique edge immediately following vertex h, we obtain a 2-forest where m and h are in the same component, which corresponds to terms in one of the two sums in Eq. (2.110), either $W_{hj} w(f_j^m \sqcup f_l^n)$ or $W_{jh} w(f_h^m \sqcup f_l^n)$ depending on the orientation of the edge. Similarly, if we remove the edge immediately prior to the vertex h, we obtain a term in Eq. (2.111) where n and h share a component. Clearly, the sum of Eq. (2.110) and Eq. (2.111) is zero completing the argument.

2.9.2 Constrains on the structural coefficients for the single-edge perturbation

Here we derive the collection of linear equalities and inequalities that constrain the forest-tree ratios P_{ij}, and the structural coefficients $\mathcal{P}_{ij}$ Eqs. (2.51) to (2.54). Our main tool used during the derivation is the *Root-Swap* map. It is an invertible function that maps a rooted spanning tree and a rooted spanning 2-forest $(T_i, f_k^m \sqcup f_l^n)$ to another such pair keeping the

total weight fixed, but interchanging the roots of the tree and the forest:

$$w(T_i)w(f_k^m \sqcup f_l^n) \xrightarrow{\textit{Root-Swap}} \Big\{ w(T'_k)w(f_i'^m \sqcup f_l'^n) \quad \text{or} \quad w(T'_l)w(f_k'^m \sqcup f_i'^n) \Big\}. \tag{2.112}$$

Notably, which root of the forest ends up getting swapped depends on the input tree T_i. Though no matter the case, the output of the map is unique. To construct this map, we need to introduce additional definitions:

> *Source of directed edge*: denoted $s(f)$ – the starting vertex of a directed edge f;
>
> *Target of directed edge*: denoted $t(e)$ – the ending vertex of a directed edge e;
>
> *Doubly-rooted spanning 2-forest*: denoted $f_k^m \sqcup f_{lp,q}^n$ – a subgraph of G which is a spanning 2-forest formed as follows. The first component f_k^m contains vertex m and is rooted at k. The second component $f_{lp,q}^n$ contains vertex n and is doubly-routed with roots l and p split by a branch point q, i.e., every edge is directed as in f_l^n and f_p^n when those directions coincide, and otherwise directed toward l if between q and l and toward p if between q and p. Note that $f_k^m \sqcup f_l^n$, coincides with any doubly-rooted 2-forest of the type $f_k^m \sqcup f_{pl,p}^n$ or $f_k^m \sqcup f_{lp,p}^n$ for any p.

The *Root-Swap* map is then built from repeated applications of the *Edge-Swap* operation:

> *Edge-Swap*: Input $\big(T_q, f_k^m \sqcup f_{lp,q}^n\big)$. Remove from $f_{lp,q}^n$ the unique edge e pointing out of the branch point q towards p, the vertex in the middle position. This splits $f_{lp,q}^n$ into two disjoint components: D, which contains vertex n, and $\bar{D}$, which does not. Insert e into T_q, thereby creating a cycle C oriented from $q = s(e)$ to $t(e)$. Note that this cycle may be formed by only two edges, e and another edge in the opposite orientation. Starting from $t(e)$, march along the links of this cycle C following its orientation, until you find the first edge f that reconnects $\bar{D}$ back to D or to the other component f_k^m. Remove f to form a new rooted tree $T'_{s(f)}$, and insert f back into the pieces of the 2-forest to form either $f_{kp,s(f)}'^m \sqcup f_l'^n$, $f_k'^m \sqcup f_{lp,s(f)}'^n$, or $f_{lk,s(f)}'^m \sqcup f_p'^n$. Output the result: $\Big(T'_{s(f)}, f'^m_{kp,s(f)} \sqcup f'^n_l\Big)$, $\Big(T'_{s(f)}, f'^m_k \sqcup f'^n_{lp,s(f)}\Big)$ or $\Big(T'_{s(f)}, f'^m_{lk,s(f)} \sqcup f'^n_p\Big)$.

With these tools in hand, we implement the *Root-Swap* map on the pair $(T_i, f_k^m \sqcup f_l^n)$ as follows, where we assume without loss of generality that $i \in V(f^n)$ initially. An illustration is presented in Fig. 2.16:

> *Root-Swap* $(T_i, f_k^m \sqcup f_l^n)$:
> (1) Identify the input with the doubly-rooted forest as $\big(T_i, f_k^m \sqcup f_{il,i}^n\big)$.

(2) Repeatedly apply *Edge-Swap* until there is no edge pointing out of the branch point in the appropriate direction, which occurs when the branch point becomes one of the original roots with pair $(T'_k, f'^m_{ik,k} \sqcup f'^n_l)$ or $(T'_l, f'^m_k \sqcup f'^n_{il,l})$.
(3) Output the result, either $\left(T'_k, f'^m_i \sqcup f'^n_l\right)$ or $\left(T'_l, f'^m_k \sqcup f'^n_i\right)$.

The above algorithm always terminates. When the initial edge e is removed during the first application of *Edge-Swap*, the component D containing n may also include the original root l, or the original root may be in $\bar{D}$ with D instead rooted at i. In the first instance we initially have tree-components D_l and $\bar{D}_i$, every subsequent application of *Edge-Swap* will grow the component $\bar{D}_i$ by marching the branch point closer to l or k, until the branch point merges with one of the original roots, and the algorithm terminates. In the second instance, after removal of e we have components D_i and $\bar{D}_l$, with each application of *Edge-Swap* shrinking $\bar{D}_l$ until the branch point merges with l, terminating the algorithm. This second instance is what is illustrated in Fig. 2.16.

Root-Swap is also invertible. Each step of *Edge-Swap* can be reversed, as we can always find the swapped edge by following the cycle C along its reverse orientation. Moreover, the starting point can be identified since the root of the tree serves as the first branch point, which we see by looking at the terminal configurations, $(T'_k, f'^m_{ik,k} \sqcup f'^n_l)$ or $(T'_l, f'^m_k \sqcup f'^n_{il,l})$. We would begin by removing the unique edge pointing into k or l. Finally the weights are conserved, as edges are merely swapped; no edges are created, destroyed or reoriented.

With *Root-Swap* in hand we now utilize it to derive Eqs. (2.51) to (2.54):

1. Derivation of $P_{ij} \leq P_{mj}, P_{in}$ Eq. (2.51):

The derivation proceeds by using the *Root-Swap* map to change the subscripts in the forest-tree weights. With this in mind, we begin by manipulating the definition of P_{mj} Eq. (2.44) by multiplying and dividing by the weight all spanning trees rooted at i, and then apply the *Root-Swap* map:

$$P_{mj} = \frac{1}{\mathcal{D}}\left[\sum_{\mathcal{T}}\sum_{\mathcal{F}^{mn}} w(T_i)w(f^m_m \sqcup f^n_j)\right] \tag{2.113}$$

$$= \frac{1}{\mathcal{D}}\left[\sum_{\{T_m, f^m_i \sqcup f^n_j\}\in\mathcal{RS}} w(T_m)w(f^m_i \sqcup f^n_j) + \sum_{\{T_j, f^m_m \sqcup f^n_i\}\in\mathcal{RS}} w(T_j)w(f^m_m \sqcup f^n_i)\right] \tag{2.114}$$

where we defined

$$\mathcal{D} = \sum_{\mathcal{T}} w(T_m)\sum_{\mathcal{T}} w(T_i)\sum_{\mathcal{T}} w(T_j) \tag{2.115}$$

to simplify the notation. Now importantly, application of the *Root-Swap* map does not necessarily generate every weighted product of trees and forests, but in general only a subset

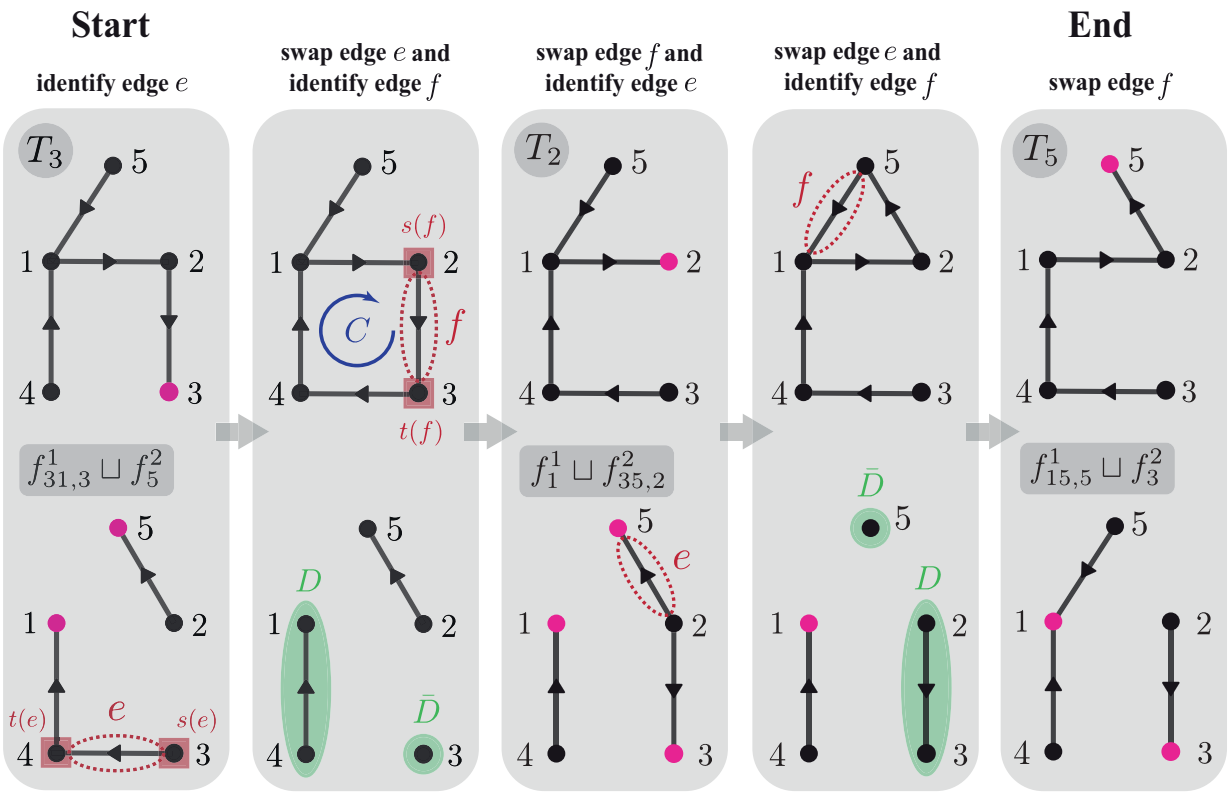


Figure 2.16: Example application of the *Root-Swap* map taking the pair $(T_3, f^1_1 \sqcup f^2_5)$ as input and outputting the pair $(T'_5, f'^1_1 \sqcup f'^2_3)$. Each panel contains one step of the *Edge-Swap* operation.

of $\mathcal{T} \times \mathcal{F}^{mn}$. This is notated in Eq. (2.114) by confining the sum to the set $\mathcal{R}S$ of tree-forest pairs generated by application of *Root-Swap* to Eq. (2.113). We now claim that in fact all pairs in the first term, which are of the form $w(T_m)w(f^m_i \sqcup f^n_j)$, are generated under *Root-Swap* and that the sum actually extends over all tree-forest pairs. This follows by imagining there is a tree-forest pair $w(T_m)w(f^m_i \sqcup f^n_j)$ not generated by *Root-Swap* (not in $\mathcal{R}S$). We can then apply the inverse *Root-Swap* map, which can only generate a pair of the form $w(T_i)w(f^m_m \sqcup f^n_j)$ (as m cannot be in the f^n component). Due to the uniqueness of the *Root-Swap* map, this term had to be present in the original sum in Eq. (2.113), and therefore there are no pairs $w(T_m)w(f^m_i \sqcup f^n_j)$ not in $\mathcal{R}S$. Thus, we have

$$P_{mj} = \frac{1}{\mathcal{D}} \left[\sum_{\mathcal{T}, \mathcal{F}^{mn}} w(T_m)w(f^m_i \sqcup f^n_j) + \sum_{\{T_j, f^m_m \sqcup f^n_i\} \in \mathcal{R}S} w(T_j)w(f^m_m \sqcup f^n_{ji}) \right] \tag{2.116}$$

$$\geq P_{ij}, \tag{2.117}$$

where we have identified P_{ij} Eq. (2.44) and noted the remaining terms are positive. A similar argument leads to the conclusion that $P_{in} \geq P_{ij}$ as well.

2. Derivation of $P_{mi} + P_{ij} = P_{mj} + P_{ji}$ Eq. (2.52) and $P_{in} + P_{ji} = P_{jn} + P_{ij}$ Eq. (2.53):
   We rearrange the sum $P_{mi} + P_{ij}$ as

$$P_{mi} + P_{ij} = \frac{1}{\mathcal{D}} \left[\sum_{\mathcal{T}, \mathcal{F}^{mn}} w(T_j) w(f_m^m \sqcup f_i^n) + \sum_{\mathcal{T}, \mathcal{F}^{mn}} w(T_m) w(f_i^m \sqcup f_j^n) \right], \tag{2.118}$$

so that we can apply the *Root-Swap* map to interchange the subscripts

$$P_{mi} + P_{ij} = \frac{1}{\mathcal{D}} \left[\sum_{\{T_m, f_j^m \sqcup f_i^n\} \in \mathcal{R}S'} w(T_m) w(f_j^m \sqcup f_i^n) + \sum_{\{T_i, f_m^m \sqcup f_j^n\} \in \mathcal{R}S'} w(T_i) w(f_m^m \sqcup f_j^n) \right], \tag{2.119}$$

with $\mathcal{R}S'$ the image of the *Root-Swap* map applied to Eq. (2.118). Again, we claim that the sums actually extend over all tree-forest pairs, $\mathcal{T} \times \mathcal{F}^{mn}$. Indeed, one can check, for example, if there were a pair $w(T_m) w(f_j^m \sqcup f_i^n) \notin \mathcal{R}S'$, application of the inverse *Root-Swap* map would generate a term in one of the sums in Eq. (2.118), leading to a contradiction. Thus, we have

$$P_{mi} + P_{ij} = \frac{1}{\mathcal{D}} \left[\sum_{\mathcal{T}, \mathcal{F}^{mn}} w(T_m) w(f_j^m \sqcup f_i^n) + \sum_{\mathcal{T}, \mathcal{F}^{mn}} w(T_i) w(f_m^m \sqcup f_j^n) \right] \tag{2.120}$$

$$= P_{ji} + P_{mj}. \tag{2.121}$$

An identical argument holds for $P_{in} + P_{ji} = P_{jn} + P_{ij}$ Eq. (2.53).

3. Derivation of $\mathcal{P}_{mn} \leq 1$ Eq. (2.54):
   From the definition of the structural coefficients Eq. (2.44), we have

$$\mathcal{P}_{mn} = \left(\sqrt{w(\mathcal{C}^{mn})} + \sqrt{w(\mathcal{C}^{nm})} \right)^2 \frac{\sum_{\mathcal{F}^{mn}} w(f_m^m \sqcup f_n^n)}{\sum_{\mathcal{T}} w(T_m) \sum_{\mathcal{T}} w(T_n)}. \tag{2.122}$$

Next, we expand the denominator into sums of trees with the perturbed edge $T^{mn} \in \mathcal{T}^{mn}$ and those without $S^{mn} \in \mathcal{S}^{mn}$ (irrespective of orientation), and then apply the inequality of

arithmetic and geometric means (AM-GM inequality),

$$\sum_{\mathcal{T}} w(T_m) \sum_{\mathcal{T}} w(T_n) = \left[\sum_{\mathcal{T}^{mn}} w\left(T_m^{mn}\right) + \sum_{\mathcal{S}^{mn}} w\left(S_m^{mn}\right) \right] \left[\sum_{\mathcal{T}^{mn}} w\left(T_n^{mn}\right) + \sum_{\mathcal{S}^{mn}} w\left(S_n^{mn}\right) \right] \tag{2.123}$$

$$\geq \left(\sqrt{\sum_{\mathcal{T}^{mn}} w\left(T_m^{mn}\right) \sum_{\mathcal{S}^{mn}} w\left(S_n^{mn}\right)} + \sqrt{\sum_{\mathcal{T}^{mn}} w\left(T_n^{mn}\right) \sum_{\mathcal{S}^{mn}} w\left(S_m^{mn}\right)} \right)^2 . \tag{2.124}$$

Now, take the terms inside the first square root $w\left(T_m^{mn}\right) w\left(S_n^{mn}\right)$. Because T_m^{mn} is rooted at m, edge e_{mn} linking m and n must indeed be oriented towards m. Removal of this edge e_{mn} from T_m^{mn} forms a 2-forest, $f_m^m \sqcup f_n^n$. If we then add that edge to S_n^{mn}, we form a cycle-graph C^{mn}. Thus, $w\left(T_m^{mn}\right) w\left(S_n^{mn}\right) = w(C^{mn}) w(f_m^m \sqcup f_n^n)$. Applying this argument to every term above, we find

$$\sum_{\mathcal{T}} w(T_m) \sum_{\mathcal{T}} w(T_n) \geq \left(\sqrt{w(\mathcal{C}^{mn})} + \sqrt{w(\mathcal{C}^{nm})} \right)^2 \sum_{\mathcal{F}^{mn}} w(f_m^m \sqcup f_n^n), \tag{2.125}$$

which implies the desired result.

2.9.3 Vertices of the convex polytope

To determine the vertices of the feasible polytope, we first determine its dimension d given by the number of trivially nonzero structural coefficients less the number of linearly independent equality constraints:

$$\begin{aligned} d &= \overbrace{1}^{\mathcal{P}_{mn}} + \overbrace{2(N-2)}^{\mathcal{P}_{mi},\mathcal{P}_{in}\ (i\neq m,n)} + \overbrace{(N-2)(N-3)}^{\mathcal{P}_{ij}\ (i\neq j\neq m,n)} - \overbrace{(N-2)}^{\text{(B34)}} - \overbrace{(N-2)(N-3)/2}^{\text{(B35)},(i>j)} \\ &= 1 + N - 2 + (N-2)(N-3)/2 \end{aligned} \tag{2.126}$$

A vertex is then the unique solution to a subset of at least d of the inequalities in Eq. (2.56) and Eq. (2.57) solved as equalities. In the following, we show that at these vertices all structural coefficients $\mathcal{P}_{ij}$ are either one or zero, that is they form a subset of the vertices of the positive unit hypercube.

We only need to focus on a collection of d linearly independent structural coefficients, which we choose to be $\mathcal{P}_{mn}$, $\mathcal{P}_{mi}$ $(i \neq m, n)$, and $\mathcal{P}_{ij}$ $(i > j;\ i \neq j \neq m, n)$. We then express all the inequalities in (2.56) and (2.57) in terms of our independent variables. After eliminating

any redundant inequalities, we find for $i > j$; $i \neq j \neq m, n$,

$$0 \leq \mathcal{P}_{ij} \leq \mathcal{P}_{mj} \leq \mathcal{P}_{mn} \leq 1 \tag{2.127}$$

$$\mathcal{P}_{mi} + \mathcal{P}_{ij} \leq \mathcal{P}_{mn} \tag{2.128}$$

$$\mathcal{P}_{mj} \leq \mathcal{P}_{mi} + \mathcal{P}_{ij} \tag{2.129}$$

Clearly, if $\mathcal{P}_{mn} = 0$, then all structural coefficients are zero, leading to a trivial solution that clearly cannot be a maximum. Thus, $\mathcal{P}_{mn} \neq 0$.

So we consider the case where $\mathcal{P}_{mn} \neq 0$. We will now argue that at every vertex all the structural coefficients are either zero or one. To determine the vertices we systematically choose one inequality to saturate and use that equality to fix a structural coefficient. Doing that d times leads to the conditions for a vertex, as long as the solution is consistent with all other inequalities. We will begin by carrying out this program only for the string of inequalities in (2.127), identifying a collection of vertices on the unit hypercube. Any other vertices can then be obtained by starting from a known vertex and then marching along every edge of the feasible polytope until arriving at another vertex, in the spirit of the simplex algorithm [47]. It will turn out that starting from any known vertex, every edge connects it to another already-identified vertex on the unit hypercube.

First, we fix $\mathcal{P}_{mn} = 1$, saturating one inequality. For each remaining structural coefficient we can fix its value by saturating either the upper or lower inequality in Eq. (2.127). Specifically, we can choose either $\mathcal{P}_{mj} = 1$ or $\mathcal{P}_{mj} = \mathcal{P}_{i'j}$, for some $i' > j$. If we fixed a particular structural coefficient via the second equality, $\mathcal{P}_{mj} = \mathcal{P}_{i'j}$, then the only way to fix $\mathcal{P}_{i'j}$ using one of the remaining inequalities in Eq. (2.127) is to set $\mathcal{P}_{mj} = \mathcal{P}_{i'j} = 0$. This automatically sets all $\mathcal{P}_{mj} = \mathcal{P}_{ij} = 0$, for $i > j$. On the other hand, if we had set $\mathcal{P}_{mj} = 1$, then each $\mathcal{P}_{ij}$ for $i > j$ can be set to either $\mathcal{P}_{ij} = 0$ or $\mathcal{P}_{ij} = \mathcal{P}_{mj} = 1$. However, an inconsistency could arise with Eq. (2.128), if $\mathcal{P}_{ij} = 1$ and $\mathcal{P}_{mi} = 1$ ($2 \leq 1$). So we must choose consistently $\mathcal{P}_{mi} = 0$ with $\mathcal{P}_{ij} = 1$. Similarly, an inconsistency could arise with Eq. (2.129), if $\mathcal{P}_{mj} = 1$ and $\mathcal{P}_{ij} = 0$ with $\mathcal{P}_{mi} = 0$ ($1 \leq 0$). Thus, we must choose consistently $\mathcal{P}_{ij} = 1$, when $\mathcal{P}_{mj} = 1$ and $\mathcal{P}_{mi} = 0$.

We can characterize these vertices by recognizing that the condition that either $\mathcal{P}_{mj} = 1$ or $\mathcal{P}_{mj} = 0$ splits the set of states into two groups. In the first group $\mathcal{P}_{mj} = 1$, and j is associated with the f^n component. Let us collect these nodes into a set $j \in V^n$. The remaining set of nodes, $\mathcal{P}_{mi} = 0$, can be characterized via Eq. (2.58) by the condition $\mathcal{P}_{in} = \mathcal{P}_{mn} - \mathcal{P}_{mi} = 1$, which allows us to associate them to the f^m component. We call this set $i \in V^m$. The remaining vertex conditions are consistent with this splitting. Indeed, if $i \in V^m$, then $\mathcal{P}_{mi} = 0$, implies $\mathcal{P}_{qi} = 0$ for all q. Similarly, $j \in V^n$, then $\mathcal{P}_{mj} = 1$, implies either $\mathcal{P}_{qj} = 1$ or $\mathcal{P}_{qj} = 0$, depending

on whether $q \in V^m$ or not.

The vertices we have so far identified turn out to be all the possible vertices. We can see this by using already identified vertices to detect any remaining ones. Vertices are linked by edges of the polytope, where $d-1$ inequalities are saturated. Thus, starting from any vertex we can identify additional vertices by marching along all incident edges. We accomplish this by taking one of the saturated equalities, and relax it by varying one of the coefficients. This gives us the one degree of freedom required to delineate the edge. To this end, let us choose a polytope vertex and label the states as $j_\alpha, j_\beta, \cdots \in V^n$ and $i_\alpha, i_\beta, \cdots \in V^m$. Then one can check that nearly all the inequalities in Eq. (2.127)-Eq. (2.129) are saturated except

$$0 = \mathcal{P}_{j_\beta j_\alpha} \leq \mathcal{P}_{m j_\alpha} = 1, \qquad 0 = \mathcal{P}_{m,i_\alpha} + \mathcal{P}_{i_\beta,i_\alpha} \leq \mathcal{P}_{mn} = 1. \tag{2.130}$$

These inequalities provide the only freedom for saturating new inequalities where we would find a new vertex. Thus, we can move any one of these coefficients from their current value to a new value that saturates either of these inequalities. Though, at this new vertex it is clear again all structural coefficients will in fact be zero or one, as claimed. Furthermore, as we move any coefficient from $1 \to 0$ or $0 \to 1$, the remaining equalities will keep all coefficients in the feasible polytope. The effect is just switching one of the states between the V^n and V^m sets.

The last step in characterizing the vertices of the polytope is to recognize that the splitting of the graph nodes into the sets V^n and V^m has to be consistent with the definition of the structural coefficients in terms of 2-forests, illustrated in Fig. 2.7. Take for example an $i \in V^m$ and $j \in V^n$, so that at this vertex $\mathcal{P}_{ij} = 1$; however, this structural coefficient can only be nonzero if there exists at least one forest of the form $f_i^m \sqcup f_j^n$. Thus, the only potential allowable choices of V^n and V^m is when they align with the vertex sets of a 2-forest, that is $V^n = V(f^n)$ and $V^m = V(f^m)$.

2.9.4 Constrains on the structural coefficients for the multiple-edge perturbation

Here, we show that $\mathcal{P}^H_{mn} \leq 1$ holds for multiple-edge perturbations. From its definition, we have

$$\mathcal{P}^H_{mn} = \left(\sqrt{w(\mathcal{C}^H)} + \sqrt{w(\tilde{\mathcal{C}}^H)}\right)^2 \frac{\sum_{\mathcal{F}^{mn}} w(f_m^m \sqcup f_n^n)}{\sum_{\mathcal{T}} w(T_m) \sum_{\mathcal{T}} w(T_n)}. \tag{2.131}$$

We lower bound the denominator by observing that since H^{mn} is only incident to the rest of the graph at two nodes, any path in a tree that links m and n must be contained entirely in H^{mn} or its complement; in other words no path can enter or leave H^{mn} without crossing

through m or n. This allows us to divide the sum over trees in the denominator into those $T^{n\overset{H}{\leftrightarrow}m}$ where the unique path that connects m and n is contained entirely in H^{mn} and those $S^{n\overset{H}{\leftrightarrow}m} \in \mathcal{S}^{n\overset{H}{\leftrightarrow}m}$ where the path is entirely contained in the complement of H^{mn}:

$$\begin{aligned}&\sum_{\mathcal{T}} w(T_m) \sum_{\mathcal{T}} w(T_n) \\ &\quad = \left[\sum_{\mathcal{T}^{n\overset{H}{\leftrightarrow}m}} w\left(T_m^{n\overset{H}{\leftrightarrow}m}\right) + \sum_{\mathcal{S}^{n\overset{H}{\leftrightarrow}m}} w\left(S_n^{m\overset{H}{\leftrightarrow}m}\right) \right] \left[\sum_{\mathcal{T}^{n\overset{H}{\leftrightarrow}m}} w\left(T_n^{n\overset{H}{\leftrightarrow}m}\right) + \sum_{\mathcal{S}^{n\overset{H}{\leftrightarrow}m}} w\left(S_n^{n\overset{H}{\leftrightarrow}m}\right) \right].\end{aligned} \tag{2.132}$$

Expanding the denominator and applying the AM-GM inequality, we have

$$\begin{aligned}&\sum_{\mathcal{T}} w(T_m) \sum_{\mathcal{T}} w(T_n) \geq \\ &\quad \left(\sqrt{\sum_{\mathcal{T}^{n\overset{H}{\leftrightarrow}m}, \mathcal{S}^{n\overset{H}{\leftrightarrow}m}} w\left(T_m^{n\overset{H}{\leftrightarrow}m}\right) w\left(S_n^{n\overset{H}{\leftrightarrow}m}\right)} + \sqrt{\sum_{\mathcal{T}^{n\overset{H}{\leftrightarrow}m}, \mathcal{S}^{n\overset{H}{\leftrightarrow}m}} w\left(T_n^{n\overset{H}{\leftrightarrow}m}\right) w\left(S_n^{m\overset{H}{\leftrightarrow}m}\right)} \right)^2.\end{aligned} \tag{2.133}$$

Now, take the terms inside the first square root $w\left(T_m^{n\overset{H}{\leftrightarrow}m}\right) w\left(S_n^{n\overset{H}{\leftrightarrow}m}\right)$. The part of the tree $T_m^{n\overset{H}{\leftrightarrow}m}$ inside the perturbed region H^{mn} is by definition connected and rooted at m. By contrast, the part of the tree $S_n^{n\overset{H}{\leftrightarrow}m}$ in H^{mn} is not connected, but is composed of two connected components, one rooted at m and the other rooted at n. This is the only arrangement possible in a tree rooted at n if m is to be linked to n in the complement of H^{mn}. We now swap all the perturbed edges in $T_m^{n\overset{H}{\leftrightarrow}m}$ with all the perturbed edges in $S_n^{n\overset{H}{\leftrightarrow}m}$. The tree that initially had the path between m and n in H^{mn} is now disconnected and forms a 2-forest $f_m^m \sqcup f_n^n$. The tree that did not have a path between m and n in H^{mn} has one now, forming a cycle-graph in the set $\mathcal{C}^H$. This is just like the single-edge perturbation, except instead of swapping a single edge, we swap all the perturbed edges together. Applying a similar argument to the second sum in Eq. (2.133), results in

$$\sum_{\mathcal{T}} w(T_m) \sum_{\mathcal{T}} w(T_n) \geq \left(\sqrt{w(\mathcal{C}^H)} + \sqrt{w(\tilde{\mathcal{C}}^H)} \right)^2 \sum_{\mathcal{F}^{mn}} w(f_m^m \sqcup f_n^n), \tag{2.134}$$

which implies the desired result

$$\left| \sum_{e_{kl} \in H^{mn}} \frac{\partial \langle Q \rangle}{\partial B_{kl}} \right| \leq \max_{\mathcal{V}^{mn}} \left| \langle\!\langle Q, \delta(V^m) \rangle\!\rangle \right| \tanh\left(\mathcal{F}_{\max}/4\right). \tag{2.135}$$

Here, $\mathcal{F}_{\max}$ is the maximum cycle force over all cycles that straddle the perturbed and unperturbed regions passing through the two vertices m and n.

2.9.5 Bounds on covariance

To bound the recurring covariance $\max_{\mathcal{V}^{mn}} \left| \langle\!\langle Q, \delta(V^m) \rangle\!\rangle \right|$ we start by noting that each $\delta(V^m)$ is nonnegative and bounded by one ($0 \leq \delta(V^m) \leq 1$). Let us consider the set of all such bounded observables, $\mathcal{B}O = \{A | 0 \leq A_i \leq 1\}$, of which $\delta(V^m)$ is a member. Then, the correlation we wish to constrain can be bounded by the maximum over all steady-states π_i and all bounded observables, keeping the average $\langle Q \rangle$ and variance $\langle\!\langle Q^2 \rangle\!\rangle$ fixed:

$$\max_{\mathcal{V}^{mn}} \left| \langle\!\langle Q, \delta(V^m) \rangle\!\rangle \right| \leq \max_{\{\pi, A \in \mathcal{B}O | \langle Q \rangle, \langle\!\langle Q^2 \rangle\!\rangle\}} \left| \langle\!\langle Q, A \rangle\!\rangle \right|. \tag{2.136}$$

To facilitate this calculation, we use that $\langle Q \rangle$ is fixed to shift the observable so that its mean is zero,

$$\tilde{Q}_i = Q_i - \langle Q \rangle, \tag{2.137}$$

and introduce a notation for the value of the fixed variance $\langle\!\langle Q^2 \rangle\!\rangle = \langle \tilde{Q}^2 \rangle = v$. As the covariance is invariant to constant shifts, our problem becomes

$$\max_{\{\pi, A \in \mathcal{B}O | \langle Q \rangle, \langle\!\langle Q^2 \rangle\!\rangle\}} \left| \langle\!\langle Q, A \rangle\!\rangle \right| = \max_{\{\pi, A \in \mathcal{B}O | \langle \tilde{Q} \rangle, \langle \tilde{Q}^2 \rangle\}} \left| \langle\!\langle \tilde{Q}, A \rangle\!\rangle \right| = \max_{\{\pi, A \in \mathcal{B}O | \langle \tilde{Q} \rangle, \langle \tilde{Q}^2 \rangle\}} \left| \sum_{j=1}^{N} \tilde{Q}_j A_j \pi_j \right|. \tag{2.138}$$

We first perform the maximization over all $A \in \mathcal{B}O$. As $\langle \tilde{Q} \rangle = 0$, we can divide the vertices into those where the observable is positive $\tilde{Q}^+ = \{i | \tilde{Q}_i \geq 0\}$, and those where it is negative $\tilde{Q}^- = \{i | \tilde{Q}_i < 0\}$. We can clearly maximize Eq. (2.138) by only keeping terms in the sum that have the same sign. If we keep only positive terms, by setting $A_i = 1$ for all $i \in \tilde{Q}^+$ and $A_i = 0$ otherwise, we find

$$\max_{\{\pi, A \in \mathcal{B}O | \langle Q \rangle, \langle\!\langle Q^2 \rangle\!\rangle\}} \left| \langle\!\langle Q, A \rangle\!\rangle \right| = \max_{\{\pi | \langle \tilde{Q} \rangle, \langle \tilde{Q}^2 \rangle\}} \left| \sum_{j \in \tilde{Q}^+} \tilde{Q}_j \pi_j \right|. \tag{2.139}$$

Notice if we had kept only negative terms, we would have arrived at the same bound as $\left| \sum_{j \in \tilde{Q}^+} \tilde{Q}_j \pi_j \right| = \left| \sum_{j \in \tilde{Q}^-} \tilde{Q}_j \pi_j \right|$. We have thus reduced our analysis to the following linear opti-

mization problem:

$$\max_{\pi} \left| \sum_{j \in \tilde{Q}^+} \tilde{Q}_j \pi_j \right| \quad \text{such that} \tag{2.140}$$

$$0 \le \pi_i \le 1 \tag{2.141}$$

$$\sum_i \pi_i = 1 \tag{2.142}$$

$$\sum_i \tilde{Q}_i \pi_i = 0 \tag{2.143}$$

$$\sum_i \tilde{Q}_i^2 \pi_i = v. \tag{2.144}$$

The potential maxima are given by the vertices of the convex polytope defined by the above constraints. With three equality constraints the dimension of this polytope is $d = N - 3$. Thus, at a vertex we need to saturate d of the inequalities in Eq. (2.141). We can only do this by setting d of the π_i's to either 1 or 0; however, if any $\pi_i = 1$, then probability conservation (Eq. (2.142)) requires the probability at all other sites to be zero, which is a situation where we cannot maintain the mean constraint on $\tilde{Q}$ Eq. (2.143). As a result, vertices are characterized by the steady-state distribution having only three nonzero elements and the rest zero. To have $\sum_i \tilde{Q}_i \pi_i = 0$, one of the nonzero elements of π must be in $\tilde{Q}^+$, let us call this state $i = +$ and have value $\tilde{Q}_+$; another must be in the negative region $\tilde{Q}^-$, let us call it $i = -$ with value $-\tilde{Q}_-$; the third state we will call $i = o$ and we will take it to have a value in between $-\tilde{Q}_- \le \tilde{Q}_o \le \tilde{Q}_+$. The probabilities at these sites, π_+, π_o and π_-, are then determined by the equality constraints Eqs. (2.142) to (2.144), which read

$$\begin{pmatrix} 1 & 1 & 1 \\ \tilde{Q}_+ & \tilde{Q}_o & -\tilde{Q}_- \\ \tilde{Q}_+^2 & \tilde{Q}_o^2 & \tilde{Q}_-^2 \end{pmatrix} \begin{pmatrix} \pi_+ \\ \pi_o \\ \pi_- \end{pmatrix} = \begin{pmatrix} 1 \\ 0 \\ v \end{pmatrix}. \tag{2.145}$$

The unique solution is

$$\pi_+ = \frac{v - \tilde{Q}_o \tilde{Q}_-}{(\tilde{Q}_+ - \tilde{Q}_0)(\tilde{Q}_+ + \tilde{Q}_-)}, \qquad \pi_o = \frac{\tilde{Q}_+ \tilde{Q}_- - v}{(\tilde{Q}_+ - \tilde{Q}_0)(\tilde{Q}_0 + \tilde{Q}_-)}, \qquad \pi_- = \frac{v + \tilde{Q}_+ \tilde{Q}_0}{(\tilde{Q}_0 + \tilde{Q}_-)(\tilde{Q}_+ + \tilde{Q}_-)}. \tag{2.146}$$

Positivity of the steady-state probabilities further requires the constraints

$$v \ge \tilde{Q}_o \tilde{Q}_-, \qquad \tilde{Q}_+ \tilde{Q}_- \ge v, \qquad v \ge -\tilde{Q}_+ \tilde{Q}_o. \tag{2.147}$$

The value of our objective function at a vertex then depends on whether $\tilde{Q}_o$ is positive or negative:

$$\left|\sum_{j\in\tilde{Q}^+}\tilde{Q}_j\pi_j\right|_{\text{vertex},\tilde{Q}_0\leq 0} = \left|\tilde{Q}_+\pi_+\right| = \left|\frac{\tilde{Q}_+(v-\tilde{Q}_o\tilde{Q}_-)}{(\tilde{Q}_+-\tilde{Q}_0)(\tilde{Q}_++\tilde{Q}_-)}\right| \tag{2.148}$$

$$\left|\sum_{j\in\tilde{Q}^+}\tilde{Q}_j\pi_j\right|_{\text{vertex},\tilde{Q}_0\geq 0} = \left|\tilde{Q}_+\pi_+ + \tilde{Q}_o\pi_o\right| = \left|\frac{\tilde{Q}_-(v+\tilde{Q}_+\tilde{Q}_0)}{(\tilde{Q}_0+\tilde{Q}_-)(\tilde{Q}_++\tilde{Q}_-)}\right|. \tag{2.149}$$

To find the vertex with the largest value, we next have to maximize over the values of the observable. We will analyze the case $\tilde{Q}_o \geq 0$, and as it turns out, the maximum is the same when $\tilde{Q}_o \leq 0$. We will allow $\tilde{Q}_+$, $\tilde{Q}_o$, and $\tilde{Q}_-$ to vary over all real numbers between the observable's maximum and minimum value, even if such values are not attained at any particular state. Thus, we now have the bound on the maximum

$$\max_\pi\left|\sum_{j\in\tilde{Q}^+}\tilde{Q}_j\pi_j\right| \leq \max_{\tilde{Q}_+,\tilde{Q}_-,\tilde{Q}_o}\left|\frac{\tilde{Q}_-(v+\tilde{Q}_+\tilde{Q}_0)}{(\tilde{Q}_0+\tilde{Q}_-)(\tilde{Q}_++\tilde{Q}_-)}\right|. \tag{2.150}$$

Observe that this is a monotonically increasing function of $\tilde{Q}_o$, whose value is limited due to Eq. (2.147) by the constraints $\tilde{Q}_o \leq v/\tilde{Q}_- \leq \tilde{Q}_+$. Thus, the maximum is attained when the value of the observable takes is largest value $\tilde{Q}_o = v/\tilde{Q}_-$,

$$\max_\pi\left|\sum_{j\in\tilde{Q}^+}\tilde{Q}_j\pi_j\right| \leq \max_{\tilde{Q}_-}\left|\frac{\tilde{Q}_-v}{\tilde{Q}_-^2+v}\right|. \tag{2.151}$$

Notice that $\tilde{Q}_+$ has dropped from the calculation, because when $\tilde{Q}_o = v/\tilde{Q}_-$ there is no probability on $\pi_+ = 0$, and the distribution is now peaked at two sites: $\pi_o = \tilde{Q}_-^2/(\tilde{Q}_-^2+v)$ and $\pi_- = v/(\tilde{Q}_-^2+v)$. Now, Eq. (2.151) has a local maximum of $\sqrt{v}/2$ when $\tilde{Q}_- = \sqrt{v}$, and this is the maximum as long $\sqrt{v}$ is a value obtainable by the observable. However, $\tilde{Q}_-$ is constrained by the observable's smallest, or most negative, value $\tilde{Q}_m = Q_m - \langle Q\rangle$ and its largest value $\tilde{Q}_M = Q_M - \langle Q\rangle$ via $v/\tilde{Q}_M \leq v/\tilde{Q}_o = \tilde{Q}_- \leq |\tilde{Q}_m|$. This leads to three possibilities: (1) $\sqrt{v} \leq \tilde{Q}_m, \tilde{Q}_M$ lies in the domain of $\tilde{Q}_-$ and the maximum is $\sqrt{v}/2$. (2) If $\tilde{Q}_m \leq \tilde{Q}_M$, then we can have $|\tilde{Q}_m| \leq \sqrt{v} \leq \tilde{Q}_M$. In this case, the maximum is obtained on the boundary where $\tilde{Q}_- = |\tilde{Q}_m|$ with value $|\tilde{Q}_m|v/(\tilde{Q}_m^2+v)$. (3) If $\tilde{Q}_M \leq \tilde{Q}_m$, then we can have $|\tilde{Q}_M| \leq \sqrt{v} \leq \tilde{Q}_m$. In this case, the maximum is obtained on the boundary where $\tilde{Q}_- = \tilde{Q}_M$ with value $\tilde{Q}_M v/(\tilde{Q}_M^2+v)$. Finally, the largest value that v can attain occurs when the domain for $\tilde{Q}_-$ shrinks to nothing, which occurs when $v = \tilde{Q}_M|\tilde{Q}_m|$. Collecting these

observation leads to the expression

$$\max_{\mathcal{V}^{mn}} \Big| \langle\!\langle Q, \delta(V^m) \rangle\!\rangle \Big| \leq \frac{\Gamma_Q \langle\!\langle Q^2 \rangle\!\rangle}{\Gamma_Q^2 + \langle\!\langle Q^2 \rangle\!\rangle}, \tag{2.152}$$

with $\Gamma_Q = \min\{Q_M - \langle Q \rangle, \langle Q \rangle - Q_m, \sqrt{\langle\!\langle Q^2 \rangle\!\rangle}\}$. The variance is required to fall below $\langle\!\langle Q^2 \rangle\!\rangle \leq (Q_M - \langle Q \rangle)(\langle Q \rangle - Q_m)$. Saturation occurs when π_i is nonzero on only two states whose precise values depend on the value of Γ_Q.

2.10 Summary

In this Chapter we built upon a class of trade-offs, a recently established collection of thermodynamic bounds on steady-state response. These past predictions are limited by not accounting for correlations between responses at different microscopic configurations. Here we include these correlations and demonstrate that the response of a physical observable is bounded not just by thermodynamic driving, but also by a measure of fluctuations sensitive to the topology of the microscopic state-space. Importantly, the only kinetic information required to determine these fluctuations is the structure of the state-space, no knowledge of the values of kinetic rates is needed.

We have demonstrated that the maximum response over all rates holding the steady-state distribution fixed is given by the maximal fluctuations of the observable across the system's topologically-consistent splittings. For symmetric edge perturbations this is further constrained by the degree of nonequilibrium driving as measured by the thermodynamic force. These trade-offs quantify the role network topology plays in shaping the connection between response and fluctuations away from equilibrium.

We can also view our predictions through the lens of the FDT. In the FDT, the relevant metric of fluctuations is between the observable and a perturbation-dependent, conjugate observable. In the predictions derived here, the perturbation-dependent quantity that appears in the covariance is the indicator function for a topologically-consistent splitting. In this way, the topologically-consistent splittings act as a kind of optimal conjugate observable, whose fluctuations help us organize our observations about response. Our predictions suggest that the deep connection between response, fluctuations, and network structure can be fruitfully quantified in some generality.

CHAPTER 3

Cooperativity in Nonequilibrium Receptor Binding Models

3.1 Introduction

In the early twentieth century, C. Bohr measured hemoglobin's fractional saturation as a function of oxygen partial pressure, revealing that the oxygen binding curves exhibit a characteristic sigmoidal shape [55]. This sigmoidal shape cannot be captured by the simple reaction $Hb + O_2 \rightleftharpoons HbO_2$, in which oxygen ($O_2$) binds to a single hemoglobin (Hb) molecule. This simple observation led to extensive research devoted to uncovering the structure of hemoglobin and the mechanisms by which oxygen binds to it.

A. Hill developed a phenomenological model that reproduces the characteristic shape of hemoglobin binding curves [56]. A central aspect of the model is the assumption that hemoglobin forms aggregates, with each molecule within the aggregate able to bind a single oxygen. This was later understood to correspond to hemoglobin's four heme groups, each serving as an oxygen-binding site. The so-called Hill curves are now widely used to describe the binding of ligands to general macromolecules. They express the average fractional occupation of the binding sites, $\langle\Theta\rangle$, as a function of ligand concentration c. Its functional form is fully described by two parameters – a dissociation constant K and the Hill coefficient H:

$$\langle\Theta\rangle = \frac{c^H}{K^H + c^H}. \tag{3.1}$$

The Hill coefficient dictates the steepness of the binding curve, where higher values correspond to a sharper transition from low to high occupancy, as illustrated in Fig. 3.1. The Hill coefficient carries intertwined meanings. In equilibrium, its maximum value cannot surpass the total number of binding sites. This maximum is also only reached in the limit of strong cooperativity, where the binding of a ligand at one site affects the binding at remaining sites. For this reason, the Hill coefficient is often employed as an empirical measure of cooperativity.

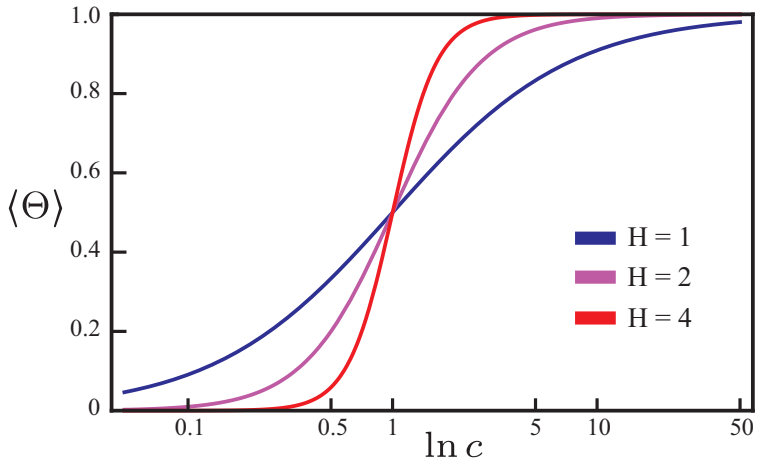


Figure 3.1: Hill curves (Eq. 3.1) for different values of the Hill coefficient: 1 (blue), 2 (pink) and 4 (red), and dissociation constant $K = 1$. When the fractional occupation $\langle\Theta\rangle$ is zero the macromolecule is empty, when its one all the sites of the macromolecule are occupied. Higher Hill coefficients correspond to increased steepness of the curve.

Mechanistically, the source of cooperative interactions lies in allosteric interactions: ligand binding at one site induces conformational changes that modulate the properties of other sites in the macromolecule. This idea is embodied in two classical models of cooperative receptor binding. In the MWC model, all sites switch concertedly between a low-affinity conformation, which binds ligands weakly, and a high-affinity conformation, which binds ligands strongly. In the KNF model, sites change conformation one at a time, with binding at one site causing neighboring sites to switch to a high-affinity conformation [57].

Beyond the empirical measure provided by the Hill coefficient, several competing mechanistic definitions of cooperativity exist for equilibrium systems [58]. Some cooperativity measures are rooted in the structure of the energy landscape, while others are derived from the binding kinetics. How these definitions extend to nonequilibrium systems remains elusive. In this Chapter, we begin by examining the precise meaning of the equilibrium principle that strong cooperativity is necessary for the Hill coefficient to reach its maximum value. We then extend our analysis to nonequilibrium systems by introducing two novel definitions of cooperativity. We conclude by analyzing the conditions under which cooperativity produces the steepest possible binding curves in nonequilibrium systems.

3.2 The role of cooperativity in equilibrium receptor binding models

To study equilibrium receptor binding models we consider a receptor with N_B binding sites in the presence of a ligand reservoir at concentration c. To each receptor site i we assign an occupation variable $\sigma_i \in \{0, 1\}$, with $\sigma_i = 1$ if the site is occupied and $\sigma_i = 0$ otherwise. The system has 2^{N_B} distinct states, each fully specified by the configuration vector $\sigma = (\sigma_1, \sigma_2, \ldots, \sigma_{N_B})$. For notational convenience, we will often equivalently represent a state by the set of its occupied sites $S = \{i \mid \sigma_i = 1\}$, with the empty receptor denoted as $\varnothing$.

To describe the energetics of the system, we must consider the chemical potential, μ, which accounts for the free energy cost of transferring a ligand from the reservoir to a receptor site. Notably, μ depends on the ligand concentration, with $\mu \propto \ln c$ [57]. If the binding sites are independent, the free energy of a state is simply the sum of the energies of the occupied sites E_i with the additional contribution from the ligand reservoir:

$$E_S = \sum_{i=1}^{N_B} E_i \sigma_i - \mu \sum_{i=1}^{N_B} \sigma_i, \tag{3.2}$$

setting, with no loss of generality, the energy of the empty receptor to zero.

If the binding sites are not independent – meaning that a collection of occupied sites affects the binding at another site – the energy of a given state must include interaction terms, which we refer to as cooperativity. For a set Ω of interacting sites, the corresponding cooperativity term is denoted by J_Ω, where the number of sites in the set, $|\Omega|$, determines the order of the interaction. In particular, when $|\Omega| = 2$, the cooperativity corresponds to a pairwise interaction between two sites. Terms with $|\Omega| > 2$ describe higher-order cooperativities, with the highest possible order corresponding to an all-to-all interaction involving all binding sites. For example, for a three-binding sites receptor illustrated in Fig. 3.2, all the combinations of interacting sites are $\{1, 2\}$, $\{1, 3\}$, $\{2, 3\}$ and $\{1, 2, 3\}$, with corresponding cooperativity terms J_{12}, J_{13}, J_{23} and J_{123}. With this notation, the free energy of a state S is given as

$$E_S = \sum_{i=1}^{N_B} E_i \sigma_i - \sum_{\Omega} J_\Omega \prod_{i \in \Omega} \sigma_i - \mu \sum_{i=1}^{N_B} \sigma_i. \tag{3.3}$$

Our objective is to examine thoroughly the general statement that, at equilibrium, strong cooperativity is necessary for the Hill coefficient to reach its maximum value. If the average fractional occupation number follows a Hill curve (Eq. (3.1)), its response to logarithmic changes in ligand concentration is

$$\partial_{\ln c} \langle \Theta \rangle = H \langle \Theta \rangle (1 - \langle \Theta \rangle). \tag{3.4}$$

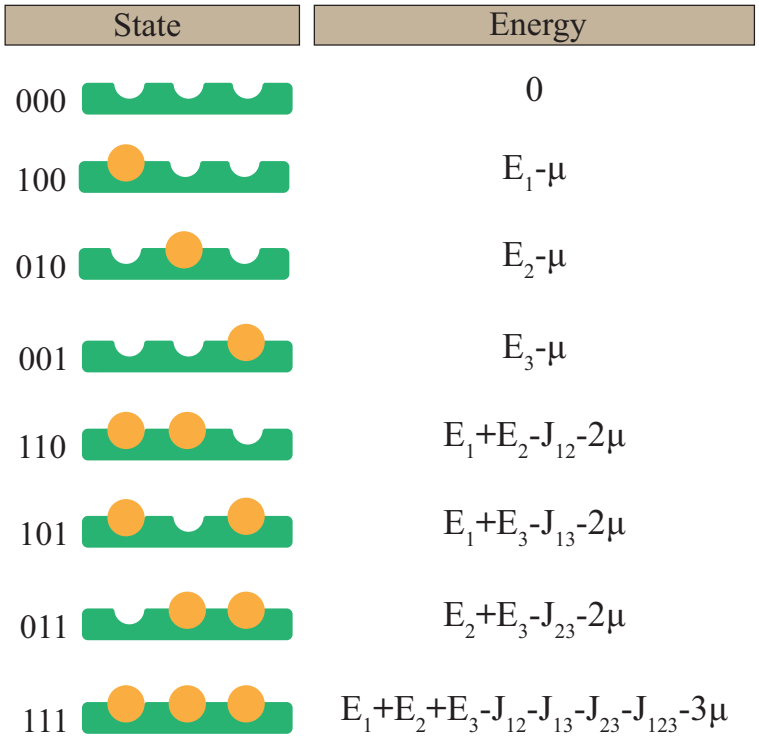


Figure 3.2: Diagrammatic representation of states and energies for a receptor binding model with three-binding sites. The receptor is shown in green, and the bound ligands in yellow. The chemical potential, μ, represents the effective energy cost of removing a ligand from the reservoir and binding it to the receptor. J_{12}, J_{13}, and J_{23} are measures of pairwise cooperativity, and J_{123} is a measure of higher-order cooperativity capturing the interaction between all three sites. Without loss of generality the energy of the empty receptor is set to zero. Note that although the binding sites are represented identically, sites can assume different energies.

We thus adopt the ratio

$$\max_c \frac{\partial_{\ln c}\langle\Theta\rangle}{\langle\Theta\rangle(1-\langle\Theta\rangle)} \tag{3.5}$$

as a measure of the Hill coefficient. The average fractional occupation number is a function of the state occupation probabilities π_S in the form

$$\langle\Theta\rangle = \sum_{m=1}^{N_B} \frac{m}{N_B} \sum_{S\epsilon\mathcal{S}_m} \pi_S, \tag{3.6}$$

with $\mathcal{S}_m$ the set of all states with exactly m sites bound. In equilibrium, the Gibbs distribu-

tion determines the occupation probabilities of the states:

$$\pi_S = \frac{e^{-\beta E_S}}{Z} \quad \text{with} \quad Z = \sum_S e^{-\beta E_S}, \tag{3.7}$$

with the inverse temperature $\beta = 1$ for simplicity. We begin by noting that the free energy depends on the ligand concentration only through the chemical potential, and that term is proportional to the number of occupied sites in the state (Eq. (3.3)). Then, for a state S with m occupied sites

$$\partial_{\ln c}\pi_S = m\pi_S - \pi_S \sum_{m=1}^{N_B} m \sum_{S\in\mathcal{S}_m} \pi_S. \tag{3.8}$$

Then the response of $\langle\Theta\rangle$ to logarithmic changes in concentration is

$$\partial_{\ln c}\langle\Theta\rangle = \sum_{m=1}^{N_B} \frac{m^2}{N_B} \sum_{S\in\mathcal{S}_m} \pi_S - \left[\sum_{m=1}^{N_B} \frac{m}{N_B} \sum_{S\in\mathcal{S}_m} \pi_S\right]\left[\sum_{m=1}^{N_B} m \sum_{S\in\mathcal{S}_m} \pi_S\right] \tag{3.9}$$

$$= \sum_{m=1}^{N_B} \frac{m^2}{N_B} \sum_{S\in\mathcal{S}_m} \pi_S - N_B\langle\Theta\rangle^2. \tag{3.10}$$

To simplify the expression further, we add and subtract $N_B\langle\Theta\rangle$ (Eq. (3.6)), which gives

$$\partial_{\ln c}\langle\Theta\rangle = N_B\langle\Theta\rangle - N_B\langle\Theta\rangle^2 - \sum_{m=1}^{N_B} m\left(1 - \frac{m}{N_B}\right) \sum_{S=\mathcal{S}_m} \pi_S. \tag{3.11}$$

Normalizing the response by $\langle\Theta\rangle(1-\langle\Theta\rangle)$, leaves us with

$$\frac{\partial_{\ln c}\langle\Theta\rangle}{\langle\Theta\rangle(1-\langle\Theta\rangle)} = N_B - \frac{1}{\langle\Theta\rangle(1-\langle\Theta\rangle)} \sum_{m=1}^{N_B-1} m\left(1 - \frac{m}{N_B}\right) \sum_{S\in\mathcal{S}_m} \pi_S, \tag{3.12}$$

where we recognized that the term in the summation vanishes when $m = N_B$. The maximum value that Eq. (3.12) can assume is therefore N_B, since all terms in the summation are non-negative. This maximum is reached when the occupation probabilities of all states, except for the empty state ($m = 0$) and the fully occupied state ($m = N_B$), are zero[1].

We then determine the values for the cooperative interactions that set the occupation probabilities of partially occupied states to vanish, while maintaining both the empty and fully occupied states occupation probabilities finite. In particular, we seek to demonstrate that this condition can be achieved solely through pairwise cooperativity, with no higher-order cooperativities.

[1]Alternatively, this conclusion can be derived by directly invoking the Fluctuation-Dissipation Theorem as discussed in Section 2.8

As a simplifying assumption we consider the case in which all individual binding sites have the same intrinsic energy, $E_i = \alpha$. The pairwise cooperativity terms between two sites i and j assume the same value, $J_{ij} = \gamma$, and all higher-order cooperativities are set to zero. Under these conditions, inserting the state energies (Eq. (3.3)) into the Gibbs distribution yields the ratio between the occupation probability of a state with m bound sites and that of the empty state as

$$\frac{\pi_{S_m}}{\pi_{\varnothing}} = e^{-\alpha m + \gamma \frac{m(m-1)}{2} + \mu m}. \tag{3.13}$$

Here we use the fact that a state with m occupied sites contains $\binom{m}{2} = \frac{m(m-1)}{2}$ distinct pairwise interaction terms, corresponding to the number of two-element subsets that can be formed from m sites. Now we choose α and γ such that they satisfy $2\alpha = \gamma(N_B - 1)$, so that the occupation probabilities take the form

$$\frac{\pi_{S_m}}{\pi_{\varnothing}} = e^{-\alpha m\left(1 - \frac{m-1}{N_B - 1}\right) + \mu m}. \tag{3.14}$$

Since the factor $1 - \frac{m-1}{N_B - 1}$ is strictly positive for all $0 < m < N_B$, taking α to be sufficiently large suppresses the probabilities of all partially occupied states. At the same time, the ratio between the fully occupied and empty states remains finite, $\pi_{N_B}/\pi_{\varnothing} = e^{-\mu N_B}$, as it no longer depends on α. With this, we have shown that the Hill coefficient can reach its maximum value without invoking higher-order cooperativities, provided that the pairwise cooperativities are sufficiently strong[2].

3.3 Definitions of cooperativity in nonequilibrium receptor binding models

We describe nonequilibrium receptor binding models using the framework of Markov-jump processes, introduced in Section 2.2. These processes can be conveniently represented as graphs, where each node corresponds to a state of the system and edges denote the allowed transitions between states. The directed edges carry weights $W_{S,S'}$, which encode the transition rate from state S' to state S. For practical reasons, the notation in this section differs from that used in Chapter 2 in its use of the comma. These transitions arise from the binding or unbinding of single ligands, with all binding rates proportional to the ligand concentration c. Figure 3.2 is an illustrative example of the graphical representation for a receptor binding model with three binding sites.

[2]Note that this is not the only way for the system to reach its maximum Hill coefficient – the same outcome is possible with nonidentical energy and interaction values, as well as through higher-order cooperativities.

While equilibrium steady-state distributions are fully determined by the energy landscape, nonequilibrium steady-state distributions can be fully specified only through knowledge of the kinetic details set by the transition rates. Thus, defining cooperativity in a nonequilibrium system requires a formulation expressed in terms of rates.

Estrada *et al.* [54] introduce a measure of nonequilibrium cooperativity that characterizes how the binding and unbinding dynamics changes when a ligand binds to a receptor that has bound ligands, compared to when it binds to an empty receptor. Specifically, consider the transition in which a ligand binds to a site i while the system is in state S, resulting in a new state we denote as $i \cup S$. We define

$$K_{i,S} = \frac{W_{i\cup S,\, S}}{W_{S,\, i\cup S}}, \tag{3.15}$$

as the ratio between binding and unbinding rates from state S to state $i \cup S$. The associated cooperativity measure is then defined as

$$J_{i,S} = \frac{K_{i,S}}{K_{i,\varnothing}}, \tag{3.16}$$

with $\varnothing$ the empty receptor state. The number of occupied sites in S determines the order of the cooperativity. In particular, pairwise cooperativity corresponds to the case $|S| = 1$. $J_{i,S} = 1$ indicates non-cooperative binding. $J_{i,S} > 1$ corresponds to positive cooperativity, where the presence of bound sites in S enhances the binding rate to site i. Conversely, $J_{i,S} < 1$ indicates negative cooperativity, in which the presence of bound sites in S reduces the binding rate to site i.

Notably, this measure of cooperativity is non-reciprocal – its value depends on the order in which sites are bound. To illustrate this concept, consider two states that are identical except that one has a ligand bound at site i, denoted $i \cup S'$, and the other has a ligand bound at site j, denoted $j \cup S'$. In a system driven out of equilibrium, the measures of cooperativity $J_{j,i\cup S'}$ and $J_{i,j\cup S'}$ can take different values.

In contrast to what is observed in equilibrium, achieving maximum nonequilibrium sensitivity under this definition (Eq. (3.16)) requires higher-order cooperativities. Although this definition has historical roots in Pauling's work on cooperative oxygen binding to hemoglobin [59], it does not reduce to the intuitive energy-based definition for cooperativities when the system is kept in equilibrium. In the following, we introduce two alternative definitions of cooperativity valid far from equilibrium: one based on energetics and the other on dynamics. We then examine whether these definitions also require higher-order cooperativities for a system to reach maximum sensitivity, as measured by the Hill coefficient.

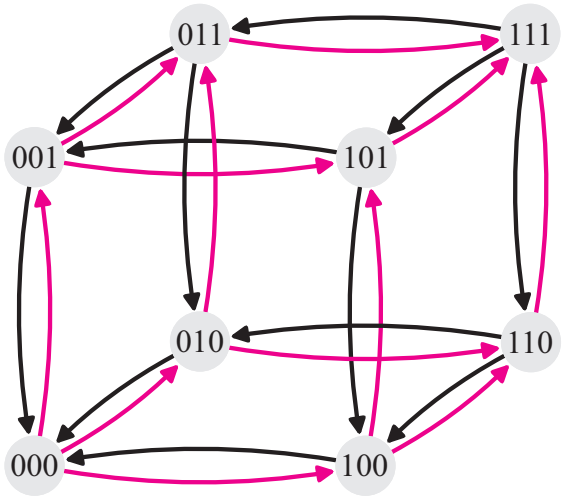


Figure 3.3: Graph representing a nonequilibrium receptor binding model with three binding sites. The binding rates (pink) correspond to transitions that lead to the binding of a ligand. The state notation follows the definition used in Fig.3.2.

3.3.1 Energetics-inspired definition

When assigning energies to a system's states, the notion of cooperative interactions arises naturally. To define an energetics-inspired notion of cooperativity, we first construct a mapping in equilibrium that links cooperative interactions encoded in the state energies to transition rates. This mapping is then promoted to nonequilibrium systems, providing a definition of nonequilibrium cooperativity.

To relate energies and rates in equilibrium, we evoke local detailed balance, which connects the ratio of transition rates between states S and S' to the free energy difference between those states:

$$E_S - E_{S'} = \ln\left(\frac{W_{S',S}}{W_{S,S'}}\right). \tag{3.17}$$

To construct the mapping, we begin by evaluating the pairwise cooperativity. We focus first on the transitions among three states: the empty receptor, a state S_i with a single ligand bound at site i, and the state $i \cup S_j$, in which two ligands are bound at sites j and i. Using the equilibrium state-energy definition in Eq. (3.3) together with local detailed balance (Eq. (3.17)), we find

$$E_i + \mu = \ln\left(\frac{W_{\varnothing,i}}{W_{i,\varnothing}}\right) \quad \text{and} \quad J_{ij} - E_i + \mu = \ln\left(\frac{W_{i\cup S_j,S_j}}{W_{S_j,i\cup S_j}}\right). \tag{3.18}$$

Solving the system of equations above determines the pairwise cooperativity of binding a

ligand to site i when site j is occupied expressed in terms of transition rates:

$$J_{i,S_j} = \ln\left(\frac{K_{i,S_j}}{K_{i,\varnothing}}\right), \tag{3.19}$$

where we have used the notation established in Eq. (3.15) for ratios of binding and unbinding rates. We now repeat the same procedure, focusing on a different set of states: the empty receptor, the state S_j with a single ligand bound at site j, and the state $j \cup S_i$, in which two ligands are bound at sites i and j. So that

$$E_j + \mu = \ln\left(\frac{W_{\varnothing,j}}{W_{j,\varnothing}}\right) \quad \text{and} \quad J_{ij} - E_j + \mu = \ln\left(\frac{W_{j\cup S_i,S_i}}{W_{S_i,j\cup S_i}}\right). \tag{3.20}$$

From these, we obtain the pairwise cooperativity associated with binding a ligand to site j when site i is already occupied:

$$J_{j,S_i} = \ln\left(\frac{K_{j,S_i}}{K_{j,\varnothing}}\right). \tag{3.21}$$

The same procedure can be repeated to determine the mapping between rates and higher-order cooperativities as

$$J_{i,S} = \ln\left(\frac{K_{i,S}}{K_{i,\varnothing}}\right) - \sum_{m=1}^{|S|-1} \sum_{\substack{T\subseteq S \\ |T|=m}} J_{i,T}. \tag{3.22}$$

The terms in the summation account for subtracting all lower-order cooperativities (up to order $|S|-1$) corresponding to all subsets that can be formed from the occupied sites in S. For pairwise cooperativities, this energetics-inspired definition is analogous to that proposed by Estrada *et al.* (Eq. (3.16)), but it differs for higher-order cooperativities. At equilibrium, our definition reduces to the standard energy-based definition, with its value becoming independent of the binding order of the sites: $J_{i,S} = J_{j,i\cup(S\setminus j)}$ for all sites $j \in S$.

3.3.2 Dynamics-inspired definition

If cooperativity measures are meant to quantify how ligand binding and unbinding is influenced by the presence of other bound ligands, one could argue that nonequilibrium cooperativity can be captured simply as the ratio between the binding (unbinding) rate in the presence of other ligands and the binding (unbinding) rate in their absence. Building on this idea, we define a dynamics-inspired measure of binding cooperativity

$$J^B_{i,S} = \ln\left(\frac{W_{i\cup S,S}}{W_{i,i\cup\varnothing}}\right) - \sum_{m=1}^{|S|-1} \sum_{\substack{T\subseteq S \\ |T|=m}} J^B_{i,T}, \tag{3.23}$$

and unbinding cooperativity

$$J^U_{i,S} = \ln\left(\frac{W_{S,i\cup S}}{W_{\varnothing,i\cup\varnothing}}\right) - \sum_{m=1}^{|S|-1}\sum_{\substack{T\subseteq S\\|T|=m}} J^U_{i,T}. \tag{3.24}$$

Similar to the energetics-inspired definition, we subtract contributions from lower-order cooperativities to ensure that its value does not inadvertently include lower-order effects. To make contact with the energetics-inspired definition we note that both definitions are related by the simple relation

$$J_{i,S} = J^B_{i,S} - J^U_{i,S}. \tag{3.25}$$

3.3.3 What is the role of higher order cooperativity in nonequilibrium receptor binding models?

Our goal is to determine whether higher-order cooperativities are required to reach maximal sensitivity, as measured by the Hill coefficient. Addressing this requires knowledge of the maximum value that a Hill coefficient can reach in a nonequilibrium binding model with N_B binding sites. In Section 2.8, we showed that for a nonequilibrium two-site receptor the Hill coefficient can reach a value of up to 3. Extending our approach to an arbitrary number of binding sites is difficult, as the perturbations would involve a progressively increasing number of edges. However, Owen *et al.* [22] proved that for a general receptor binding model it holds that

$$\partial_{\ln c}\langle\Theta\rangle \leq (2^{N_B}-1)\langle\Theta\rangle(1-\langle\Theta\rangle). \tag{3.26}$$

So that the maximal nonequilibrium analogue of the Hill coefficient is $2^{N_B}-1$. We then proceed to numerically investigate the role of higher-order cooperativities in the simplest model exhibiting interactions beyond the pairwise level: a receptor with three binding sites. For both the energetics and dynamics-inspired definitions, we search for rate choices that saturate the bound while maintaining all higher-order cooperativities equal to zero.

3.3.3.1 The sampling challenge

Before proceeding, it is necessary to asses if the numerical sampling strategy used in Section 2.8 for the two-binding site model is sufficient to capture maximum sensitivity in the three-binding sites case. As shown in Fig. 3.4(a), uniform sampling in the logarithmic rate space fails to reach the expected maximum sensitivity of $2^3 - 1 = 7$ (Eq. (3.26)), instead yielding values only slightly above 5.

This challenge is addressed by developing a greedy search algorithm with an objective

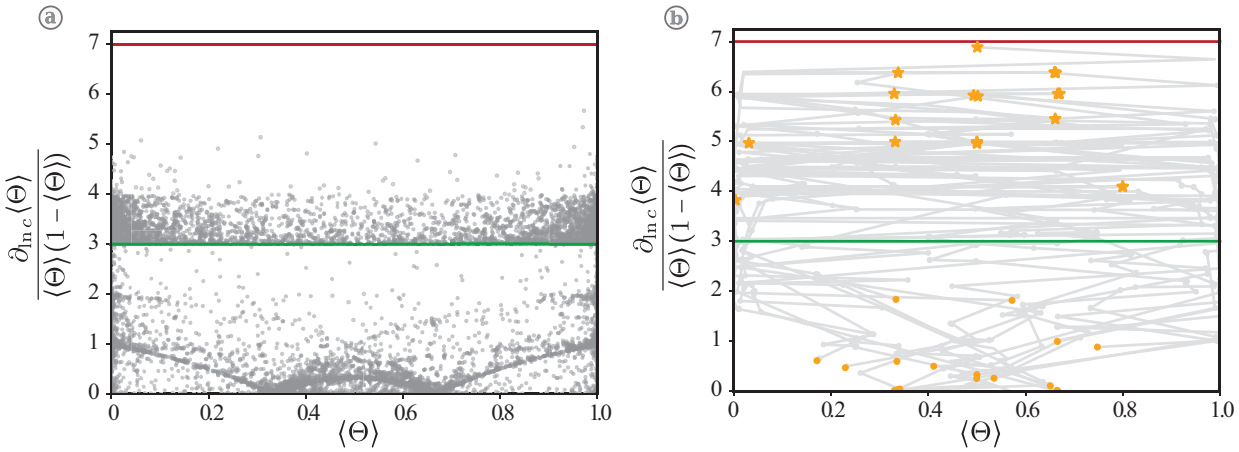


Figure 3.4: (a) For the three-binding site case, the maximum value of $\partial_{\ln\Theta}\langle n\Theta\rangle/\langle\Theta\rangle(1-\langle\Theta\rangle)$ is 7, and the numerical sampling strategy only recovers values slightly above 5. To generate the plot, 5×10^7 sets of rates were sampled with $\ln(W_{S,S'})$ drawn uniformly from the $[-17,17]$ interval. For visualization purposes, only 15,000 samples were plotted. Of these, 10,000 points were randomly selected from the interval $[0,3]$, and another 4,995 points were randomly selected from the interval $[3,7]$. All the five values above 5 were plotted. It should be noted that uniform sampling in log-rate space does not translate into uniform sampling in the space of responses, which is reflected in structured distributions of sampled values in the plots.(b) A greedy search algorithm reaches the maximum sensitivity for a three-binding site receptor model. Initial rate values are chosen at random, orange dots, and only moves that increase the ratio $\partial_{\ln c}\langle\Theta\rangle/\langle\Theta\rangle(1-\langle\Theta\rangle)$ are accepted. Each optimization run is terminated after 10^6 steps, with final values indicated by orange stars. Individual optimization trajectories through the rates state space are shown as gray lines. To generate the figure, 200 independent runs were initiated, of which 20 are shown for visualization purposes.

function defined by $\partial_{\ln c}\langle\Theta\rangle/\langle\Theta\rangle(1-\langle\Theta\rangle)$. In this algorithm, each rate can assume one of five possible values $\{10^{-7},1,10^2,10^4\}$. This choice of rates is motivated by our exploration of optimal topologies in Section 2.5, where a large time-scale difference between rates is necessary to achieve maximum response. An initial set of transitions rates is chosen at random, and at each step a single rate is randomly selected and assigned a different value from the five available options. If the value of the objective function increases, the move is accepted, otherwise, it is rejected. The algorithm is repeated for a fixed number of steps. Using this approach, the expected maximum value of 7 can be reached, as shown in Fig. 3.4(b). Having addressed the sampling challenge, we proceed to explore the role of cooperativity in nonequilibrium binding models.

3.3.3.2 Maximum sensitivity does not require higher order cooperativity

To determine whether higher-order cooperativities are required for maximal sensitivity in a nonequilibrium binding system, it is enough to identify a single case in which the maximum is achieved with all higher-order cooperativities set to zero. Such a counterexample would demonstrate that they are not strictly necessary. We use the optimization algorithm described in Section 3.3.3.1, imposing rate constraints that set all higher-order cooperativities to zero, as defined by both energetics and dynamics-inspired definitions.

Somewhat unexpectedly, for each one of our definitions of cooperativity, a counterexample was identified that reaches the expected maximum value of 7, without any higher-order cooperativities, see Fig. 3.5. It is worth noting, however, that the pairwise cooperativities assume nonzero values.

3.4 Summary

In equilibrium receptor binding models, maximal sensitivity to changes in ligand concentration can be achieved through strong pairwise cooperative interactions alone. To explore whether this principle extends to nonequilibrium systems, we establish two notions of cooperativity. An energetics-inspired definition, based on ratios of transition rates that reduce to the intuitive energy-based definition for cooperativities at equilibrium. And a dynamics-

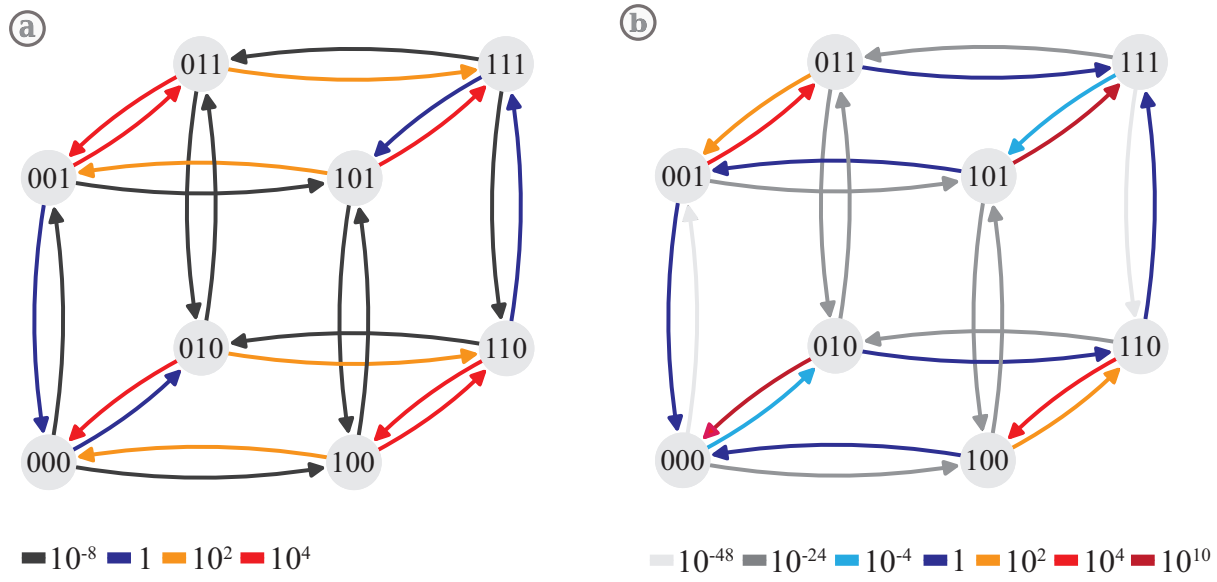


Figure 3.5: Identified counterexamples of three-binding site models that reach the maximum expected sensitivity with no higher-order cooperativity, for the energetics-inspired (a) and dynamics-inspired definition (b). The legend indicates the color coded values for the rates.

inspired definition, based on differences in binding and unbinding rates in the presence versus absence of other bound ligands.

We approached the problem numerically, searching for counterexamples in which maximal sensitivity is achieved while all higher-order cooperativities are set to zero. Remarkably, for each cooperativity definition, we identified one counterexample. Despite the fundamental differences between equilibrium and nonequilibrium dynamics, these results indicate that, similar to equilibrium systems, higher-order cooperativity is not strictly required to achieve maximal sensitivity in nonequilibrium receptor binding models.

CHAPTER 4

Cooperative Antibiotic Response in Bacterial Communities

This Chapter is based on a manuscript under preparation by G. Fernandes Martins *et al.*[1].

4.1 Introduction

The response of bacteria to antibiotic stress is remarkably complex, driven by processes operating across molecular, cellular and population scales. A central feature of this response is antibiotic resistance, which is the capacity of bacteria to survive and grow in otherwise lethal drug concentrations. Resistance can emerge from genetic determinants, conferred from genetic mutations or from horizontal gene transfer. Common resistance mechanisms include efflux pumps, pumps that actively remove the antibiotics from the cell's interior, reduced permeability of the cell membrane to the antibiotic, modification of the drug's target site, or active degradation of the antibiotic. Another form of antibiotic resistance is collective resistance, which remarkably emerges from the protection provided by resistant bacteria to sensitive bacteria that lack intrinsic resistance [60, 61, 62, 63, 64]

Enzymatic drug degradation is a prevalent mechanism of antibiotic resistance, by which enzymes produced by resistant bacteria inactivate antibiotics [65]. This mechanism enables collective resistance through cooperative interactions, allowing sensitive cells to survive due to reduced antibiotic concentrations – resistant bacteria have been shown to fully rescue sensitive counterparts in mixed cultures [8, 9, 10, 11].

To add an extra level of complexity, bacteria do not live in isolation but instead exist in diverse and dynamic communities. These can be broadly categorized either as planktonic communities, composed of free-floating bacteria, or biofilms, composed of surface-attached bacteria. Within biofilms, bacteria are embedded in a self-produced extracellular matrix

[1]Gabriela Fernandes Martins, Keanu Alexander Guardiola-Flores, Luis Zaman, Jordan M. Horowitz, Kelsey M. Hallinen and Kevin Wood. Cooperative antibiotic response in coupled biofilm and planktonic E. faecalis communities. Gabriela Fernandes Martins contributed with the collection of all experimental data discussed in this Chapter, data analysis, model development and writing of the manuscript.

that allows the formation of dense aggregates, often giving rise to highly structured communities [12, 66]. In biofilm communities, bacteria constantly interact, competing for space and nutrients while also cooperating through the sharing of public goods such as the extracellular matrix. Biofilms are considered the most abundant and robust form of bacterial life and are ubiquitous across natural environments, industrial settings, and even the human body [67]. As a result, they pose a serious public health challenge, as they are estimated to account for up to 80% of microbial infections in the body [68].

Biofilms are notorious for frequently displaying greater tolerance to antibiotics than their planktonic counterparts [69]. The extracellular matrix acts as a natural barrier to antibiotics by slowing down or even preventing their penetration. Beyond this, the close proximity between cells promotes high levels of horizontal gene transfer, facilitating the spread of resistance genes within the community. In addition, nutrient gradients within the biofilm give rise to metabolic heterogeneity, producing slow-growing persister cells that can survive antibiotic stress [70, 71, 72, 69, 73].

The prevalence of biofilm-associated infections, together with their increased resistance to traditional antibiotic treatment, makes them an important topic of investigation. More specifically, we ask whether enzymatic-based collective resistance mechanisms are more effective in biofilms when compared to planktonic communities. We focus on understanding the effects of drug-induced cooperative interaction in simultaneously growing, coupled biofilm and planktonic populations. As a model organism, we employ *Enterococcus faecalis*, a non-motile Gram-positive pathogen that readily forms robust biofilms. This opportunistic pathogen is common in hospital acquired infections and frequently exhibits multidrug resistance. In *E. faecalis*, β-lactamase produced by resistant bacteria is localized within the cell [74], with resistant cells operating as antibiotic sinks that provide protection to surrounding bacteria Fig. 4.1. This drug-induced cooperation produces complex spatiotemporal patterns in agar-grown colonies composed of mixed sensitive and resistant bacteria [75, 76]. We show that, albeit unexpectedly, antibiotic driven compositional shifts are the same in both biofilm and planktonic populations. In the biofilm, although antibiotic sinks could be expected to promote spatial structure, correlation analysis reveals that sensitive and resistant cells are not positioned differently relative to one another than in the absence of antibiotics.

4.2 Experimental setup

4.2.1 Bacterial strains

Experiments were performed with *E. faecalis* OG1RF strains with added plasmids encoding fluorescent labels (ampicillin-sensitive:DasherGFP and ampicillin-resistant:RudolphRFP), and a spectinomycin resistance gene. Ampicillin-resistant strains contained a plasmid encoded blaZ gene from the CH19 clinical isolate [77]. The reporter plasmids were previously described and employed in [78, 79, 76, 75]. Brain heart infusion broth (Remel) was used throughout the experiment as the growth media. Selection of the plasmids was enforced by supplementing all media with spectinomycin sulfate (Thermo Fisher Scientific, at 120 µg/mL).

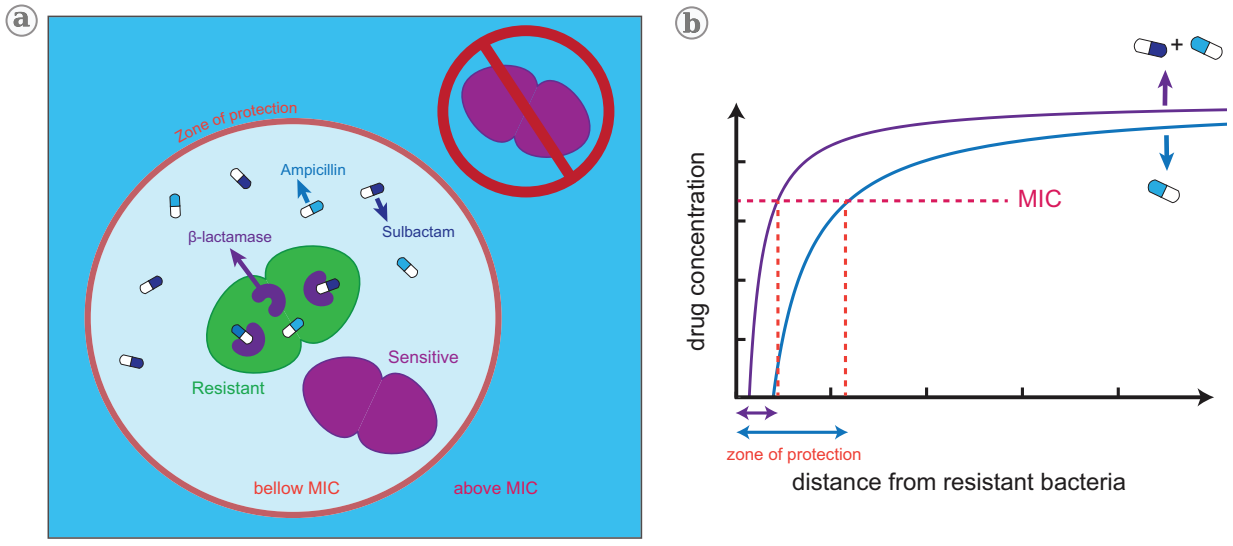


Figure 4.1: *E. faecalis* exhibits cooperative resistance to β-lactam antibiotics. (a) Ampicillin-resistant bacteria, shown in green, produce β-lactamase, an enzyme that inactivates ampicillin through hydrolysis. Although β-lactamases remain cell-associated, resistant bacteria effectively act as antibiotic sinks by degrading the drug. If the antibiotic concentration in the vicinity of a resistant cell falls below the MIC, sensitive cells, in magenta, can grow within this zone of protection. Sulbactam is a β-lactam drug commonly used in combination with ampicillin in clinical settings. Sulbactam has no toxic effects, however it binds irreversibly to β-lactamases, acting as a competitive inhibitor to ampicillin and decreasing the ability of resistant bacteria to degrade the drug. (b) The drug concentration profile is calculated by solving the 1D diffusion equation for a single resistant bacteria acting as a sink, with a fixed drug concentration at infinity. The zone of protection is defined as the distance from a resistant cell for which the drug concentration is below the MIC. The addition of sulbactam effectively decreases the zone of protection.

4.2.2 Biofilm growth

Overnight cultures were prepared by inoculating bacteria directly from frozen stocks in media and grown at 32°C on an orbital shaker at 150 RPM. After 17 hours, cultures were diluted at a 1:4 ratio to enable for accurate optical density (OD_{600}) measurements. Both cultures were brought to an OD_{600} of 0.51. Mixtures with a target initial percentage of resistant bacteria equal to p were prepared by mixing $2 \times p$ µL of the resistant culture and $2 \times (100 - p)$ µL of the sensitive culture in 10 mL of media. For experiments starting at an OD of 0.001, an additional 1:10 dilution was performed. A total of 2.7 mL of each mixture was transferred to 35 mm glass bottom microscope dishes (Cellvis, D35-20-1-N) and incubated at 37°. Samples were kept stationary during the incubation period. After 30 minutes, 0.3 mL of media supplemented with antibiotics was added to each dish. The antibiotics used include ampicillin sodium salt (Sigma-Aldrich) and sulbactam (Cayman Chemical). To achieve a target antibiotic concentration of c in 3 mL, the media supplemented with antibiotics was prepared at a concentration equal to $10 \times c$. Samples were then incubated at 37°C for 24 hours.

4.2.3 Data collection and image analysis

After 24 hrs the glass bottom dishes containing the biofilms were removed to room temperature and imaged separately on a Zeiss LSM 700 inverted confocal microscope with a 40x oil objective and a pinhole of 1.2 µm. Five different regions of dimensions 80 µm x 80 µm x 60 µm were imaged for each biofilm. Vertical planes were separated by 2.5 µm and selected to allow for imaging of the biofilm from its bottom layer to its upper surface at every point. The composition of the planktonic population was measured by imaging three independent 20 µL samples on a glass slide. After image processing using Fiji [80], data analysis was performed in two steps, with pixel classification executed with scientific software ilastik [81] followed by bacterial segmentation using a custom MATLAB script. Each experiment was repeated on three separate days. The error bars reported throughout this work capture both the variability across different positions within the biofilm and the variation between independent experimental replicas.

4.3 Resistance spreads through a population inversion effect in biofilm and planktonic populations equally

To investigate the role of antibiotic-induced cooperativity in shaping bacterial response to antibiotic stress, we study coupled biofilm and planktonic populations consisting of mixed

ampicillin-sensitive and ampicillin-resistant *E. faecalis* bacteria. Both strains constitutively express fluorescent markers - green for sensitive and magenta for resistant - allowing for clear distinction between the two cell types [78]. Resistance is conferred to ampicillin-resistant bacteria by a plasmid-encoded β-lactamase of clinical origin [79]. For each experiment, mixtures of sensitive and resistant cells, prepared at a specific initial ratio and cellular density, were grown in liquid media supplemented with a defined concentration of antibiotics. After 24 hrs of undisturbed incubation at 37°, bacteria form two distinct populations, a surface attached biofilm and a free-floating planktonic community. The final composition and characteristics of both populations were measured via confocal fluorescent microscopy Fig. 4.2.

The presence of resistant strains in bacterial populations has been observed to protect non-β-lactamase producers from otherwise lethal ampicillin concentrations in diverse scenarios [82, 83, 76, 75, 8, 84, 9, 73]. This phenomena is evident in our biofilm microscopy data Fig. 4.2, where, despite population-wide compositional shifts, sensitive bacteria (magenta) are always present at super inhibitory ampicillin and sulbactam concentrations. We quantify the fraction of resistant bacteria in the final population as a function of its initial value for both biofilm and planktonic communities, revealing a non-monotonic dependency for all ampicillin concentrations tested, Fig. 4.4. We refer to this as a population inversion effect, where, below a threshold value, the final fraction of resistant cells is greater than its initial value, leading to the spread of resistance through the population. This effect results from the interplay between two bacterial social interactions, competition for resources and cooperative protection against antibiotics. When the initial number of resistant bacteria is low, cross-protection against antibiotics is limited, and sensitive bacteria are unable to survive. On the other hand, when the initial number of resistant bacteria is above a certain threshold, sensitive cells are protected from the antibiotic and compete with the resistant cells for resources, containing the spread of resistance. Naturally, an increase in the initial drug concentration amplifies this effect, whereas an increase in the initial cell density attenuates it.

Studies in planktonic cultures of *Escherichia coli* have reported results of a similar nature than ours [8, 73], suggesting this resistance spread effect to be of broad application. Differently than in *E. faecalis*, in *E. coli* β-lactamase is found extracellularly, naturally altering the mechanistic details of the cooperative interaction [85]. Previous work also suggests that differently from our results, the populational shifts caused by antibiotic stress are quantitatively distinct in *E. coli* planktonic and biofilm cultures grown separately [84]. This disparity could reflect differences in the enzyme location mechanism or indicate that the simultaneous formation of the two populations during antibiotic stress produces distinct effects than when

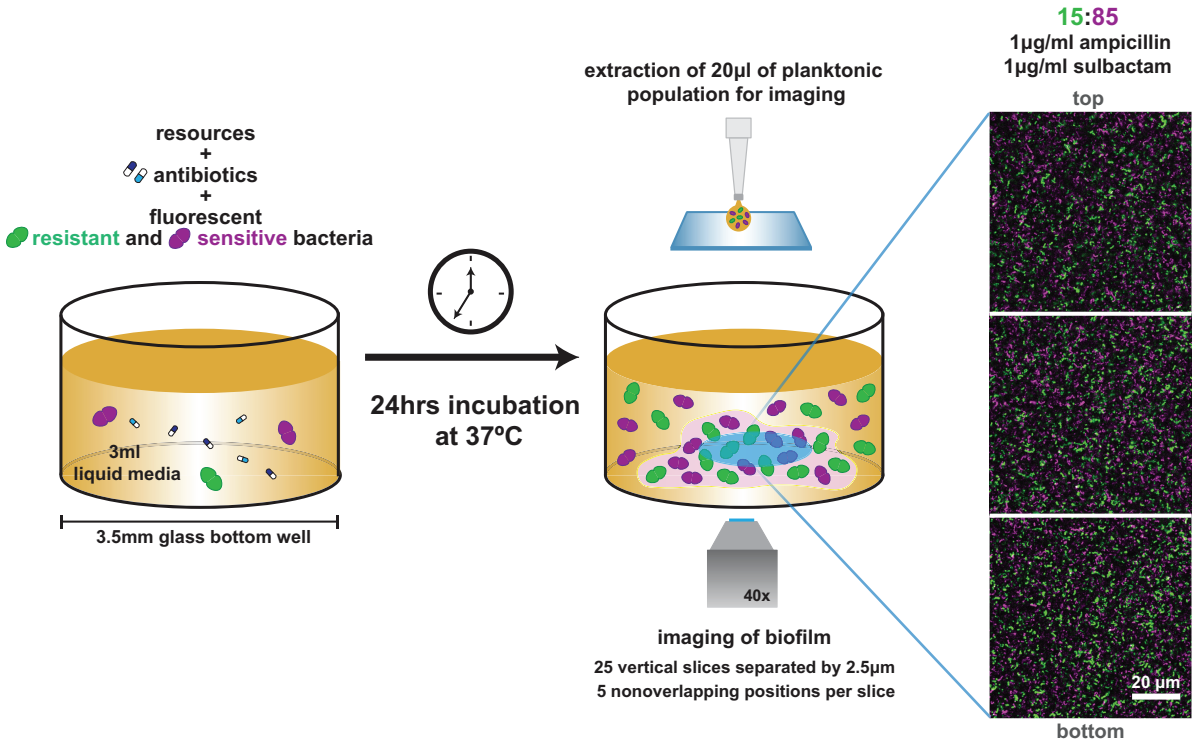


Figure 4.2: *E. faecalis* populations growing in the presence of ampicillin and sulbactam undergo significant compositional changes that depend on drug concentration and initial population composition. Diagram illustrating the experiment. A mixture of florescent ampicillin-sensitive and ampicillin-resistant *E. faecalis* bacteria, prepared at a defined density and ratio, is added to a glass-bottom well containing liquid growth media supplemented with drugs. After a 24 hour incubation period at 37 the biofilm is imaged directly in the glass-bottom well using confocal fluorescence microscopy. During incubation the well is kept undisturbed with no liquid media or antibiotics replenishing. The biofilm is imaged though its full thickness along the vertical axis by capturing 25 optical slices of dimensions 80 µm x 80 µm separated by 2.5 µm. A 20 µL sample of the planktonic population is extracted and mounted on a glass slide for imaging using confocal fluorescent microscopy.

the two populations are studied separately.

4.4 β-lactamase inhibition enhances resistance spread

To increase efficacy against strains exhibiting resistance mechanisms, β-lactam antibiotics are commonly administered in conjunction with β-lactamase inhibitors such as sulbactam. Sulbactam has little intrinsic antibacterial activity but binds irreversibly to β-lactamases, thus protecting ampicillin from enzymatic degradation and restoring its antibacterial effectiveness [86, 87, 88, 89]. Since resistant cells mediate protection of sensitive cells through

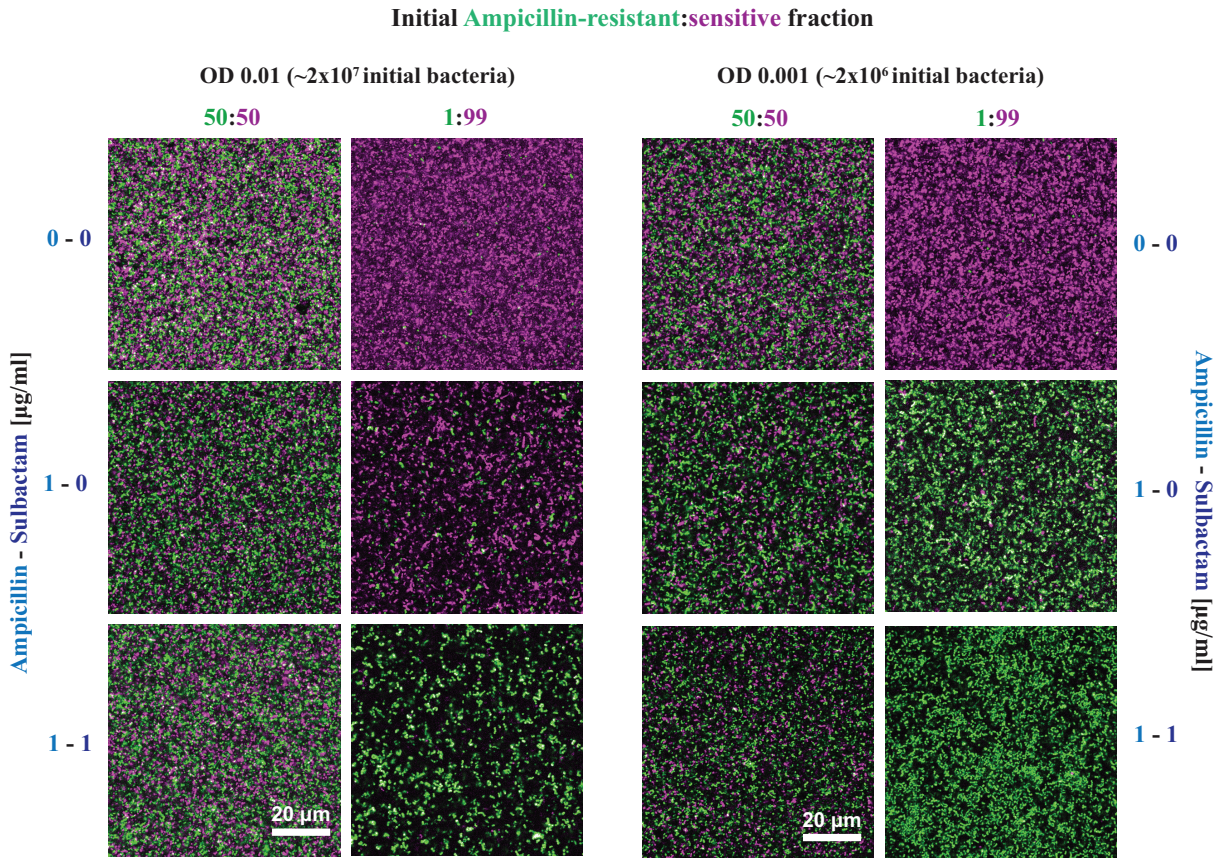


Figure 4.3: Representative images (densest slice) of mixed ampicillin-resistant (green) and ampicillin-sensitive (magenta) biofilms after the incubation period. Initial bacterial density, initial resistant:sensitive ratio, as well as ampicillin and sulbactam concentrations were varied to examine effects on final population composition. All panels are shown at the same scale.

β-lactamase activity, the cooperative dynamics between the two strains are expected to be altered by sulbactam.

As expected, sulbactam by itself does not alter the population composition relative to the drug-free case, Fig. 4.5 (panels a and d). However, when combined with ampicillin, the final fraction of resistant cells is consistently higher than with ampicillin alone Fig. 4.5 (panels b and e). This can be understood through the interplay of cooperative and competitive interactions. Upon initial antibiotic exposure, resistant cells degrade ampicillin less efficiently, leaving sensitive cells partially unprotected. The early loss of sensitive cells reduces competition for nutrients, allowing resistant cells to take over the population. As observed in the ampicillin-only condition, biofilm and planktonic populations also exhibit the same composition Fig. 4.5 (panels c and f).

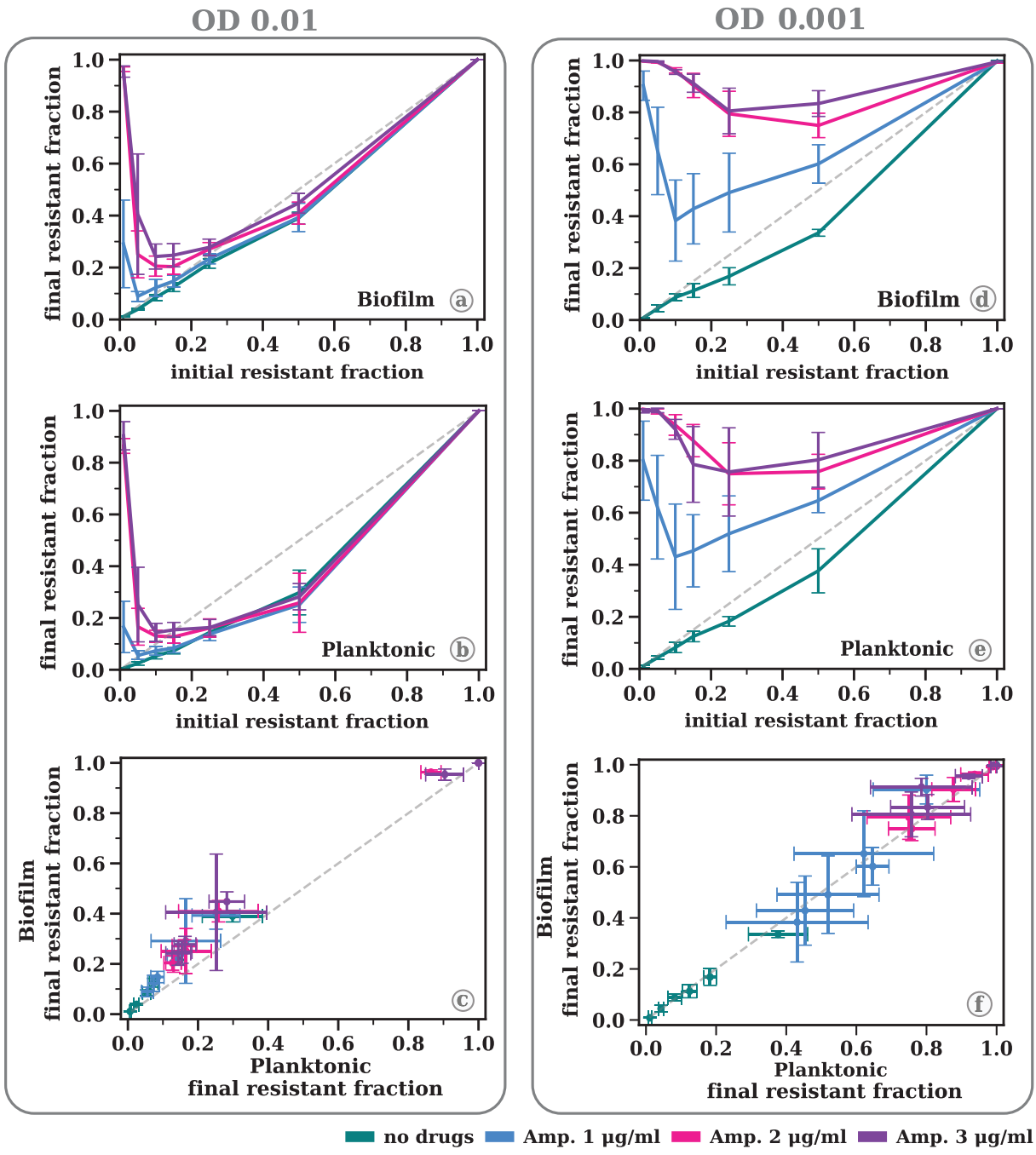


Figure 4.4: Spread of resistance by a population inversion effect as demonstrated by measurements of the final resistant fraction of bacteria as a function of the initial resistant fraction in the biofilm (panels a and d) and in the planktonic (panels b and e) populations. The non-monotonic dependence between final and initial resistant fractions is modulated by the initial number of bacteria in the system (for biofilm data compare panels a and d, for planktonic data compare panels b and e) with higher resistant fractions observed at the lower OD value of 0.001. Both biofilm and planktonic populations have the same final composition as seen by visualizing the final resistant fraction in the biofilm in terms of the final resistant fraction in the planktonic (panels c and f).

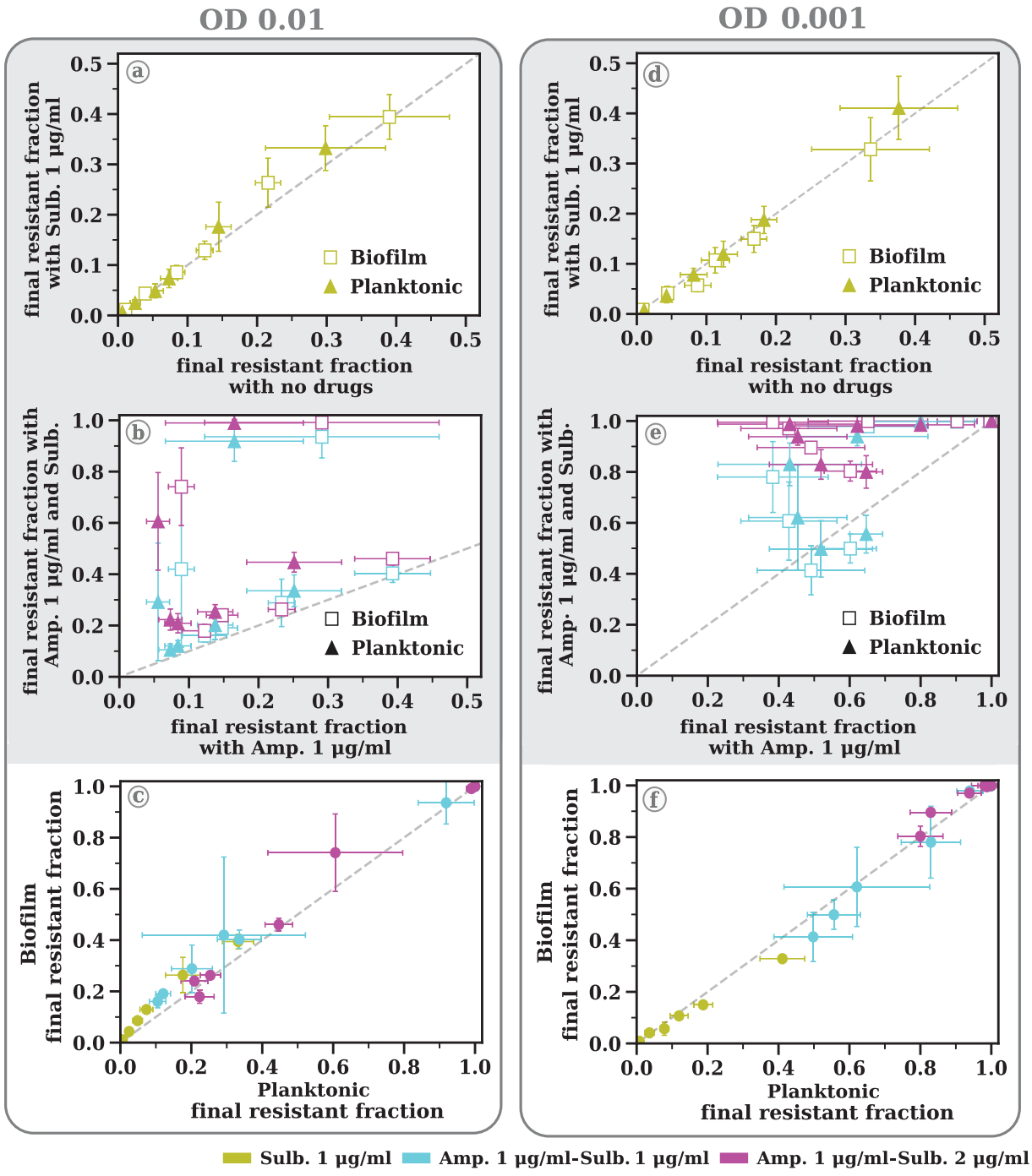


Figure 4.5: The combined use of ampicillin and sulbactam exacerbates the spread of resistance in the biofilm and planktonic populations. Sulbactam has no intrinsic toxic effects to the cells, when used by itself final resistant fractions are the same as for the no drugs case scenario for both OD 0.01 and 0.001 (panels a and d). Ampicillin was used in combination with sulbactam at two distinct concentration values, Amp.1 µm-Sulb.1 µm (cyan) and Amp.1 µm-Sulb.2 µm (purple). For both OD 0.01 (panel b) and OD 0.001 (e) the resulting final fraction is higher than the final resistant fraction with only Ampicillin at 1 µm. Similarly to the only Ampicillin cases, both biofilm and planktonic populations have the same final composition (panels c and f).

4.5 Biofilms are structurally amorphous as revealed by correlation analysis

So far our analysis has focused on the characteristics of the global population of the planktonic and biofilm communities. However, biofilms often exhibit well-defined spatial structure that can be altered in response to antibiotic treatment [90]. The nature of the drug-induced cooperative interaction suggests that biofilms formed under antibiotic stress may undergo spatial restructuring, altering relative distances between β-lactamase producers and non-producers. We use a metric similar to a cumulative radial distribution function to study the spatial distribution of resistant cells in respect to sensitive cells. The quantification of this metric, which we refer simply as correlation, requires two datasets. One contains the extracted values of the centroid for each cell in the biofilm and the other is a randomized dataset that contains the same number of cells, but with centroid values assigned at random. The correlation $c(r)$ is then equal to the ratio between the average number of resistant cells within a distance r of a sensitive cell in the original dataset and the same quantity calculated in the randomized dataset [91, 92, 93]. We denote the centroids of sensitive and resistant cells in the original dataset as $\{\vec{r}_S\}$ and $\{\vec{r}_R\}$, and in the randomized dataset as $\{\vec{q}_S\}$ and $\{\vec{q}_R\}$. The correlation is then calculated as

$$c(r) = \frac{\sum_{\{\vec{r}_S\}} \sum_{\{\vec{r}_R\}} H(r - |\vec{r}_S - \vec{r}_R|)}{\sum_{\{\vec{q}_S\}} \sum_{\{\vec{q}_R\}} H(r - |\vec{q}_S - \vec{q}_R|)}, \tag{4.1}$$

where $H(x)$ denotes the Heaviside step function, defined as $H(x) = 1$ for $x > 0$ and $H(x) = 0$ otherwise. When equal to one, this metric indicates that cells are positioned in the biofilm at random. Values below one indicate fewer resistant cells in the neighborhood of sensitive cells than expected in a random spatial arrangement, whereas values greater than one indicate more resistant cells.

For distances larger than 1 µm, the correlation is equal to one, and drops below one for shorter distances. This observation extends to biofilms formed with and without antibiotic stress, for all values of drug concentrations and initial resistant fractions, see Fig. 4.6. As the typical cell size is of the order of 1 µm, values below one are expected within this distance. This arises as an artifact of the randomization procedure, in which centroids are placed without enforcing spatial exclusion, that is, without accounting for the finite size of the cells. For distances larger than 1 µm, correlation values equal to one indicate that the biofilm is structurally amorphous. When rationalized in conjunction with the observation that planktonic and biofilm communities undergo the same population shift, this result suggests that the drug-induced cooperative interaction does not induce structuring in *E. faecalis*

bacterial communities.

4.6 Modeling

The following Sections introduce two different models and analyze their relevance to the experimental observations. In particular, we assume that the system is at steady-state and evaluate whether each model can capture the non-monotonic relationship between the initial and final fractions of resistant bacteria observed in Figs. 4.4 and 4.5.

4.6.1 The minimal model

Experimental data show that planktonic and biofilm populations have identical final compositions, with no spatial structuring in the biofilm. These observations motivate a minimal, well-mixed model without a spatial component, capable of describing the biofilm composition. One could imagine that the simplest well-mixed model has both sensitive and resistant bacteria growing following a logistic growth rule with carrying capacity C and dying to emulate the presence of the antibiotics. To account for the observed fitness differences, sensitive and resistant bacteria have distinct growth rates, b_S and b_R (Fig. 4.4). To capture the larger tolerance to antibiotics of resistant bacteria, different death rates are also assigned, d_S and d_R. The cooperative protection provided by resistant bacteria can be expressed as a multiplicative term on the sensitive population's death rate, such that the death rate decreases as the resistant population increases. Under said assumptions, the resulting dynamics of resistant, R, and sensitive, S bacteria are then described by,

$$\frac{dS}{dt} = b_S S\left(1 - \frac{R+S}{C}\right) - d_S S\frac{K^n}{K^n + R^n}, \tag{4.2}$$

$$\frac{dR}{dt} = b_R R\left(1 - \frac{R+S}{C}\right) - d_R R. \tag{4.3}$$

The system's carrying capacity quantifies the maximum total population that can be sustained by the environment. The functional form, K^n/K^n+R^n, reflects the presence of the cooperative interaction: in the absence of resistant bacteria the sensitive death rate is unaffected, but as the number of resistant bacteria increases, the effective death rate decreases. K sets the number of resistant bacteria required to lower the death rate of sensitive cells to half its original value. n dictates how steeply the death rate drops with increasing numbers of resistant bacteria. Other functions with similar properties could be also considered, as long as they do not produce negative values for the effective death rate.

The model's steady-state is determined by numerically evaluating the intersection be-

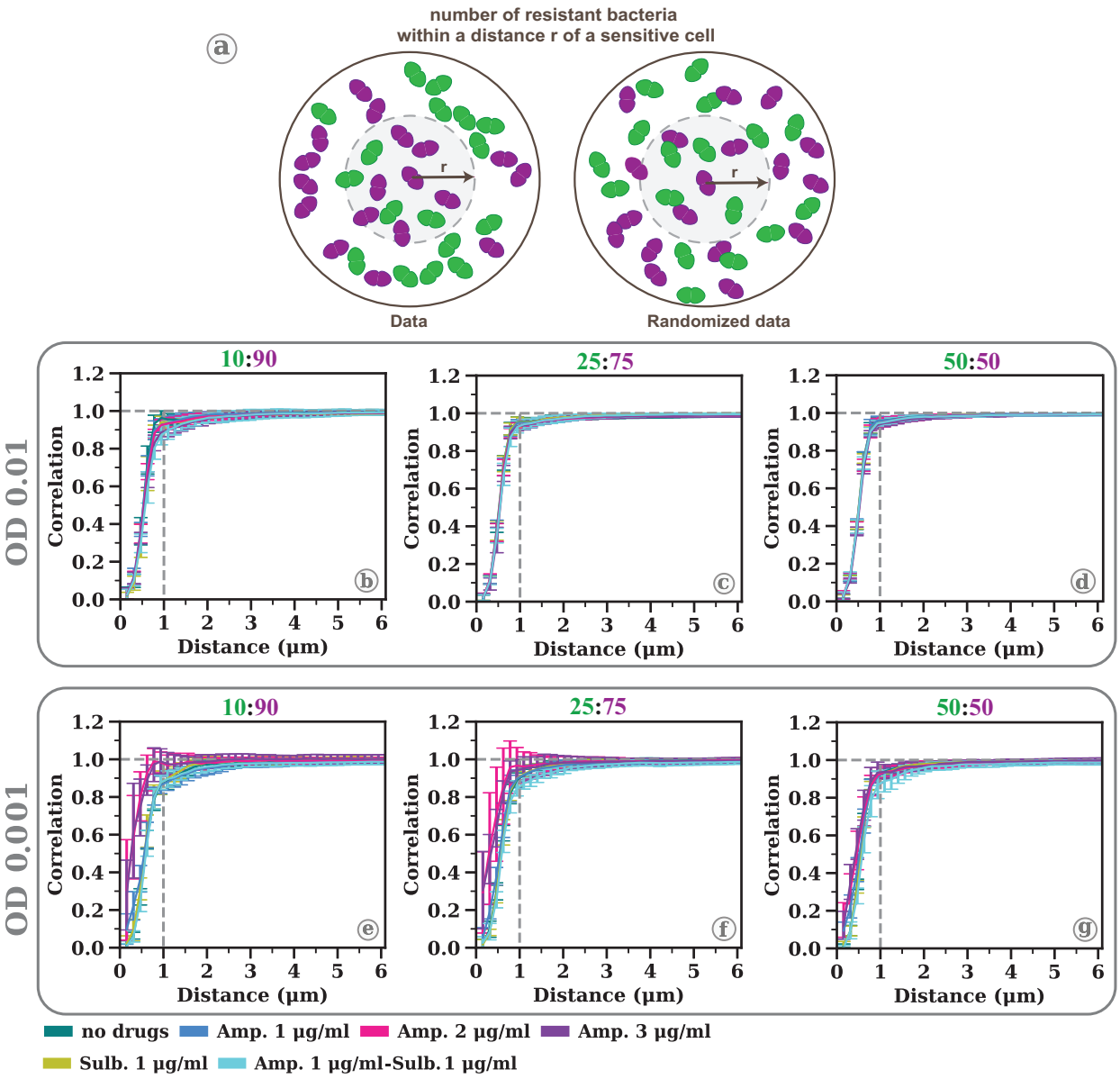


Figure 4.6: Correlation analysis reveals that the biofilm does not exhibit spatial structure. (a) The metric used to quantify structure is analogous to a cumulative radial distribution function, quantifying differences between the relative positions of resistant bacteria in respect to sensitive bacteria in the data and in its randomized version. Values equal to one indicate that the biofilm lacks spatial structure, as the relative positions are the same as in a completely random scenario. Values above one indicate an increase in the number of resistant cells close to sensitive cells in relation to the random scenario, and values below one indicate a decrease. (b) For all initial resistant fractions and values of drug concentrations, the correlation metric has the same qualitative behavior with small quantitative shifts.

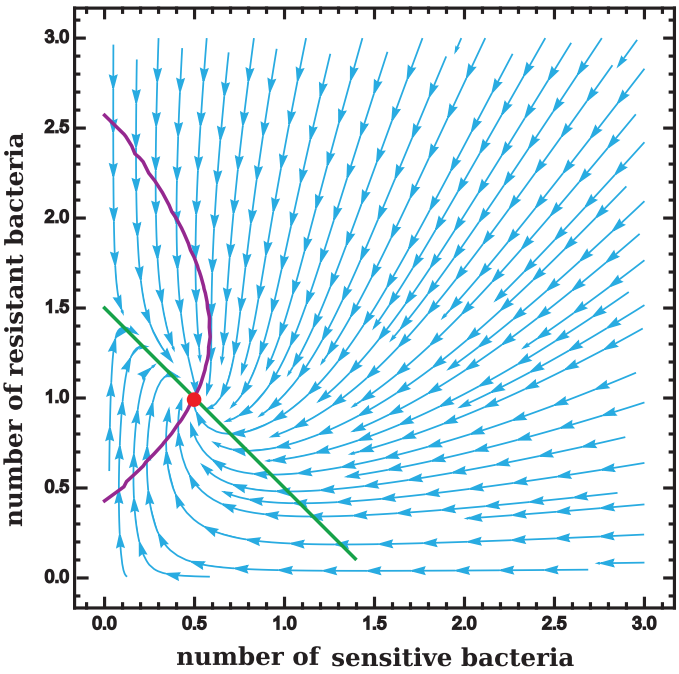


Figure 4.7: Phase plane of the dynamical system defined by Eqs. 4.2 and 4.3. The intersection between the nullcline of Eq. 4.2, in magenta, and Eq. 4.3, in green, defines the single fixed point of the system, in red. The values of the parameters used to generate this plot are $b_S = b_R = 1 = d_S$, $d_R = 0.5$, $C = 3$, $K = 1$ and $n = 2$.

tween the nullclines of Eq. (4.2) and Eq. (4.3). For any realistic choice of parameters[2], the system exhibits a single fixed point where both sensitive and resistant bacteria coexist. At this point, a fundamental limitation of this model becomes apparent. Experimental data, Figs. 4.4 and 4.5, show that each initial resistant fraction leads to distinct final resistant fraction values. In contrast, the model predicts that all initial resistant fractions result in the same steady-state value of the final resistant fraction. This inconsistency suggests that the cooperative interaction should be incorporated indirectly by explicitly modeling the drug dynamics.

4.6.2 The model with drug dynamics

To overcome the limitations of the minimal model, we develop a framework that explicitly accounts for the drug dynamics, Fig. 4.8. While the intracellular regulatory dynamics during antibiotic exposure is relevant to explain divergent cell fates in certain scenarios [94, 95], we

[2]For a coexistence fixed point to exist, d_R must be larger than zero and smaller than b_R. d_S must also lie below an upper bound that depends on the values of all other parameters. This bound is always larger than d_R, ensuring consistency with the model assumptions.

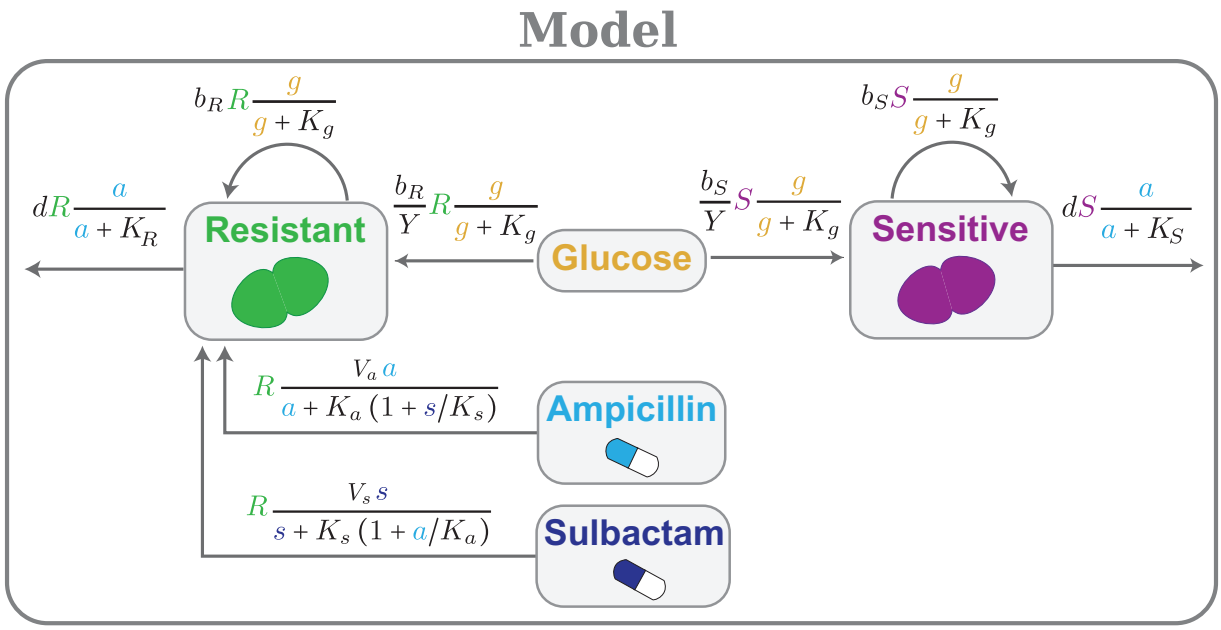


Figure 4.8: Diagrammatic representation of the well-mixed model used to reproduce the observed spread of resistance within the biofilm. Sensitive and resistant cells consume glucose and grow at a rate that scales hyperbolically with its concentration. Ampicillin causes cell death, with resistant cells requiring substantially higher drug concentrations to reach half-maximal death rates compared with sensitive cells. Resistant cells produce intracellular β-lactamase, which degrades ampicillin. Sulbactam, while not toxic to cells, binds β-lactamase and competitively inhibits ampicillin degradation, thereby reducing its efficacy.

assume that such details are not necessary to account for the observed phenomena. We then assume that each resistant cell contains the same number of β-lactamase enzymes, which remains constant over time and ensures the dynamics of drug degradation depends linearly on the number of resistant bacteria.

A second modification to the minimal model is required. In that model, the growth dynamics is dictated by a carrying capacity term that constrains the total population at steady-state. However, even a qualitative examination of Fig. 4.3 suggests that this constraint is not consistent with the experimental observations. This shortcoming can be addressed by introducing bacterial growth dynamics that depend on the concentration of available resources. Then the model considered in this section is centered on three core processes: resource limited cell birth, drug induced cell death and drug degradation by resistant cells, Fig. 4.8.

We describe growth using the empirical Monod model [96, 97, 98], with glucose as the limiting resource. In this model, bacteria of a given strain have the same resource dependent growth rate $^{bg}/_{g+K_g}$, where g is the glucose concentration, b is the maximum growth rate, and K_g is the Monod constant. To incorporate the fitness cost of antibiotic resistance, sensitive

and resistant cells are assumed to have distinct maximum growth rates, b_S and b_R. Both strains undergo only ampicillin-dependent cell death, as sulbactam showed no toxicity at the concentrations tested. We assume the dose-response function takes the format of a Hill function with Hill coefficient equal to one [99]. The death rate of cells is then equal to $^{da}/_{a+K}$, with a being the ampicillin concentration, d the maximum death rate, and K the antibiotic concentration at which the death rate is half of its maximum. As sensitive cells are substantially more susceptible to ampicillin than resistant cells, sensitive and resistant strains reach half of the maximum death rate at different ampicillin concentrations, denoted by K_S and K_R. The resulting dynamics of the sensitive, S, and resistant, R, populations are described by

$$\frac{dS}{dt} = S\frac{b_S g}{g + K_g} - S\frac{da}{a + K_S}, \tag{4.4}$$

$$\frac{dR}{dt} = R\frac{b_R g}{g + K_g} - R\frac{da}{a + K_R}. \tag{4.5}$$

Throughout the experiment, the concentration of glucose, ampicillin and sulbactam only decreases, as cells consume resources and intracellular β-lactamase degrades the antibiotics. The dynamics of glucose depletion is

$$\frac{dg}{dt} = -\frac{1}{Y}\left(b_S S + b_R R\right)\frac{g}{g + K_g}, \tag{4.6}$$

where Y denotes the cell yield per unit of glucose consumed. We assume the binding rate between the drugs and β-lactamase follows Michaelis-Menten kinetics with competitive inhibition [100], as both ampicillin and sulbactam bind to the same substrate. The dynamics of ampicillin is then phenomenologically modeled as

$$\frac{da}{dt} = -R\frac{V_a a}{a + K_a\left(1 + s/K_s\right)}, \tag{4.7}$$

where the degradation rate is proportional to a maximum rate per cell, V_a, and scales with the total number of resistant cells. The presence of sulbactam increases the effective Michaelis constant, K_a, by a factor of $1 + {}^{s}/_{K_s}$, where s is the sulbactam concentration. An analogous dynamics holds for the degradation of sulbactam

$$\frac{ds}{dt} = -R\frac{V_s s}{s + K_s\left(1 + a/K_a\right)}, \tag{4.8}$$

with a sulbactam specific maximum degradation rate per cell, V_s, and an effective Michaelis constant, K_s, increased by a factor of $1 + {}^{a}/_{K_a}$.

The steady-state of the model is reached when glucose and drugs in the system are fully depleted. Solving Eqs. (4.4) to (4.8) is only possible using numerical methods. To simplify the numerical analysis, the variables and parameters of the model are nondimensionalized to remove redundant degrees of freedom. After nondimensionalization, the model is characterized by six parameters: $\tilde{b}$, $\tilde{d}$, $\tilde{K}_{SR}$, $\tilde{K}_{as}$, $\tilde{V}$, and $\tilde{Y}$. Rates are measured in units of the maximum birth rate of resistant cells, b_R. Ampicillin concentration is measured in units of K_S, and glucose concentration in units of K_g. Thus $\tilde{b} := {}^{b_S}/_{b_R}$ quantifies the fitness differences between the strains and $d := {}^{d}/_{b_R}$ measures the difference between maximum death and birth rates. $\tilde{K}_{SR} := {}^{K_R}/_{K_S}$ quantifies the difference in values of lethal antibiotic concentrations for sensitive and resistant cells, and $\tilde{K}_{as} := {}^{K_s}/_{K_a}$ the ratio of Monod constants for sulbactam and ampicillin. Only one parameter, $\tilde{V} := {}^{V_s K_a}/_{V_a K_s}$, is necessary to characterize the drug degradation rates. It then follows that the dimensionless version of the yield coefficient has the format $\tilde{Y} := {}^{Y K_g V_a}/_{K_S b_R}$. Then the nondimensional version of the equations dictating the dynamics are,

$$\frac{d\tilde{S}}{d\tau} = \tilde{S}\frac{\tilde{b}\tilde{g}}{\tilde{g}+1} - \tilde{S}\frac{\tilde{d}\tilde{a}}{\tilde{a}+1}, \tag{4.9}$$

$$\frac{d\tilde{R}}{d\tau} = \tilde{R}\frac{\tilde{g}}{\tilde{g}+1} - \tilde{R}\frac{\tilde{d}\tilde{a}}{\tilde{a}+\tilde{K}_{SR}}, \tag{4.10}$$

$$\frac{d\tilde{g}}{d\tau} = -1/\tilde{Y}\left(\tilde{b}\tilde{S}+\tilde{R}\right)\frac{\tilde{g}}{\tilde{g}+1}, \tag{4.11}$$

$$\frac{d\tilde{a}}{d\tau} = -\tilde{R}\frac{\tilde{a}}{\tilde{a}+\tilde{K}_{as}+\tilde{s}}, \tag{4.12}$$

$$\frac{d\tilde{s}}{d\tau} = -\tilde{R}\frac{\tilde{V}\tilde{s}}{\tilde{s}+\tilde{K}_{as}+\tilde{a}}, \tag{4.13}$$

where $\tau := {}^{t}/_{b_R}$, $\tilde{a} := {}^{a}/_{K_S}$, and $\tilde{g} := {}^{g}/_{K_g}$. For consistency, the remaining variables are rescaled as $\tilde{R} := {}^{R V_a}/_{b_R K_S}$, $\tilde{S} := {}^{S V_a}/_{b_R K_S}$, and $\tilde{s} := {}^{s K_a}/_{K_s K_S}$[3].

The model predicts the non-monotonic behavior of the final fraction of resistant cells for different values of drug concentrations and initial bacterial densities, Fig. 4.10. The values of the six dimensionless parameters and the initial conditions are determined through fitting to a subset of the OD 0.001 data. We do not mean the fitted parameters to carry accurate

[3]We can check if our analysis is consistent with the Buckingham π Theorem. The theorem states that an equation with a total of m variables and parameters can be rewritten in terms of p nondimensional variables and parameters, with $p = m - n$. n is the total number of physical dimensions involved. In this case, the original set of equations contains $m = 18$ variables (R, S, g, a, s, as well as time) and parameters (b_S, b_R, d_R, d_S, K_g, K_S, K_R, Y, V_a, V_s, K_a, K_s). The total number of physical dimensions is equal to 5, which are time, the number of bacteria, and the glucose, ampicillin and sulbactam concentrations. This leaves us with the prediction that the nondimensional version of our system should contain 13 variables and parameters, which is precisely what we obtain.

biological interpretation but instead serve to demonstrate that this simple phenomenological model reproduces the experimental observations. The fitting procedure is split in three steps. First, the number of sensitive bacteria and the final fraction of resistant bacteria in the no-drug condition were used to estimate parameters $\tilde{b}$ and $\tilde{Y}$, as well as the initial total cell number and glucose concentration, Fig. 4.11. Next, the final resistant fraction data for the lowest ampicillin concentration (Amp.1 µg/mL) is used to determine the values of $\tilde{d}$, $\tilde{K}_{SR}$, $\tilde{K}_{as}$, along with the initial ampicillin concentration. At last, the final resistant fraction data for the highest sulbactam concentration (Amp.1 µg/mL – Sulb.1 µg/mL) is used to fit for the value of $\tilde{V}$. The fitted values are listed in Table 4.1: as expected, a value of $\tilde{b} > 1$ represents the fitness difference between sensitive and resistant bacteria, while $\tilde{K}_{SR} > 1$ represents the decreased susceptibility of resistant bacteria to the drug.

Using the fitted nondimensionalized parameters and initial conditions we numerically evaluate the system dynamics to gain intuition about its behavior, see Fig. 4.9. As the bacterial populations grow, the glucose concentration decreases, while ampicillin and sulbactam are degraded at different rates. The system reaches a steady-state once glucose and both drug concentrations reach zero, at which point birth and death processes can no longer occur. The initial fraction of resistant bacteria influences both the time required to reach stationary dynamics and the final resistant fraction.

Using the fitted initial conditions and parameter values, the model is challenged by evaluating its predictions on the subset of data not used for fitting. Specifically, we compare measurements at higher ampicillin concentrations (Amp.2 µg/mL and Amp.3 µg/mL) with model predictions generated using twofold and threefold increases of the fitted initial ampicillin concentration. For both values of initial cell densities the model accurately predicts the experimental observations, Fig. 4.10, panels a and c. We next compare measurements at non-zero sulbactam concentrations (Sulb.2 µg/mL, Amp.1 µg/mL – Sulb.1 µg/mL and Amp.1 µg/mL – Sulb.1 µg/mL) with model predictions generated using a baseline sulbactam concentration equal to the fitted ampicillin concentration. Although the model predicts an increase in the final fraction of resistant cells relative to the cases with ampicillin alone, it does not quantitatively capture the observed values. A plausible explanation is that, when used in combination with ampicillin, sulbactam effectively increases the maximum cell death rate.

4.7 Summary

Bacteria inhabit rich communities shaped by cell-cell interactions, giving rise to emergent behaviors such as collective antibiotic resistance, a phenomenon of growing relevance in the face of declining antibiotic effectiveness. This phenomena is observed in *Enterococcus*

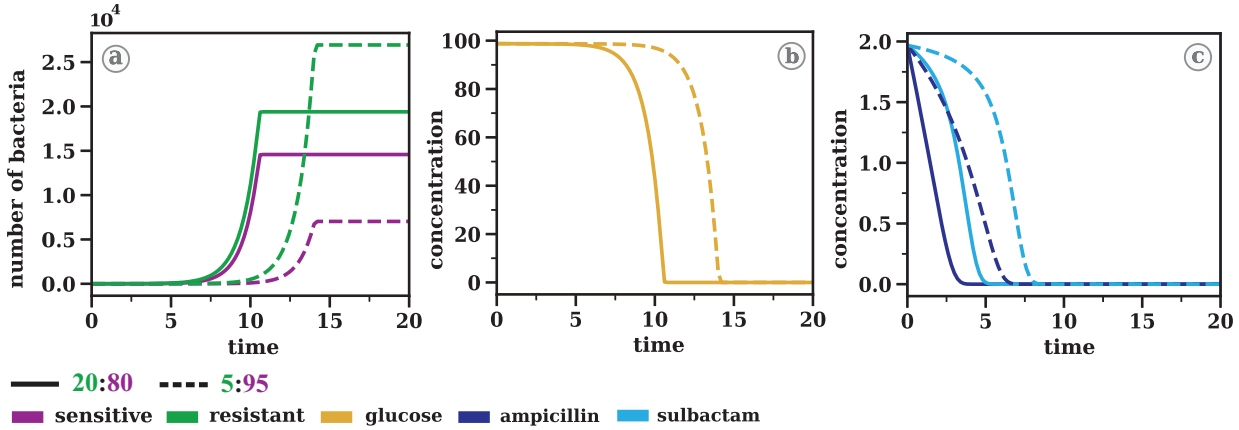


Figure 4.9: Time dynamics of the model variables for two different initial resistant fractions, 0.2 and 0.05. Ampicillin and sulbactam are continuously degraded as the population of resistant bacteria increases. Once both drug concentrations reach zero, bacterial death stops and the population only grows. As bacteria grow, the glucose concentration also decreases and once it reaches zero, growth ceases. When both glucose and drug concentrations reach zero, the system reaches steady-state. The dynamics are generated using parameters obtained from the fitting procedure, with values specified in Fig. 4.10.

Parameters and initial conditions	**Fitted values**
$\tilde{S}_0 + \tilde{R}_0$	10
$\tilde{g}_0$	98.75
$\tilde{a}_0$	1.96
$\tilde{b}$	1.07
$\tilde{d}$	2.73
$\tilde{K}_{SR}$	5.11
$\tilde{K}_{as}$	2.18
$\tilde{V}$	0.16
$1/\tilde{Y}$	0.003

Table 4.1: Fitted values of the nondimensionalized parameters and initial conditions of the model.

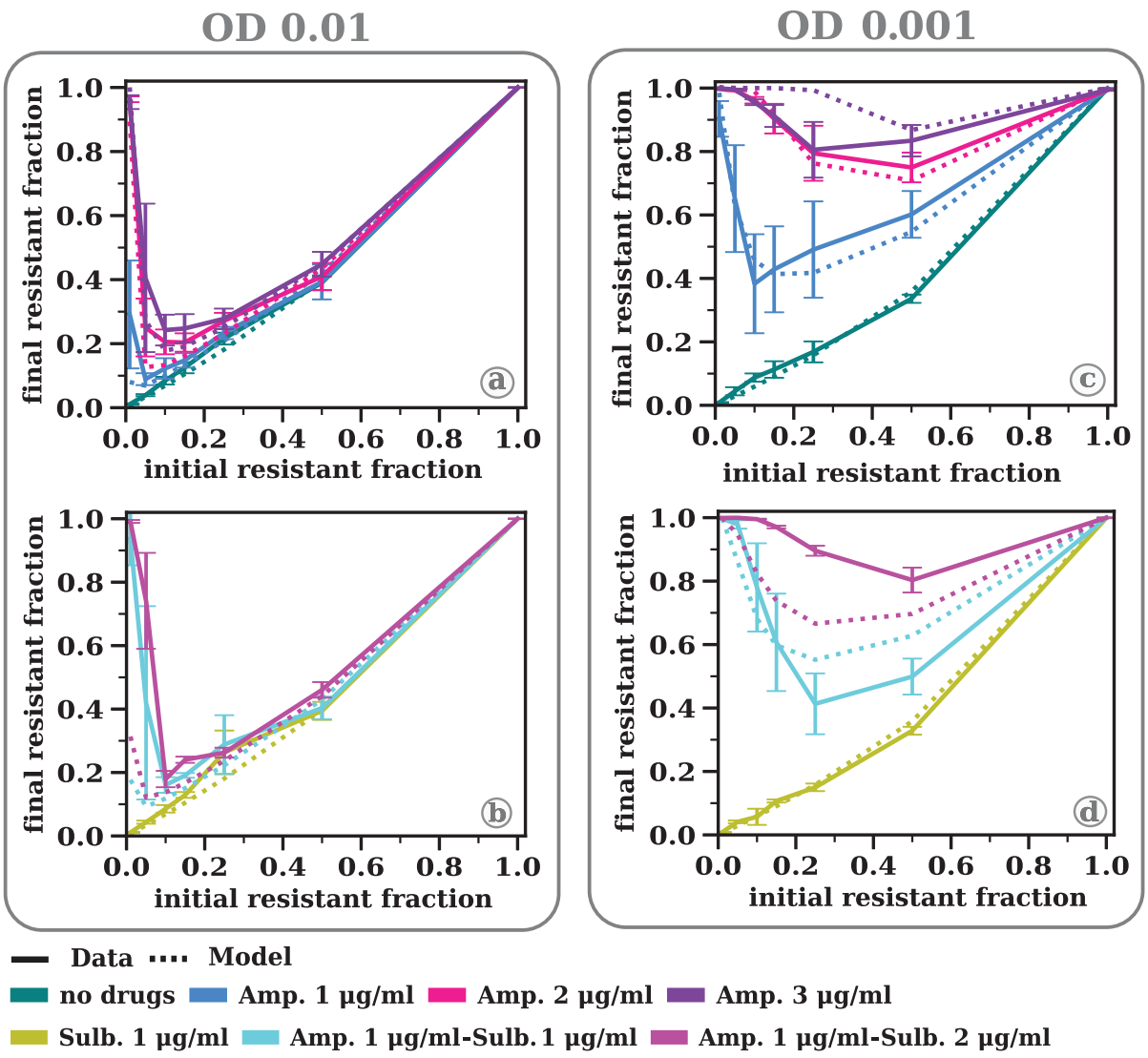


Figure 4.10: Comparison between data and model predictions for initial OD 0.01, panels a and b, and initial OD 0.001, panels c and d. Data is shown in full lines and model predictions in dashed lines. The model is able to accurately predict final resistant fractions for ampicillin only data, panels b and d. With the addition of sulbactam, the model is not able to predict exact final resistant fractions, but it captures the increase in final resistant fractions. The values used to generate the plots are list in Table 4.1.

faecalis, a clinically relevant pathogen that exhibits natural resistance to ampicillin through β-lactamase production. β-lactamase producers degrade antibiotics intracellularly and therefore act as antibiotic sinks, providing cross-protection to ampicillin-sensitive cells. This drug-induced cooperative interaction enables the survival of ampicillin-sensitive bacteria even at super inhibitory antibiotic concentrations. We studied this interaction in mixed populations of ampicillin-resistant and ampicillin-sensitive *E. faecalis* grown in undisturbed liquid cul-

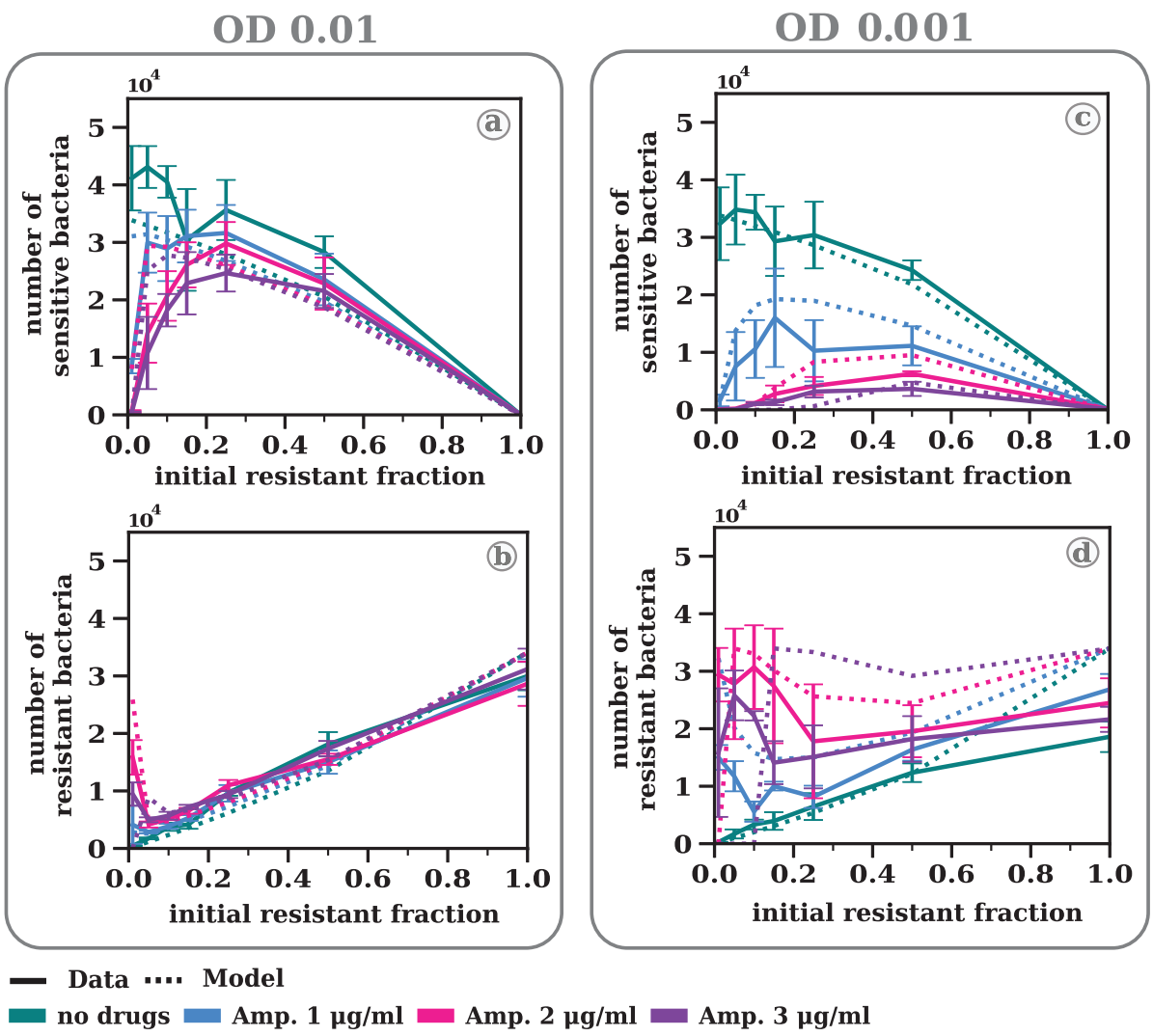


Figure 4.11: Number of sensitive and resistant bacteria in the biofilm as a function of the initial resistant fraction for different values of antibiotic concentrations. The experimental data, in full lines, quantifies the total population in a 80 µm x 80 µm x 60 µm volume averaged over 5 distinct regions and 3 experimental replicas. The fitted data, in dashed lines, reproduce the observed data well, showcasing only an overestimation of resistant bacteria for higher drug concentrations. The total number of sensitive bacteria with no drugs and initial optical density of 0.001, green line in panel c, is used to fit the model parameters $\tilde{b}$ and $\tilde{Y}$, as well as the initial values $\tilde{S}_0 + \tilde{R}_0$, and $\tilde{g}_0$.

ture. During growth, two bacterial communities form, a sessile biofilm and a planktonic population. Using confocal microscopy, we characterized the composition of both populations and quantified the spatial organization within the biofilm.

We find that both planktonic and biofilm populations undergo a population inversion effect under antibiotic treatment, characterized by final resistant fractions higher than their

starting value. Somewhat surprisingly, although planktonic and biofilm bacteria exhibit distinct physiological states, this effect is quantitatively indistinguishable in both populations. The spread of resistance is modulated by the initial cell density, as the initial number of resistant cells affects the drug degradation dynamics, and therefore the amount of cross-protection provided to sensitive cells. We also find that antibiotic exposure does not induce detectable spatial restructuring within the biofilm, that is, the spatial distribution of resistant cells relative to sensitive cells remains unchanged in the presence of the drug. Such experimental observations suggests that the population inversion effect can be explained by employing a well-mixed model with no spatial component. In the model, the cooperative interaction between resistant and sensitive strains is mediated by ampicillin degradation, and bacteria compete for resources as they grow. The model is able to reproduce quantitative and qualitative aspects of the experimental data.

This study leaves open the question of what causes planktonic and biofilm communities to undergo the same population shift. Although determining the cause requires additional experimental data, we can speculate on possible mechanisms. One possibility is that planktonic and biofilm communities are strongly coupled, meaning that planktonic bacteria continuously attach to the biofilm while biofilm bacteria continuously detach and become free-floating. If this coupling is strong enough, the two effectively behave as a single bacterial community.

Following this line of reasoning, two other related mechanistic explanations can be considered. First, the process of attachment of planktonic bacteria to the biofilm may occur on a much faster timescale than growth within the biofilm, such that the biofilm composition is dominated by the composition of the planktonic community. Second, the biofilm itself may be intrinsically loosely structured, in the sense that different strains are not spatially segregated and the population is effectively well-mixed. Previous work has suggested that well-mixed regimes can emerge as a function of nutrient availability and cell growth rate [101].

Another conceptually distinct possibility is that the initial number of resistant bacteria is sufficiently high such that the dynamics of drug degradation occur on a much faster timescale than the dynamics of biofilm formation. This would imply that, by the time the biofilm is being formed, the planktonic population that seeds it has already reached a steady state and antibiotic concentrations have been completely depleted. One last explanation is that the range of the cooperative interaction – the zone of protection provided by resistant bacteria – is sufficiently large that it makes little difference whether a bacteria is part of the planktonic or biofilm population, such that local neighborhood effects become negligible.

CHAPTER 5

Outlook

In this Chapter, we highlight potential directions for future research drawn from the work presented in this Dissertation.

5.1 Topology and thermodynamics bound nonequilibrium response

Nonequilibrium response to arbitrary perturbations in mesoscopic stochastic systems is constrained not only by the thermodynamic driving but also by a measure of fluctuations related to the topology of the state-space. One avenue for future work is extending the bounds to arbitrary combinations of multi-edge perturbations, which can then be applied to the study of nonequilibrium ligand-binding models with more than two binding sites. Another relevant direction is to characterize optimal topologies and formally prove that they saturate the Fluctuation-Response Inequalities derived in this work.

In many biochemical motifs, relevant observables are not limited to state variables [102, 103]. Extending response bounds to observables that depend explicitly on dynamics, such as currents, would be particularly relevant for systems like molecular motors. Another promising direction is the study of time-dependent perturbations [104], which could shed light on cell fate and differentiation, where growing evidence suggests that timing plays an important role [105, 106].

5.2 Maximum nonequilibrium sensitivity does not require higher-order cooperativity

Cooperative interactions play a central role in regulating the process of a ligand binding to a macromolecule. It is not evident how the notion of cooperativity extends beyond the energy-based framework that naturally holds in equilibrium. Both nonequilibrium cooperativity

definitions we introduce are inherently non-reciprocal, meaning its value depends on the order in which binding events occur at the interacting sites. A natural direction for future research is the formulation of definitions of cooperativity that remain reciprocal even arbitrarily far from equilibrium.

Our analysis was restricted to models of receptors with three binding sites, and we conjecture that the findings extend to systems with an arbitrary number of sites. Applying the analysis to models with more binding sites was limited by the challenge of finding samples that reach the maximum predicted sensitivity. Developing alternative algorithms to explore the rate space more efficiently would constitute an important next step. These algorithms would also allow for a more systematic investigation of the central question: what fundamental limits do cooperative interactions impose on nonequilibrium response? Even though higher-order cooperativities do not appear to impose constrains, one could still ask what conditions on lower-order cooperativities are sufficient to generate an increase in the steepness of the binding curves.

5.3 Resistance subpopulations protect biofilm and planktonic populations equally

Collective resistance to antibiotics allows bacteria lacking inherent resistance mechanisms to survive treatment through cooperative interactions with resistant cells. In a system where planktonic and biofilm populations are co-cultured in the presence of antibiotics, we observe that the resistant subpopulations provide a comparable level of protection in both planktonic and biofilm communities. This work leaves open the question of what drives this observed effect. Determining which of the proposed mechanisms underlies this behavior requires additional experimental measurements. One natural next step is to investigate the temporal dynamics of both biofilm and planktonic populations over the course of the experiment. This could be achieved through live microscopy imaging of the biofilm, coupled with tracking of the initial bacterial attachment events that ultimately give rise to biofilm formation. This can reveal how the presence of antibiotics influences biofilm formation and the extent to which the two populations are coupled through bacterial exchange.

Another direction is to characterize the time-dependent dynamics of antibiotic degradation by monitoring how its concentration evolves throughout the experiment. While direct fluorescent tagging of ampicillin is possible, a simpler approach would be to periodically collect liquid media samples, remove remaining bacteria, and plate the samples on agar. Following inoculation with a high-density bacterial culture, the extent of bacterial survival on the plate would provide a proxy for the antibiotic concentration. Tracking antibiotic

concentrations over time could clarify the dynamics of drug degradation and their impact on the cooperative interactions.

Our findings provide an alternative perspective on the assumption that biofilms are inherently more resistant to antibiotics. An important question is whether these results are unique to *E. faecalis* and its biofilm architecture, or if they extend to other bacterial species with similar collective resistance mechanisms.

BIBLIOGRAPHY

[1] R. Kubo, M. Toda, and N. Hashitsume. Statistical Physics II: Nonequilibrium Statistical Mechanics. Springer-Verlag, Berlin, 1985.

[2] P. M. Chaikin and T. C. Lubensky. Principles of condensed matter physics. Cambridge University Press, Cambridge, 2000.

[3] W. Bialek and S. Setayeshgar. Physical limits to biochemical signaling. Proc. Nat. Ac. Sci., 102(29):10040–10045, 2005.

[4] G. C. Govern and P. R. ten Wolde. Optimal resource allocation in cellular sensing systems. Proc. Natl. Acad. Sci. USA, 111(49):17486–17491, 2014.

[5] G. Lan, P. Sartori, S. Neumann, V. Sourjik, and Y. Tu. The energy-speed-accuracy trade-off in sensory adaptation. Nat. Phys., 8:422–428, 2012.

[6] P. Sartori and Y. Tu. Free energy cost of reducing noise while maintaining a high sensitivity. Phys. Rev. Lett., 115:118102, 2015.

[7] Michael S. Gilmore, Don B. Clewell, Yasuyoshi Ike, and Nathan Shankar, editors. Enterococci: From Commensals to Leading Causes of Drug Resistant Infection. Massachusetts Eye and Ear Infirmary, Boston, 2014.

[8] Eugene A. Yurtsev, Hui Xiao Chao, Manoshi S. Datta, Tatiana Artemova, and Jeff Gore. Bacterial cheating drives the population dynamics of cooperative antibiotic resistance plasmids. Molecular Systems Biology, 9(1):MSB201339, August 2013.

[9] Robin A. Sorg, Leo Lin, G. Sander Van Doorn, Moritz Sorg, Joshua Olson, Victor Nizet, and Jan-Willem Veening. Collective Resistance in Microbial Communities by Intracellular Antibiotic Deactivation. PLOS Biology, 14(12):e2000631, December 2016.

[10] Ayush Pathak, Daniel C Angst, Ricardo León-Sampedro, and Alex R Hall. Antibiotic-degrading resistance changes bacterial community structure via species-specific responses. The ISME Journal, 17(9):1495–1503, September 2023.

[11] Rotem Gross, Muhittin Mungan, Suman G. Das, Melih Yüksel, Berenike Maier, Tobias Bollenbach, Joachim Krug, and J. Arjan G. M. de Visser. Collective -lactam resistance in Escherichia coli due to -lactamase release upon cell death, October 2024. Pages: 2024.10.14.618215 Section: New Results.

[12] Rodney M. Donlan. Biofilms: Microbial Life on Surfaces - Volume 8, Number 9—September 2002 - Emerging Infectious Diseases journal - CDC. September 2002.

[13] Gabriela Fernandes Martins and Jordan M. Horowitz. Topologically constrained fluctuations and thermodynamics regulate nonequilibrium response. Physical Review E, 108(4):044113, October 2023. Publisher: American Physical Society.

[14] G. S. Agarwal. Fluctuation-dissipation theorems for systems in non-thermal equilibrium and applications. Z. Phys. A, 252:25–38, 1972.

[15] U. Seifert and T. Speck. Fluctuation-dissipation theorem in nonequilibrium steady states. Europhys. Lett., 89:10007, 2010.

[16] Marco Baiesi, Christian Maes, and Bram Wynants. Fluctuations and Response of Nonequilibrium States. Physical Review Letters, 103(1):010602, July 2009.

[17] Takahiro Harada and S. I. Sasa. Equality connecting energy dissipation with a violation of the fluctuation-response relation. Phys. Rev. Lett., 95(13):130602, 2005.

[18] Christopher Jarzynski. Equalities and Inequalities: Irreversibility and the Second Law of Thermodynamics at the Nanoscale. Annual Review of Condensed Matter Physics, 2(1):329–351, 2011.

[19] Andre C Barato and Udo Seifert. Thermodynamic uncertainty relation for biomolecular processes. Phys. Rev. Lett., 114(15):158101, 2015.

[20] J. M. Horowitz and T. R. Gingrich. Proof of the finite-time thermodynamic uncertainty relation for steady-state currents. Phys. Rev. E, 96:020103, 2017.

[21] J. A. Owen, T. R. Gingrich, and J. M. Horowitz. Universal thermodynamic bounds on nonequilibrium response with biochemical applications. Phys. Rev. X, 10:011066, 2020.

[22] Jeremy A. Owen and Jordan M. Horowitz. Size limits the sensitivity of kinetic schemes. Nat. Commun., 14, 2023.

[23] Q. Gao, H.-M. Chun, and J. M. Horowitz. Thermodynamic constraints on the nonequilibrium response of one-dimensional diffusions. Phys. Rev. E, 105:L012102, 2022.

[24] Hyun-Myung Chun and Jordan M. Horowitz. Trade-offs between number fluctuations and response in nonequilibrium chemical reaction networks. J. Chem. Phys, 158(17):174115, 05 2023.

[25] Jürgen Schnakenberg. Network theory of microscopic and macroscopic behavior of master equation systems. Rev. Mod. Phys., 48(4):571, 1976.

[26] T. L. Hill. Free Energy Transduction in Biology. Academic Press, New York, 1977.

[27] C. Maes and K. Netočný. Heat bounds and the blowtorch theorem. J. Stat. Phys., 14:1193–1202, 2012.

[28] Shiling Liang, Paolo De Los Rios, and Daniel Maria Busiello. Thermodynamic Bounds on Symmetry Breaking in Linear and Catalytic Biochemical Systems. Physical Review Letters, 132(22):228402, May 2024. Publisher: American Physical Society.

[29] K.-M. Nam, R. Martinez-Corral, and J. Gunawardena. The linear framework: using graph theory to reveal the algebra and thermodynamics of biomolecular systems. Interface Focus, 12(20220013), 2022.

[30] U. Cetiner and J. Gunawardena. Reformulating nonequilibrium steady states and generalized hopfield discrimination. Phys. Rev. E, 106:064128, 2022.

[31] Timur Aslyamov. Nonequilibrium Response for Markov Jump Processes: Exact Results and Tight Bounds. Physical Review Letters, 132(3), 2024.

[32] Timur Aslyamov and Massimiliano Esposito. General Theory of Static Response for Markov Jump Processes. Physical Review Letters, 133(10):107103, September 2024. Publisher: American Physical Society.

[33] Krzysztof Ptaszynski, Timur Aslyamov, and Massimiliano Esposito. Nonequilibrium fluctuation-response relations for state-current correlations, December 2025. arXiv:2506.08877 [cond-mat].

[34] Timur Aslyamov, Krzysztof Ptaszyński, and Massimiliano Esposito. Nonequilibrium Fluctuation-Response Relations: From Identities to Bounds. Physical Review Letters, 134(15):157101, April 2025. Publisher: American Physical Society.

[35] Krzysztof Ptaszynski, Timur Aslyamov, and Massimiliano Esposito. Nonequilibrium fluctuation-response relations for state observables, January 2026. arXiv:2412.10233 [cond-mat].

[36] Jeremy Gunawardena. A linear framework for time-scale separation in nonlinear biochemical systems. PloS one, 7(5):e36321, 2012.

[37] J. A. Owen and J. M. Horowitz. Size limits sensitivity in all kinetic schemes. arXiv:2112.07777.

[38] L. Peliti and S. Pigolotti. Stochastic thermodynaics: An introduction. Princeton University Press, New Jersey, 2021.

[39] N. G. Van Kampen. Stochastic Processes in Physics and Chemistry. Elsevier Ltd., New York, 3rd edition, 2007.

[40] U. Seifert. Stochastic thermodynamics, fluctuation theorems, and molecular machines. Rep. Prog. Phys., 75:126001, 2012.

[41] C. Van den Broeck and M. Esposito. Ensemble and trajectory thermodynamics: A brief introduction. Physica A, 418:6–16, 2015.

[42] D. Andrieux and P. Gaspard. Fluctuation theorem for transport in mesoscopic systems. J. Stat. Mech.: Theor. Exp., page P01011, Jan 2006.

[43] S. Chaiken. A combinatorial proof for the all minors matrix tree theorem. SIAM J. Alg. Disc. Meth., 3(3):319–329, 1982.

[44] P. Chebotarev and R. Agaev. Forest matrices around the laplacian matrix. Linear Algebra Appl., 356:253–274, 2002.

[45] M. Baiesi and C. Maes. An update on the nonequilibrium linear response. New J. Phys., 15:013004, 2013.

[46] Thomas M. Cover and Joy A. Thomas. Elements of Information Theory. Wiley-Interscience, New York, second edition, 2006.

[47] David G. Luenberger and Yinyu Ye. Linear and Nonlinear Programming. Springer International Publishing, 2016.

[48] T. L. Hill. Cooperativity Theory in Biochemistry: Steady-state and Equilibrium Systems. Spring Series in Molecular Biology. Springer-Verlag, New York, 1985.

[49] R. Phillips. The Molecular Switch: Signalling and Allostery. Princeton University Press, New Jersey, 2020.

[50] Sara Mahdavi, Gabriel L. Salmon, Patill Daghlian, Hernan G. Garcia, and Rob Phillips. Flexibility and sensitivity in gene regulation out of equilibrium. 2023.

[51] M. Razo-Mejia, S. L. Barnes, N. M. Belliveau, G. Chure, T. Einav, M. Lewis, and R. Phillips. Tunig transcriptional regulation through signaling: A predictive theory of allosteric induction. Cell Syst., 6(4):456–469.e10, 2019.

[52] A. Reimer, S. Alamos, C. Westrum, M. A. Turner, P. Talledo, J. Zhao, and H. G. Garcia. Minimal synthetic enhancers reveal control of the probability of transcriptional engagement and its timing by a morphogen gradient. Cell Systems, 14, 2023.

[53] Y. J. Kim, K. Rhee, J. Liu, S. Jeammet, M. A. Turner, S. J. Small, and H. G. Garcia. Predictive modeling reveals higher-order cooperativity drives transcriptional repression in a synthetic developmental enhancer. eLife, 11:e73395, 2022.

[54] J. Estrada, F. Wong, A. DePace, and J. Gunawardena. Information integration and energy expenditure in gene regulation. Cell, 166:234–244, 2016.

[55] Chr. Bohr, K. Hasselbalch, and August Krogh. Ueber einen in biologischer Beziehung wichtigen Einfluss, den die Kohlensäurespannung des Blutes auf dessen Sauerstoff-bindung übt. Skandinavisches Archiv Für Physiologie, 16(2):402–412, 1904. _eprint: https://onlinelibrary.wiley.com/doi/pdf/10.1111/j.1748-1716.1904.tb01382.x.

[56] Archibald Hill. The possible effects of the aggregation of the molecules of haemoglobin on its oxygen dissociation curve. PROCEEDINGS OF THE PHYSIOLOGICAL SOCIETY, 40:i–vii, 1910.

[57] Phillips, Rob. The Molecular Switch. 2019.

[58] John W Biddle, Rosa Martinez-Corral, Felix Wong, and Jeremy Gunawardena. Allosteric conformational ensembles have unlimited capacity for integrating information. eLife, 10:e65498, June 2021. Publisher: eLife Sciences Publications, Ltd.

[59] Linus Pauling. The Oxygen Equilibrium of Hemoglobin and Its Structural Interpretation. Proceedings of the National Academy of Sciences, 21(4):186–191, April 1935. Publisher: Proceedings of the National Academy of Sciences.

[60] Marlis Denk-Lobnig and Kevin B Wood. Antibiotic resistance in bacterial communities. Current Opinion in Microbiology, 74:102306, August 2023.

[61] Jacob Moran and Kevin B. Wood. From Fluctuations and Disorder to Scaling and Control: The Emergence of Resistance in Microbial Communities. Annual Review of Condensed Matter Physics, 16(Volume 16, 2025):297–318, March 2025. Publisher: Annual Reviews.

[62] Jessica M. A. Blair, Mark A. Webber, Alison J. Baylay, David O. Ogbolu, and Laura J. V. Piddock. Molecular mechanisms of antibiotic resistance. Nature Reviews Microbiology, 13(1):42–51, January 2015. Publisher: Nature Publishing Group.

[63] Nicole M Vega and Jeff Gore. Collective antibiotic resistance: mechanisms and implications. Current Opinion in Microbiology, 21:28–34, October 2014.

[64] Sivan Pearl Mizrahi, Akshit Goyal, and Jeff Gore. Community interactions drive the evolution of antibiotic tolerance in bacteria. Proceedings of the National Academy of Sciences, 120(3):e2209043119, January 2023. Publisher: Proceedings of the National Academy of Sciences.

[65] Gerard D. Wright. Bacterial resistance to antibiotics: Enzymatic degradation and modification. Advanced Drug Delivery Reviews, 57(10):1451–1470, July 2005.

[66] Mary Ellen Davey and George A. O'toole. Microbial Biofilms: from Ecology to Molecular Genetics. Microbiology and Molecular Biology Reviews, 64(4):847–867, December 2000. Publisher: American Society for Microbiology.

[67] Anahit Penesyan, Ian T. Paulsen, Staffan Kjelleberg, and Michael R. Gillings. Three faces of biofilms: a microbial lifestyle, a nascent multicellular organism, and an incubator for diversity. npj Biofilms and Microbiomes, 7(1):80, November 2021. Publisher: Nature Publishing Group.

[68] David Davies. Understanding biofilm resistance to antibacterial agents. Nature Reviews Drug Discovery, 2(2):114–122, February 2003. Publisher: Nature Publishing Group.

[69] Ho Yu Liu, Emma L. Prentice, and Mark A. Webber. Mechanisms of antimicrobial resistance in biofilms. npj Antimicrobials and Resistance, 2(1):27, October 2024. Publisher: Nature Publishing Group.

[70] Philip S Stewart and J William Costerton. Antibiotic resistance of bacteria in biofilms. The Lancet, 358(9276):135–138, July 2001.

[71] Hans-Curt Flemming, Jost Wingender, Ulrich Szewzyk, Peter Steinberg, Scott A. Rice, and Staffan Kjelleberg. Biofilms: an emergent form of bacterial life. Nature Reviews Microbiology, 14(9):563–575, September 2016. Publisher: Nature Publishing Group.

[72] Clayton W. Hall and Thien-Fah Mah. Molecular mechanisms of biofilm-based antibiotic resistance and tolerance in pathogenic bacteria. FEMS Microbiology Reviews, 41(3):276–301, May 2017.

[73] Philip Ruelens, Eline de Ridder, J. Arjan G. M. de Visser, and Meike T. Wortel. Density-dependent feedback limits the spread of beta-lactamase mutants: experimental observations and population dynamic model. mBio, 16(8):e01500–25, July 2025. Publisher: American Society for Microbiology.

[74] B E Murray. Beta-lactamase-producing enterococci. Antimicrobial Agents and Chemotherapy, 36(11):2355–2359, November 1992. Publisher: American Society for Microbiology.

[75] Marlis K. Denk-Lobnig and Kevin B. Wood. Spatial population dynamics of bacterial colonies with social antibiotic resistance. Proceedings of the National Academy of Sciences, 122(7):e2417065122, February 2025. Publisher: Proceedings of the National Academy of Sciences.

[76] Anupama Sharma and Kevin B. Wood. Spatial segregation and cooperation in radially expanding microbial colonies under antibiotic stress. The ISME Journal, 15(10):3019–3033, October 2021. Publisher: Nature Publishing Group.

[77] L B Rice, G M Eliopoulos, C Wennersten, D Goldmann, G A Jacoby, and R C Moellering. Chromosomally mediated beta-lactamase production and gentamicin resistance in Enterococcus faecalis. Antimicrobial Agents and Chemotherapy, 35(2):272–276, February 1991. Publisher: American Society for Microbiology.

[78] Kelsey M. Hallinen, Keanu A. Guardiola-Flores, and Kevin B. Wood. Fluorescent reporter plasmids for single-cell and bulk-level composition assays in E. faecalis. PLOS ONE, 15(5):e0232539, 2020. Publisher: Public Library of Science.

[79] Kelsey M Hallinen, Jason Karslake, and Kevin B Wood. Delayed antibiotic exposure induces population collapse in enterococcal communities with drug-resistant subpopulations. eLife, 9:e52813, March 2020. Publisher: eLife Sciences Publications, Ltd.

[80] Johannes Schindelin, Ignacio Arganda-Carreras, Erwin Frise, Verena Kaynig, Mark Longair, Tobias Pietzsch, Stephan Preibisch, Curtis Rueden, Stephan Saalfeld, Benjamin Schmid, Jean-Yves Tinevez, Daniel James White, Volker Hartenstein, Kevin Eliceiri, Pavel Tomancak, and Albert Cardona. Fiji: an open-source platform for biological-image analysis. Nature Methods, 9(7):676–682, July 2012. Publisher: Nature Publishing Group.

[81] Stuart Berg, Dominik Kutra, Thorben Kroeger, Christoph N. Straehle, Bernhard X. Kausler, Carsten Haubold, Martin Schiegg, Janez Ales, Thorsten Beier, Markus Rudy, Kemal Eren, Jaime I. Cervantes, Buote Xu, Fynn Beuttenmueller, Adrian Wolny, Chong Zhang, Ullrich Koethe, Fred A. Hamprecht, and Anna Kreshuk. ilastik: interactive machine learning for (bio)image analysis. Nature Methods, 16(12):1226–1232, December 2019. Publisher: Nature Publishing Group.

[82] Hervé Nicoloff and Dan I. Andersson. Indirect resistance to several classes of antibiotics in cocultures with resistant bacteria expressing antibiotic-modifying or -degrading enzymes. Journal of Antimicrobial Chemotherapy, 71(1):100–110, January 2016.

[83] Isabel Frost, William P J Smith, Sara Mitri, Alvaro San Millan, Yohan Davit, James M Osborne, Joe M Pitt-Francis, R Craig MacLean, and Kevin R Foster. Cooperation, competition and antibiotic resistance in bacterial colonies. The ISME Journal, 12(6):1582–1593, June 2018.

[84] Elli Amanatidou, Andrew C. Matthews, Ute Kuhlicke, Thomas R. Neu, James P. McEvoy, and Ben Raymond. Biofilms facilitate cheating and social exploitation of -lactam resistance in Escherichia coli. npj Biofilms and Microbiomes, 5(1):36, November 2019.

[85] J A Francisco, C F Earhart, and G Georgiou. Transport and anchoring of beta-lactamase to the external surface of Escherichia coli. Proceedings of the National Academy of Sciences, 89(7):2713–2717, April 1992. Publisher: Proceedings of the National Academy of Sciences.

[86] Sarah M. Drawz and Robert A. Bonomo. Three Decades of -Lactamase Inhibitors. Clinical Microbiology Reviews, 23(1):160–201, January 2010. Publisher: American Society for Microbiology.

[87] K Bush. Beta-lactamase inhibitors from laboratory to clinic. Clinical Microbiology Reviews, 1(1):109–123, January 1988. Publisher: American Society for Microbiology.

[88] Davide Carcione, Claudia Siracusa, Adela Sulejmani, Valerio Leoni, and Jari Intra. Old and New Beta-Lactamase Inhibitors: Molecular Structure, Mechanism of Action, and Clinical Use. Antibiotics, 10(8):995, August 2021. Publisher: Multidisciplinary Digital Publishing Institute.

[89] Arthur R. English, James A. Retsema, Arthur E. Girard, John E. Lynch, and Wayne E. Barth. CP-45,899, a Beta-Lactamase Inhibitor That Extends the Antibacterial Spectrum of Beta-Lactams: Initial Bacteriological Characterization. Antimicrobial Agents and Chemotherapy, 14(3):414–419, September 1978. Publisher: American Society for Microbiology.

[90] Jennifer L. Dale, Jennifer L. Nilson, Aaron M. T. Barnes, and Gary M. Dunny. Restructuring of Enterococcus faecalis biofilm architecture in response to antibiotic-induced stress. npj Biofilms and Microbiomes, 3(1):15, June 2017. Publisher: Nature Publishing Group.

[91] Elizabeth J. Stewart, Ashley E. Satorius, John G. Younger, and Michael J. Solomon. Role of Environmental and Antibiotic Stress on Staphylococcus epidermidis Biofilm Microstructure. Langmuir, 29(23):7017–7024, June 2013. Publisher: American Chemical Society.

[92] Ricardo Martínez-García, Carey D. Nadell, Raimo Hartmann, Knut Drescher, and Juan A. Bonachela. Cell adhesion and fluid flow jointly initiate genotype spatial distribution in biofilms. PLOS Computational Biology, 14(4):e1006094, 2018. Publisher: Public Library of Science.

[93] Claudia Schillinger, Annett Petrich, Renate Lux, Birgit Riep, Judith Kikhney, Anton Friedmann, Lawrence E. Wolinsky, Ulf B. Göbel, Holger Daims, and Annette Moter. Co-Localized or Randomly Distributed? Pair Cross Correlation of In Vivo Grown Subgingival Biofilm Bacteria Quantified by Digital Image Analysis. PLOS ONE, 7(5):e37583, 2012. Publisher: Public Library of Science.

[94] Nicholas A. Rossi, Imane El Meouche, and Mary J. Dunlop. Forecasting cell fate during antibiotic exposure using stochastic gene expression. Communications Biology, 2(1):259, July 2019. Publisher: Nature Publishing Group.

[95] Daniel Schultz, Adam C. Palmer, and Roy Kishony. Regulatory Dynamics Determine Cell Fate following Abrupt Antibiotic Exposure. Cell Systems, 5(5):509–517.e3, November 2017. Publisher: Elsevier.

[96] Jacques Monod. The growth of bacterial cultures. Annual Review of Microbiology, 3(Volume 3, 1949):371–394, October 1949. Publisher: Annual Reviews.

[97] Arthur L. Koch. The Monod Model and Its Alternatives. In Arthur L. Koch, Joseph A. Robinson, and George A. Milliken, editors, Mathematical Modeling in Microbial Ecology, pages 62–93. Springer US, Boston, MA, 1998.

[98] Xinxian Shao, Andrew Mugler, Justin Kim, Ha Jun Jeong, Bruce R. Levin, and Ilya Nemenman. Growth of bacteria in 3-d colonies. PLOS Computational Biology, 13(7):e1005679, July 2017. Publisher: Public Library of Science.

[99] Roland R. Regoes, Camilla Wiuff, Renata M. Zappala, Kim N. Garner, Fernando Baquero, and Bruce R. Levin. Pharmacodynamic Functions: a Multiparameter Approach to the Design of Antibiotic Treatment Regimens. Antimicrobial Agents and Chemotherapy, 48(10):3670–3676, October 2004. Publisher: American Society for Microbiology.

[100] Adam B. Shapiro. Kinetics of Sulbactam Hydrolysis by -Lactamases, and Kinetics of -Lactamase Inhibition by Sulbactam. Antimicrobial Agents and Chemotherapy, 61(12):10.1128/aac.01612–17, November 2017. Publisher: American Society for Microbiology.

[101] Carey D. Nadell, Kevin R. Foster, and João B. Xavier. Emergence of Spatial Structure in Cell Groups and the Evolution of Cooperation. PLOS Computational Biology, 6(3):e1000716, March 2010.

[102] John J. Tyson and Béla Novák. Functional Motifs in Biochemical Reaction Networks. Annual review of physical chemistry, 61:219–240, 2010.

[103] R. Dean Astumian. Thermodynamics and Kinetics of Molecular Motors. Biophysical Journal, 98(11):2401–2409, June 2010.

[104] Arvind Murugan, Kabir Husain, Michael J Rust, Chelsea Hepler, Joseph Bass, Julian M J Pietsch, Peter S Swain, Siddhartha G Jena, Jared E Toettcher, Arup K Chakraborty, Kayla G Sprenger, T Mora, A M Walczak, O Rivoire, Shenshen Wang, Kevin B Wood, Antun Skanata, Edo Kussell, Rama Ranganathan, Hong-Yan Shih, and Nigel Goldenfeld. Roadmap on biology in time varying environments. Physical biology, 18(4):10.1088/1478–3975/abde8d, May 2021.

[105] G. Fernandes, H. Tran, M. Andrieu, Y. Diaw, C. Perez Romero, C. Fradin, M. Coppey, A. M. Walczak, and N. Dostatni. Synthetic reconstruction of the hunchback promoter specifies the role of Bicoid, Zelda and Hunchback in the dynamics of its transcription. eLife, 11:e74509, 2021.

[106] Mochi Liu, Anuj K Sharma, Joshua W Shaevitz, and Andrew M Leifer. Temporal processing and context dependency in Caenorhabditis elegans response to mechanosensation. eLife, 7:e36419.